Diploma Thesis

Deeply Virtual Compton Scattering on Neon

Sebastian Haan

UNIVERSITÄT LEIPZIG

August 16, 2005

Supervisor at the University of Leipzig: Prof. Dr. T. Butz
Supervisor at DESY: Dr. W.-D. Nowak

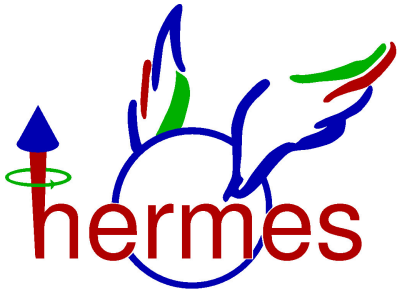

The HERMES Experiment

Deutsches Elektronen-Synchroton DESY

Contents

Abstract

The measurement of Deeply Virtual Compton Scattering (DVCS) provides access to the spin structure of nucleons. Its description within the theoretical framework of generalized parton distributions offers a possibility to determine the total angular momentum carried by the quarks in the nucleon.
In this thesis a cross section asymmetry with respect to the beam-helicity has been measured for hard exclusive electroproduction of photons from a neon target. The resulting asymmetry appears in the distribution of the produced photon in the azimuthal angle ϕ around the virtual-photon direction. Attributed to the interference between the Bethe-Heitler process and the DVCS process, the asymmetry gives access to the latter at the amplitude level. The DVCS reaction on nuclei proceeds through two different processes the coherent process that involves the nucleus as a whole and the incoherent process as the reaction on a single nucleon. The beam-helicity asymmetry and its dependences are studied for the coherent and incoherent sample, separately. The data presented has been accumulated by the HERMES experiment at DESY, scattering the HERA 27.6 GeV polarized positron beam off an unpolarized neon target.

Kurzfassung

Schnelle geladene Teilchen haben sich schon seit längerer Zeit als nützliches Instrument zur Untersuchung der Struktur von Nukleonen erwiesen. Bei dem Prozess der tiefvirtuellen Comptonstreuung (DVCS) werden durch die Streuung von hochenergetischen Elektronen oder deren Antiteilchen (Positronen) an einem Parton (Quark oder Gluon) im Inneren des Nukleons Photonen erzeugt.
Seit einigen Jahren existiert der Formalismus der sogenannten "'generalisierten Partonverteilungen"' (GPDs) zur Beschreibung derartiger Prozesse. Diese GPDs enthalten zusätzlich zur Beschreibung der Partonstruktur des Nukleons, ausgedrückt durch die einfachen Partonverteilungen (PDFs), noch zusätzliche Information über Korrelationen der Quarks und Gluonen untereinander. Die Messung von GPDs ermöglicht im Prinzip die Bestimmung des Gesamtdrehimpulsanteils der Quarks und Gluonen innerhalb des Nukleons.
In der vorliegenden Arbeit wurde die Asymmetrie in Bezug auf die Polarisationsrichtung des Positronstrahles für die exklusive Erzeugung von Photonen an Neonkernen gemessen. Die Asymmetrie tritt in der Verteilung der Photonen bezüglich des azimuthalen Winkels ϕ zwischen Positronenstreuebene und Photonenerzeugungsebene auf. Dabei kommt es zu einer Überlagerung mit dem Bethe-Heitler (BH) Prozess, der auf der Abstrahlung von Photonen durch Bremsstrahlung beruht. Aufgrund der Interferenz beider Prozesse, DVCS und BH, ist es möglich, den Imaginärteil der Interferenz-Amplitude zu bestimmen, der wiederum in Beziehung zu den generalisierten Partonenverteilungen steht. Im Fall von DVCS an Kernen ist zwischen zwei verschiedenen Reaktionen zu unterscheiden: Zum einen gibt es den kohärenten Prozess, bei dem der Kern in seiner Gesamtheit

reagiert, und zum anderen den inkohärenten Prozess, der durch die Reaktion an einem einzelnen Proton oder Neutron gekennzeichnet ist. In dieser Arbeit wurde für beide, den kohärenten und inkohärenten Prozess, eine Strahl-Polarisations Asymmetrie gemessen, sowie deren kinematische Abhängigkeiten untersucht. Die zu Grunde liegenden Daten stammen aus dem Jahr 2000 vom HERMES Experiment am DESY, wobei der 27.6 GeV polarisierte Positronen Strahl von HERA an unpolarisiertem Neongas gestreut wurde.

1 Introduction

Most of our knowledge about the structure of matter was gained by scattering experiments. After Rutherford discovered the existence of a nucleus in an atom more than 90 years ago, it was shown 50 years ago that they are composed of protons and neutrons [Hof57]. Over the past few decades, the research on the structure of matter has made enormous strides. In the late sixties, deep inelastic lepton nucleon scattering at SLAC (Stanford Linear Accelerator Center) [A$^+$76, B$^+$83] showed that protons are composed of point-like objects called partons. In the quark-parton-model partons are identified with quarks carrying spin and a charge of multiples of one third of the elementary charge e. Further experiments showed that the nucleon consists not only of quarks but also of gluons, which are the mediating particles of the strong interactions. At HERA (Hadron Elektron Ring Anlage) of the DESY laboratory in Hamburg, this research is continued to determine the parton structure of nucleons.

In order to investigate in particular the spin structure of the nucleon, the HERMES experiment was built. The nucleon spin can be decomposed conceptually into the angular momentum contributions of its constituents according to the equation

$$\left\langle s_z^N \right\rangle = \frac{1}{2} = \frac{1}{2}\Delta\Sigma + L_q + J_g$$

where the three terms give the contributions to the nucleon spin from the quark spins, the quark orbital angular momentum, and the total angular momentum of the gluons, respectively. Since the results from the European Muon Collaboration (EMC) [Muon88, Muon89] led to the conclusion that $\Delta\Sigma \approx 0.1 - 0.2$, one of the most interesting questions is to understand how the remaining contribution is distributed between the orbital angular momentum of the quarks L_q and the total angular momentum of the gluons J_g. The only known way nowadays to access the size of those contributions is to determine the total angular momentum of the quarks in the framework of generalized parton distributions (GPDs). This theoretical formalism describes the quark-gluon structure of a nucleon and takes into account dynamical correlations between partons of different momenta in the nucleon. The ordinary parton distribution functions (PDFs) and form factors turn out to be the limiting cases and moments of GPDs, respectively. The theoretically cleanest process sensitive to GPDs and accessible nowadays is Deeply Virtual Compton Scattering (DVCS).

DVCS denotes exclusive production of high energy photons, where in contrast to Bremsstrahlung the photon is not emitted by the lepton but by one of the quarks inside the nucleon. In

the present analysis DVCS is studied through positron scattering on a nuclear target. This reaction receives contributions from both the DVCS process, whose origin lies in the strong interaction, and the electromagnetic Bethe-Heitler (BH) process, well known as Bremsstrahlung. Note that the BH cross section can be precisely calculated in quantum electrodynamics (QED) using elastic form factors. At HERMES kinematics, the DVCS process can not be clearly separated from the interfering BH process because the final states are indistinguishable and hence their scattering amplitudes add coherently:

$$|\tau|^2 = |\tau_{BH}|^2 + |\tau_{DVCS}|^2 + \underbrace{\tau^*_{BH}\tau_{DVCS} + \tau^*_{DVCS}\tau_{BH}}_{Interference\ term\ I}.$$

The BH-DVCS interference term I offers the possibility to directly access the DVCS amplitudes. Thereby the imaginary part of the interference term can be isolated by measuring the angular dependence of the produced photon if polarized lepton beams are available. In order to access the real part in addition, lepton beams of both charges are needed. A determination of the angular dependences in beam-spin and beam-charge asymmetry provides the possibility to access DVCS amplitudes and through them certain combinations of GPDs.

The measurement of DVCS on the proton has shown the possibility to provide a sensitive test of current models of GPDs [Ell, Kra]. Such studies open also access for questions to the properties of the quark and gluon matter inside nuclei. Consequently, nuclear DVCS allows the study of the modifications of particle correlations encoded in GPDs within the nuclear environment. Hence it may shed new light on the dynamical interplay of highly complex bound hadronic systems [Pol03].

The aim of this thesis was to study and to extract beam-spin asymmetries for an unpolarized neon target. The outline is as follows. The theoretical description of GPDs and their relation to the DVCS process is explained in the next chapter. The third chapter will explain the relevant aspects of the HERMES experiment for this study. In chapter 4 the selection criteria for the data and the extraction of the beam-spin asymmetry is described. The systematic studies are given in chapter 5, and the results are shown in chapter 6. In the end an interpretation of the results by a comparison to hydrogen results is performed in chapter 7. The last chapter of this thesis will give a short summary and outlook.

2 Generalized Parton Distributions and Deeply Virtual Compton Scattering

In the theory of Quantum Chromodynamics (QCD), one of the main questions is the understanding of the substructure of hadrons. Therefore, most high energy experiments study inclusive reactions, such as deep inelastic scattering (DIS): $e+p \longrightarrow e+X$. These processes are described in QCD by parton distribution functions (PDFs), which encode the one-dimensional distribution of longitudinal momentum and polarization, carried by quarks, antiquarks and gluons.

By definition PDFs do not contain information on the three-dimensional distribution of the hadronic substructure. In order to extract the additional information, particle correlation functions have to be measured that depend on additional variables, characterizing e.g. the momentum difference of the "in" and "out" state. Therefore, processes are required in which the nucleon stays intact, otherwise the dynamical relationship between the different partons could not be accessed anymore. In such processes, either all produced particles have to be detected and clearly separated from the intact final state nucleon, or the missing mass has to be calculated in order to characterize the difference between the initial energy and the sum of the energy of all reconstructed particles in the detector. In particular Deeply Virtual Compton Scattering (DVCS) $e + p \Rightarrow e + p + \gamma$ provides such a process, which constitutes a hard exclusive reaction. Note that hard means here a large momentum transfer from probe to target. These exclusive hard reactions, e.g. DVCS, are described by particle correlation functions, called Generalized Parton Distributions (GPDs).

GPDs have been extensively studied theoretically in recent years [M$^+$94, Ji97a, Rad97, Die03]. They came into the focus of interest, after Ji has found that GPDs offer the possibility to determine the total angular momentum carried by quarks and gluons [Ji97b]. Nowadays, GPDs start to play a central role in the studies of nuclear structure. Figure 2.1 presents a schematic overview about the exclusive processes that are related to GPDs. In comparison to other exclusive processes, DVCS is the theoretically cleanest process accessible today that allows access to GPDs in the nucleon. This can be explained by the fact that the real photon in the final state is a pointlike particle and not a bound state like a meson, or an even more complicated state. Note that the non-pointlike part of the real photon wave function is suppressed in DVCS [Rad97, JF99]. Experimentally very difficult to access is the process of timelike Compton scattering describing the production of a virtual photon that converts into a lepton-antilepton pair, as it is suppressed by

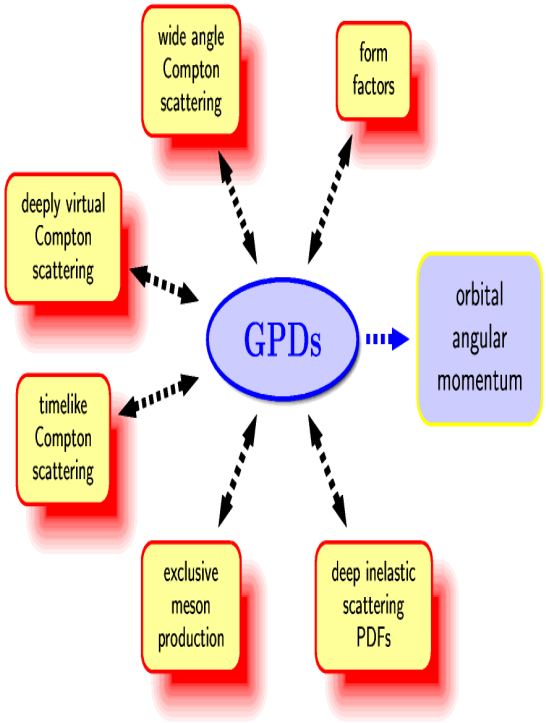

Figure 2.1: Reactions and nucleon properties related to GPDs.

α_{em}^2 compared to the DVCS process. In the Wide-Angle Compton Scattering process, the initial and final photons are real and the involved momentum transfer is large.

2.1 Properties of Generalized Parton Distributions

GPDs are universal non-perturbative objects, entering the description of hard exclusive electroproduction processes [GPRV04]. First implicitly introduced in [M$^+$94, Ji97a, Rad97], they are generally defined for each quark flavor (u,d,s) and gluon (g) as a parameterization of matrix elements of lightcone operators [Rad96]. The matrix elements can be described as elements of the transition matrix between the initial and final hadron state.

The GPDs can be characterized by the following features:

- They depend on two longitudinal momentum fraction variables (x, ξ) and on the Mandelstam variable t, defining the momentum transfer to the nucleon, which also contains transverse components. The involvement of GPDs in the DVCS process and the relevant kinematic variables are shown in figure 2.2 which illustrates the

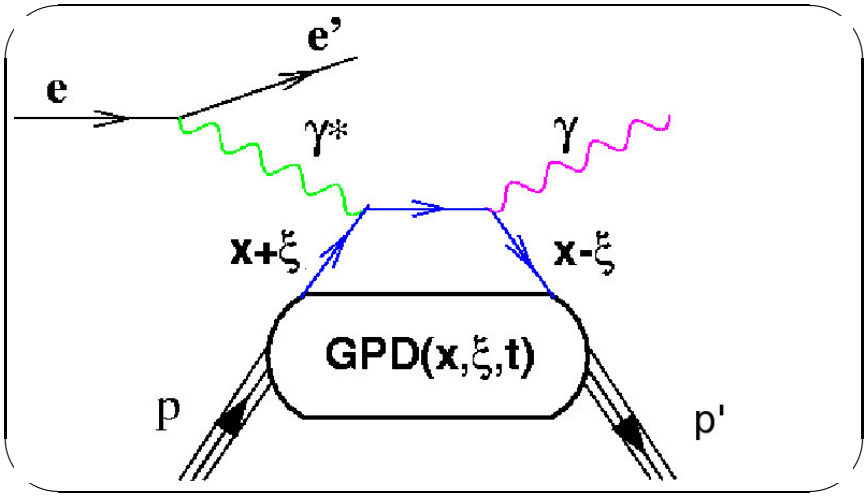

Figure 2.2: DVCS handbag diagram.

leading order process in the generalized Bjorken limit. Note that GPDs are defined at a starting scale μ^2 and their Q^2 evolution is generated by pertubative QCD with Q^2 being the photon virtuality. In Off-forward parton-distributions (OFPDs) [Ji98] the variables x, ξ and t are described in longitudinal lightcone coordinates (or the infinite momentum frame) by:

$$k^+ = xP^+ \qquad x \,\epsilon\, [-1,1] \tag{2.1}$$

$$\xi = \frac{-\Delta^+}{2P^+} \tag{2.2}$$

$$\Delta = P' - P \tag{2.3}$$

$$\Delta^2 = -t \tag{2.4}$$

with x (the average longitudinal momentum fraction of the involved parton with the momentum k) and the *skewedness* variable ξ (the longitudinal fraction of the momentum transfer Δ). The meaning of the longitudinal momentum fraction variables in the context of OFPD is that the parton with the longitudinal momentum fraction $x+\xi$ is removed from the proton and then put back with a longitudinal fraction $x-\xi$. Note that these longitudinal momentum fractions are either positive or negative if the active parton is a particle or antiparticle. In the Bjorken limit of large photon virtuality Q^2 and collision energy, the parameter ξ is related to x_{Bj}, the momentum fraction of the proton carried by the struck quark, as

$$\xi \simeq \frac{x_{Bj}}{2 - x_{Bj}}$$

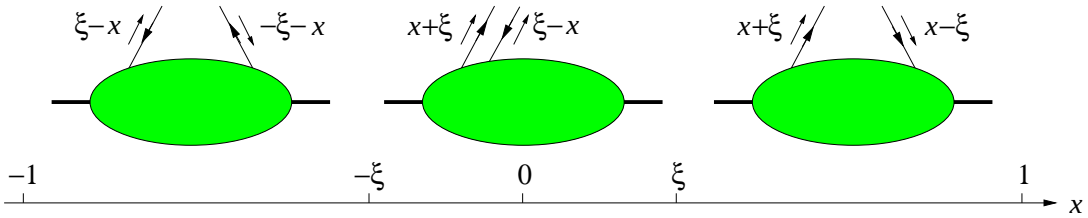

Figure 2.3: The parton interpretation of GPDs in the three x-intervals [-1,−ξ], [−ξ,ξ], and [ξ,1] [Die03].

- GPDs are defined in the interval $x \in [-1, 1]$, which is subdivided into three regions, shown in figure 2.3:

  1. for $x \in [\xi, 1]$: both momentum fractions $x+\xi$ and $x-\xi$ are positive, describing emission and reabsorption of a quark.
  2. for $x \in [-\xi, \xi]$: $x + \xi \geq 0$ and $x - \xi \leq 0$, interpreted as an antiquark with momentum fraction $\xi - x$ emitted from the initial proton.
  3. for $x \in [-1, -\xi]$: both momentum fractions $x + \xi$ and $x - \xi$ are negative, belonging to emission and reabsorption of antiquarks

  The first and third case are commonly referred to as DGLAP (Dokshitzer-Gribov-Lipatov-Altarelli-Parisi) regions and the second as ERBL (Efremov-Radyushkin-Brodsky-Lepage) region [Die03].

- In the case of the spin-1/2 nucleon the most important GPDs are the chirally-even GPDs $H^{q,g}$,$\tilde{H}^{q,g}$,$E^{q,g}$,$\tilde{E}^{q,g}$, defined for each quark flavor (q = u,d,s) and gluon (g). Chirally-even means here that they do not flip the parton helicity [HJ98]. They can be divided into unpolarized GPDs ($H^{q,g}$ and $E^{q,g}$) and polarized ones ($\widetilde{H}^{q,g}$ and $\widetilde{E}^{q,g}$). Of these, $H^{q,g}$ and $\widetilde{H}^{q,g}$ conserve the nucleon helicity, while $E^{q,g}$ and $\widetilde{E}^{q,g}$ can also flip it.
  The number of GPDs for spin-zero hadrons (pions and spin-zero nuclei, e.g. neon) is reduced to one GPD $H^{q,g}$ for each quark flavor and gluon [Die03].

- The first moments of the helicity-conserving GPDs are related to the elastic form factors of the nucleon [Ji97b]:

  $$\int_{-1}^{1} dx H^q(x,\xi,t) = F_1(t) \quad \text{Dirac form factor}$$

  $$\int_{-1}^{1} dx E^q(x,\xi,t) = F_2(t) \quad \text{Pauli form factor}$$

  $$\int_{-1}^{1} dx \widetilde{H}^q(x,\xi,t) = G_A(t) \quad \text{Axial-vector form factor}$$

  $$\int_{-1}^{1} dx \widetilde{E}^q(x,\xi,t) = G_P(t) \quad \text{Pseudo-scalar form factor}$$

  Since the result of the integration does not depend on ξ, one can choose $\xi = 0$. In

the limit of vanishing momentum transfer $t \longrightarrow 0$, the helicity conserving GPDs $H^q(x, \xi = 0, t)$ and $\widetilde{H}^q(x, \xi = 0, t)$ reduce to $H^q(x, \xi = 0, t = 0) \equiv q(x)$ and $\widetilde{H}q(x, \xi = 0, t = 0) \equiv \Delta q(x)$. For gluons they reduce to $H^g(x, \xi = 0, t = 0) = xg(x)$ and $\widetilde{H}^g(x, \xi = 0, t = 0) = \Delta xg(x)$. The reduced distributions are the ordinary spin-independent density $q(x)$ and spin-dependent density $\Delta q(x)$ for quarks and $xg(x)$, $\Delta xg(x)$ for gluons. The corresponding relation for the distributions $E^{q,g}$ and $\widetilde{E}^{q,g}$, which would express the "magnetic" density, can not be directly expressed in terms of any known parton distribution [GPRV04].

- The t-independent part of GPDs complies the polynomiality condition following from Lorentz invariance [Ji97b]

$$\int_{-1}^{1} dx\, x^N H^q(x, \xi) = h_0^{q(N)} + h_2^{q(N)} \xi^2 + \ldots + h_{N+1}^{q(N)} \xi^{N+1}, \tag{2.5}$$

$$\int_{-1}^{1} dx\, x^N E^q(x, \xi) = e_0^{q(N)} + e_2^{q(N)} \xi^2 + \ldots + e_{N+1}^{q(N)} \xi^{N+1}, \tag{2.6}$$

  where the coresponding polynomials contain only even powers of the parameter ξ due to time reversal invariance [MPW98, Ji98].
  In order to satisfy the polynomiality condition, a parameterization of GPDs can be defined by the Double Distribution (DD) formalism, which is completed by adding a D-term introduced by Polyakov and Weiss [PW99].

The present experimental knowledge on GPDs is presented in figure 2.4. The GPDs are placed in the middle of three concentric rings, the PDFs in the outermost and nucleon form factors in the innermost rings. Today's experimental knowledge of the different functions is illustrated in different colors from light (no data exist) to dark (well known). Note that for empty sectors no function exists or no strategy is known for its measurement. For more details see Ref. [Now02].

2.2 The Energy-Momentum Tensor and the Spin of the Nucleon

In order to understand the spin structure of the nucleon, the best way is to start with the QCD angular momentum operator in its gauge-invariant form . The sum of the quark and gluon contribution is given as [Ji03]:

$$\vec{J}_{QCD} = \vec{J}_q + \vec{J}_g$$

where

$$\vec{J}_q = \int d^3x\, \vec{x} \times \vec{T}_q$$

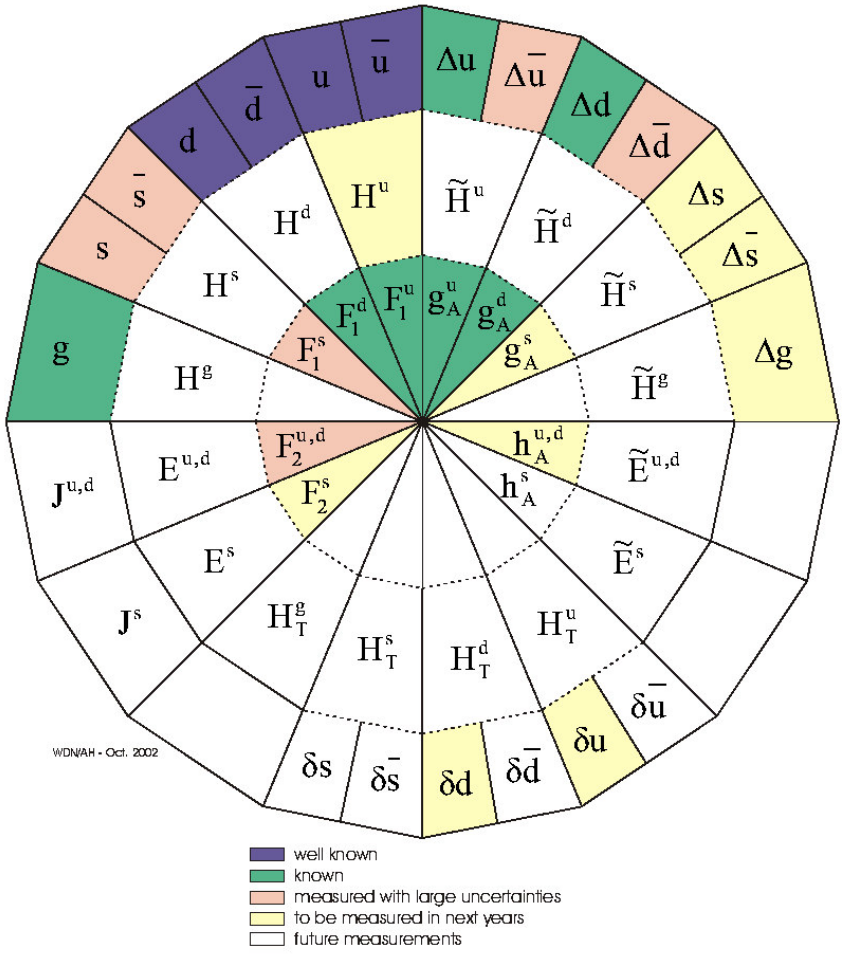

Figure 2.4: Visualization of the most relevant Generalized Parton Distributions and their limiting cases, forward Parton Distributions and Nucleon Form Factors [Now02].

and

$$\vec{J}_g = \int d^3x \; \vec{x} \times (\vec{E} \times \vec{B}).$$

Here $\vec{T}_q$ and $(\vec{E} \times \vec{B})$ are the quark and gluon momentum densities, respectively. The separation of the quark and gluon contributions to the nucleon spin can be deduced from an analogy with the magnetic moment, if the form factors of the momentum density are

known at zero momentum transfer t:

$$\mu = G_M(t=0) = F_1(t=0) + F_2(t=0),$$

where the spin-flip form factor $\Delta G_M(t) = q(F_1(t) + F_2(t))$ yields the electric current distribution in the nucleon with the Dirac and Pauli form factors of the electromagentic current $F_1(Q^2)$ and $F_2(Q^2)$. In analogy, the second moments of the parton distributions yield the form factors of the energy-momentum tensor,

$$\int_{-1}^{1} dx(H^{q,g}(x,\xi,t) + E^{q,g}(x,\xi,t))x = A(t) + B(t), \tag{2.7}$$

where the ξ dependence drops out. Extrapolating this relation to $t \to 0$, the total quark and gluon contribution to the nucleon spin is obtained:

$$J_{q,g} = \frac{1}{2}(A_{q,g}(0) + B_{q,g}(0)) \tag{2.8}$$

with

$$\frac{1}{2} = J_q + J_g. \tag{2.9}$$

The relation $L_q = J_q - \frac{1}{2}\Delta\Sigma$ offers the possibility to determine L_q through a measurement of J_q by using the information on the quarks spin contribution $\frac{1}{2}\Delta\Sigma$, which is available from inclusive and semi-inclusive polarized DIS.

In summary, the second moment of GPDs yield the total angular momentum

$$J^{q,g} = \lim_{t\to 0} \int_{-1}^{1} x[H^{q,g}(x,\xi,t) + E^{q,g}(x,\xi,t)]dx, \tag{2.10}$$

well know as Ji's relation.

2.3 Kinematics of Deeply Virtual Compton Scattering

Deeply Virtual Compton Scattering (DVCS) is the hard exclusive production of a real photon in lepton scattering

$$e(k) + P(p) \to e(k') + P(p') + \gamma(q'),$$

with the four-momentum of the incoming (outgoing) lepton $k(k')$, the initial (final) hadron $p(p')$ and the real photon q'. The exchanged virtual photon is described by the four-momentum $q = k - k'$. In analogy to ordinary Compton scattering, where a *real* photon is scattered on a charged particle, the DVCS process refers to *virtual*-photon scattering with a real photon being produced.

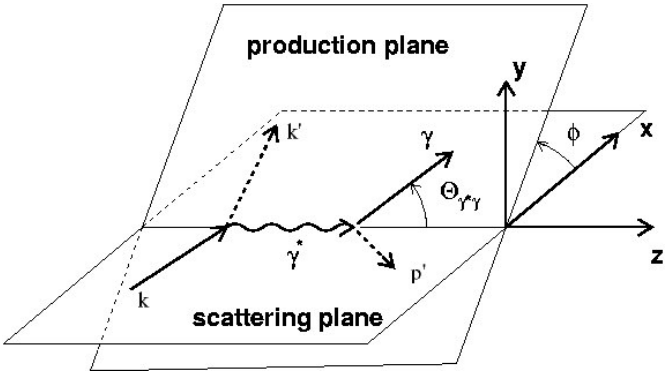

Figure 2.5: Diagram for Deeply Virtual Compton Scattering with the azimuthal angle ϕ between lepton scattering plane and photon production plane and the polar angle $\theta_{\gamma^*\gamma}$ between virtual and real photon.

The reaction of DVCS is defined in the generalized Bjorken limit of large photon virtuality and collision energy. DVCS is characterized through an reaction of the virtual photon with partons, where a real photon in the final state is produced, as illustrated in figure 2.5. The azimuthal angle ϕ is defined as angle between lepton scattering plane and photon production plane, given as

$$\phi = \arccos\left(\frac{(\overrightarrow{q}\times\overrightarrow{k'})(\overrightarrow{q}\times\overrightarrow{q'})}{|\overrightarrow{q}\times\overrightarrow{k'}||\overrightarrow{q}\times\overrightarrow{q'}|}\right)\frac{\overrightarrow{q'}\cdot\overrightarrow{q}\times\overrightarrow{k'}}{|\overrightarrow{q'}\cdot\overrightarrow{q}\times\overrightarrow{k'}|} \tag{2.11}$$

The angle between virtual and real photon is $\theta_{\gamma^*\gamma}$, defined as

$$\theta_{\gamma^*\gamma} = \arccos\left(\frac{\overrightarrow{q}\cdot\overrightarrow{q'}}{|\overrightarrow{q}||\overrightarrow{q'}|}\right). \tag{2.12}$$

The following kinematic variables are defined:

- The photon virtuality,

$$Q^2 \equiv -q^2 = -(k-k')^2 \overset{lab}{\cong} 4EE'sin^2(\frac{\theta}{2}) \tag{2.13}$$

  with the lepton energies E and E'.

- The momentum fraction of the proton carried by the struck quark (Bjorken variable),

$$x_{Bj} \equiv \frac{Q^2}{2pq} = \frac{Q^2}{2M_n\nu} \tag{2.14}$$

  with the mass of the nucleon M_n.

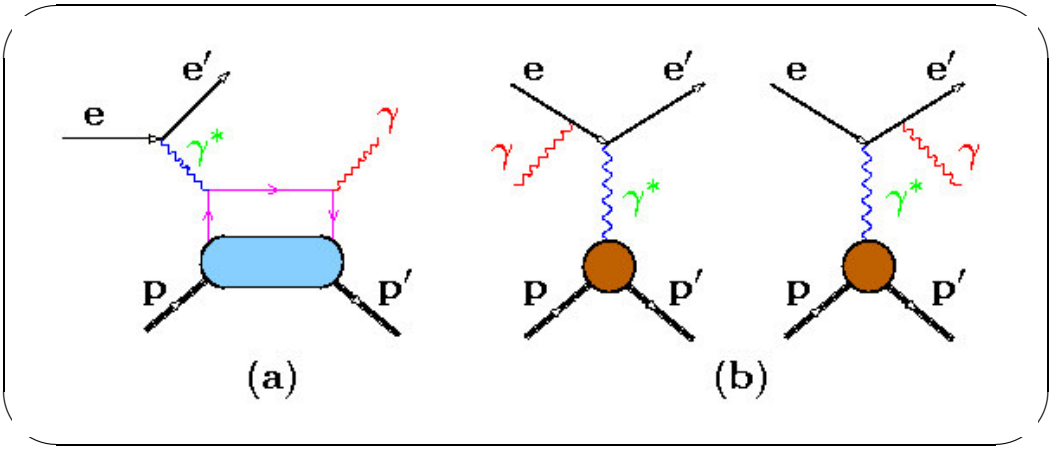

Figure 2.6: Diagrams for the DVCS process (a) and the BH process (b). In the latter a photon can be radiated by the incoming or outgoing lepton.

- The energy of the virtual photon,

$$\nu \equiv \frac{pq}{M_n} \overset{lab}{=} E - E'. \tag{2.15}$$

- The fractional energy of the virtual photon to the beam energy,

$$y \equiv \frac{pq}{pk} \overset{lab}{=} \frac{\nu}{E}. \tag{2.16}$$

- The invariant mass of the system of virtual photon and proton (squared energy in the photon-proton center-of-mass system),

$$W^2 = (q+p)^2 = M_n^2 + 2M_n\nu - Q^2. \tag{2.17}$$

- The four-momentum transfer to the nucleon,

$$t = (p-p')^2 = (q-q')^2. \tag{2.18}$$

2.4 Beam-Spin and Beam-Charge Asymmetries

In fact, not only the DVCS process produces a real photon in the final state. Photons are also emitted by leptons through Bremsstrahlung, characterized by the so-called Bethe Heitler (BH) process. In figure 2.6 both processes are shown. The DVCS process can not be separated from the BH process, because the final states are indistinguishable; the scattering amplitudes of the two interfering processes add coherently.

The square of the photon production amplitude receives contributions from pure DVCS (τ_{DVCS}) and pure BH (τ_{BH}) and from their interference

$$|\tau|^2 = |\tau_{BH}|^2 + |\tau_{DVCS}|^2 + \tau^*_{BH}\tau_{DVCS} + \tau^*_{DVCS}\tau_{BH} \tag{2.19}$$

with the DVCS-BH interference term

$$I = \tau^*_{BH}\tau_{DVCS} + \tau^*_{DVCS}\tau_{BH}. \tag{2.20}$$

The corresponding five-fold differential cross section for a spin-0 target (e.g. neon) per nucleon is given as [FS04]

$$\frac{1}{A}\frac{d\sigma}{dx_{Bj}dyd|t|d\phi d\varphi} = \frac{\alpha^3_{em}x_{Bj}y}{16\pi^2Q^2\sqrt{1+4x^2_{Bj}\frac{M^2_N}{Q^2}}A^3}|\frac{\tau}{e^3}|^2 \tag{2.21}$$

with the fine-structure constant α_{em}, the charge of the lepton e, the atomic number A of the nucleus with the mass M_N and the angle φ between the target polarization vector and the hadron if the hadron is transversely polarized. Note that the nuclear amplitudes are given per nucleon, and in order to obtain the correct scaling of the cross section with A, the DVCS amplitude has to be multiplied by A.

In the case that the BH cross section is not dominating the DVCS cross section, it is possible to obtain the DVCS cross section through a measurement of the full cross section subtracting the BH cross section. Note that the BH cross section is exactly calculable in Quantum Electrodynamics (QED). The measurement of the DVCS cross section has been done in the collider experiments H1 [H101] and Zeus [HZ] at DESY. Since HERMES is a fixed-target experiment, its kinematic region is disjunct from that of the collider experiments which measure at small x. Here the BH cross section mostly dominates the DVCS cross section and the subtraction of the calculated BH cross section might lead to large uncertainties.

In contrast, the BH-DVCS interference term I offers the possibility to directly access the DVCS amplitudes. The three parts of the photon production cross section 2.19, expanded in Fourier series, are for an unpolarized target [BMK02]

$$|\tau_{BH}|^2 = -\frac{e^6}{x^2_{Bj}y^2(1+\frac{4M^2_Nx^2_{Bj}}{Q^2})^2tP_1(\phi)P_2(\phi)}\left(c^{BH}_0 + \sum_{n=1}^{2}c^{BH}_n\cos n\phi\right), \tag{2.22}$$

$$|\tau_{DVCS}|^2 = \frac{e^6}{y^2Q^2}\left(c^{DVCS}_0 + \sum_{n=1}^{2}c^{DVCS}_n\cos n\phi + s^{DVCS}_1\sin\phi\right), \tag{2.23}$$

$$I = \frac{\pm e^6}{x_{Bj}y^3tP_1(\phi)P_2(\phi)}\left(c^I_0 + \sum_{n=1}^{3}c^I_n\cos n\phi + \sum_{n=1}^{2}s^I_n\sin n\phi\right), \tag{2.24}$$

where the +/- sign in the interference term I stands for a negatively/positively charged incident lepton. In the squared BH term $|\tau_{BH}|^2$ and in the interference term I, an additional ϕ dependence arises from the scaled lepton BH propagators $P_i(\phi) = A_i + B_i\cos\phi$.

The c_n and s_n are the Fourier coefficients and depend on the variables y, x_{Bj}, t, Q^2. For an unpolarized target the helicity-dependent coefficients are given by

$$\begin{aligned} s_1^I &= \lambda 8Ky(2-y)\, \Im m\left\{C^I\right\} \\ s_1^{DVCS} &= -\lambda 8K/(2-x_{Bj})y\, \Im m\left\{C^{DVCS}\right\} \\ s_2^I &= -\lambda 16K^2/(2-x_{Bj})y\, \Im m\left\{C^I\right\} \end{aligned}$$

with $K \simeq \sqrt{(1-x_{Bj})(1-y)}\frac{\Delta_\perp}{Q}$, where $\Delta_\perp$ is the transverse momentum transfer, and λ is the lepton helicity. The C's are linear combinations of the Compton form factors (CFFs) $\mathcal{F} = \{\mathcal{H}, \widetilde{\mathcal{H}}, \mathcal{E}, \widetilde{\mathcal{E}}\}$, which have been worked out in Ref. [BMK02]. At leading order in α_s, the function C^I for an unpolarized target is given by

$$C^I = F_1\mathcal{H} + \frac{x_{Bj}}{2-x_{Bj}}(F_1+F_2)\widetilde{\mathcal{H}} - \frac{\Delta^2}{4M^2}F_2\mathcal{E}$$

where F_1 and F_2 are the nucleon Dirac and Pauli form factors, respectively.

In order to get access to the helicity-dependent Fourier coefficients, one has to measure the beam-spin asymmetry, defined as [BMK02]

$$A_{LU}(\phi) = \frac{d\overrightarrow{\sigma} - d\overleftarrow{\sigma}}{d\overrightarrow{\sigma} + d\overleftarrow{\sigma}}. \tag{2.25}$$

This cross section asymmetry is built from two measurements with opposite beam helicity, denoted by arrows with opposite orientation. The indices L and U of the asymmetry A denote the longitudinal polarized beam and the unpolarized target.
By inserting the Fourier coefficients [BMK02] in the cross sections of equations 2.22 - 2.24, the beam-spin-asymmetry A_{LU} can be expressed as

$$\frac{d\overrightarrow{\sigma} - d\overleftarrow{\sigma}}{d\overrightarrow{\sigma} + d\overleftarrow{\sigma}} = \frac{\frac{e^6}{y^2Q^2}s_1^{DVCS}\sin\phi \pm \frac{e^6}{x_{Bj}y^3tP_1(\phi)P_2(\phi)}(s_1^I\sin\phi + s_2^I\sin 2\phi)}{|\tau_{BH}|^2 + \frac{e^6}{y^2Q^2}(c_0^{DVCS} + \sum_{n=1}^{2} c_n^{DVCS}\cos n\phi) \pm \frac{e^6(c_0^I + \sum_{n=1}^{3} c_n^I\cos n\phi)}{x_{Bj}y^3tP_1(\phi)P_2(\phi)}}.$$

To leading order in α_s and neglecting DVCS and interference part in the denominator it reduces to:

$$A_{LU}(\phi) \simeq \pm\frac{x_{Bj}}{y}\frac{s_1^I}{c_0^{BH}}\sin\phi \tag{2.26}$$

where the $+(-)$ sign stands for a negative (positive) charged lepton beam. Note that the BH-coefficient c_0^{BH} is exactly calculable in quantum-electrodynamics. In this approximation, the asymmetry A_{LU} is proportional to $\sin\phi$ and s_1^I, the Fourier-coefficient of the interference part, which is given as $s_1^I = \lambda 8Ky(2-y)\, \Im m\left\{C^I(\mathcal{F})\right\}$. With

$$\Im m\left\{\mathcal{F}\right\} = \pi\sum_q e_q^2(F^q(\xi,\xi,t) - F^q(-\xi,\xi,t)) \tag{2.27}$$

the imaginary part directly probes the respective GPDs $F^q = \{H, \widetilde{H}, E, \widetilde{E}\}$ along the line $x = \pm\xi$.

Another possibility to get access to the Fourier coefficients is provided by the beam-charge asymmetry [BMK02]

$$A_C(\phi) = \frac{d\sigma^+ - d\sigma^-}{d\sigma^+ + d\sigma^-} \tag{2.28}$$

where $d\sigma^+$ and $d\sigma^-$ denote the cross section measurement with a positron and an electron beam, respectively. This cross section difference directly projects out the interference term I, since it is the only term depending on the charge, indicated by the sign $\pm$ in equation 2.24. Assuming unpolarized beam ($\lambda = 0$) and to leading power $1/Q$, the beam-charge asymmetry at leading order in α_s is approximately given as

$$A_C(\phi) = -\frac{x_{Bj}}{y}\frac{c_1^I}{c_0^{BH}}\cos\phi \tag{2.29}$$

with $c_1^I = -8K(2 - 2y + y^2)\ \Re e\left\{C^I(\mathcal{F})\right\}$. Consequently, the beam-charge asymmetry for an unpolarized beam has a $\cos\phi$ dependence and is proportional to the real part of $C^I(\mathcal{F})$. The real part of the Compton form factor

$$\Re e\left\{\mathcal{F}\right\} = -\sum_q e_q^2 \left[P\int_{-1}^{1} dx\ F^q(x,\xi,t)\left(\frac{1}{x-\xi} \pm \frac{1}{x+\xi}\right)\right], \tag{2.30}$$

gives access to the integral over the respective GPDs, where P denotes the Cauchy's principal value.
Since neon data at HERMES is presently only available for one lepton beam charge (positrons), the beam-charge asymmetry will not be further discussed in this thesis.

2.5 Deeply Virtual Compton Scattering on Nuclei

The measurement of DVCS on the proton has shown the possibility to provide a sensitive test of current models of GPDs [Ell, Kra]. Such studies open also access to questions of the properties of quark and gluon matter inside nuclei. Consequently, nuclear DVCS allows the study of the modification of parton correlations encoded in GPDs within a nuclear environment. Hence it may shed new light on the dynamical interplay of highly complex bound hadronic systems.

In the case of the simplest nucleus, the deuteron, which can be seen as a weakly bound state of a proton and a neutron, first results have already been published [HERMES03]. In comparison to the deuteron, described by two-body wave functions ψ_{p+n} and their transition GPDs, it is even more complicated to work out a theoretical prediction for

heavier nuclei, as the number of wave functions increases with the atomic number of the hadron.

The number of GPDs also depends on the spin of the hadron: for spin-1 nuclei (i.e. Deuteron) 9 GPDs, for spin-$\frac{1}{2}$ nuclei 4 GPDs and for spin-0 nuclei (i.e. Neon) only one GPD for each parton. In the case of Neon it reduces to the GPD $H^{q,g}$ [Die03].

For a nuclear target there exist two distinct processes, both in DVCS and BH:

1. The scattering proceeds coherently, i.e. the target nucleus recoils as a whole while emitting a photon with momentum $q\prime$, as illustrated in the left panels of figure 2.7 [LT05a].
2. The scattering proceeds incoherently, i.e. the nucleus undergoes a breakup and the final photon is emitted from a quasi-elastically scattered nucleon, as shown in the right panels of figure 2.7.

The extension to the case of heavier spin-0 nuclei has been considered, among others, by Guzey and Strikman [GS03] and is explained in the following. In order to obtain an estimate of the change of A_{LU}, the ratio of nuclear to proton asymmetries $\frac{A_{LU}^{nucleus}}{A_{LU}^{Proton}}$ has been calculated in the limit $t = 0$:

$$\frac{A_{LU}^{nucleus}(\phi)}{A_{LU}^{Proton}(\phi)} = \frac{H^p(\xi,\xi,0) - H^p(-\xi,\xi,0) + (\frac{A}{Z} - 1)\left(H^n(\xi,\xi,0) - H^n(-\xi,\xi,0)\right)}{H^p(\xi,\xi,0) - H^p(-\xi,\xi,0)}. \quad (2.31)$$

Note it was assumed that the process is a coherent reaction.

Since both coherent and incoherent contributions enter the total cross section, the expression for A_{LU} should be modified. The modified asymmetry $A_{LU}^{nucleus}$ becomes [GS03]:

$$A_{LU}^{nucleus}(\phi) = sin(\phi)\frac{K8y(2-y)x_{Bj}}{yc_0^{BH}}$$

$$\times\frac{\left(Z\left(H^p(\xi,\xi,t) - H^p(-\xi,\xi,t)\right) + Z(A-1)F_A^{e.m.}(t')\left(H^p(\xi,\xi,t') - H^p(-\xi,\xi,t')\right)\right)}{ZF_1(t) + Z(Z-1)(F_A^{e.m.}(t'))^2} \quad (2.32)$$

with $t' = t\frac{A}{A-1}$. Figure 2.8 shows a schematic representation of the origin of the combinatorial factors Z and $Z(A-1)$. The first term in nominator and denominator of equation 2.32 describes the contribution from the "in" and "out" states to the same nucleon (incoherent term), which at small t is proportional to the number of protons, Z, times the GPD H of the free proton. This contribution has a slow t-dependence due to the proton elastic form factor $F_1(t)$. Note that the neutron contribution is suppressed by the smallness of the electromagnetic form factors and can therefore be neglected. The contribution given by the second term in the nominator and denominator describes the

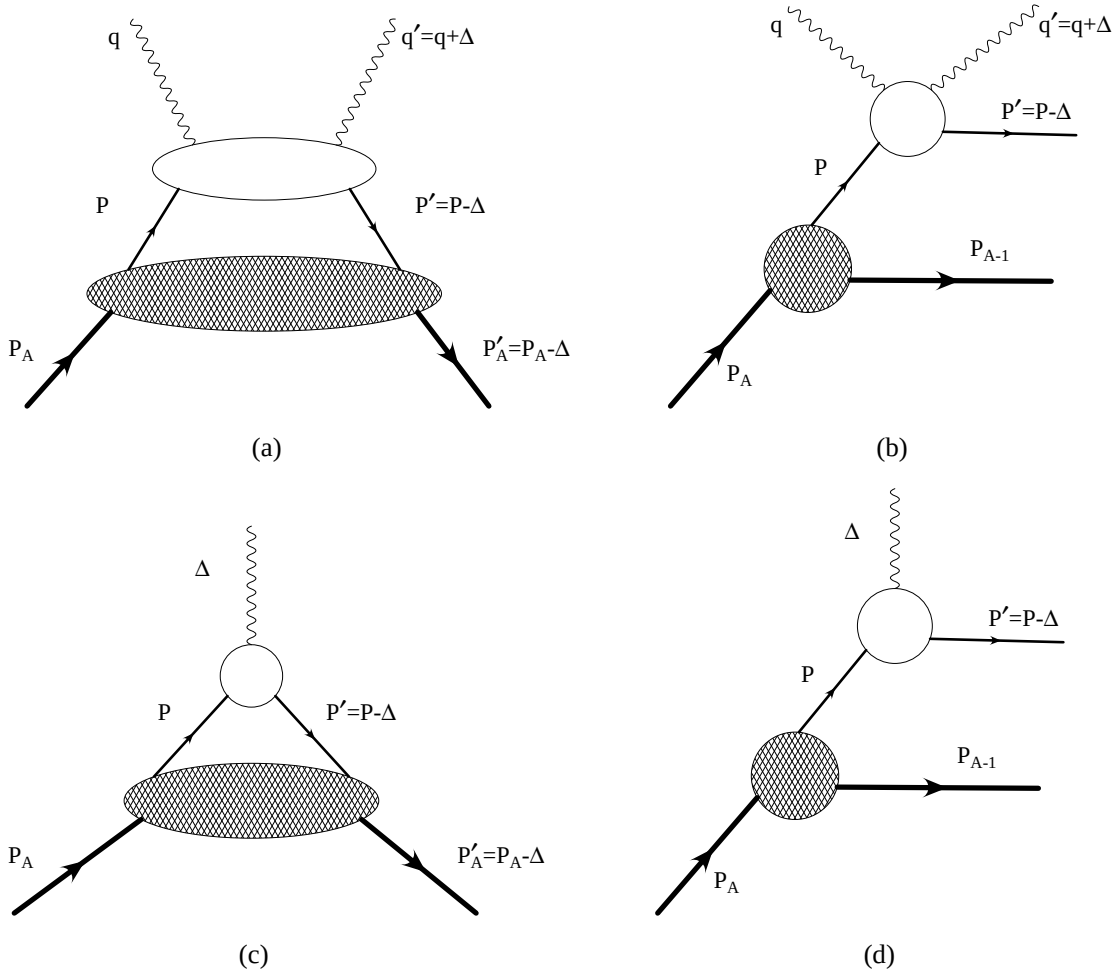

Figure 2.7: Diagrams for DVCS and BH processes from a nuclear target at leading order in α_s. (**a**) DVCS, coherent process; (**b**) DVCS, incoherent process; (**c**) BH, coherent process; (**d**) BH, incoherent process [LT05a].

$Z(A-1)$ attachments of BH to the proton and DVCS to a different nucleon. It is mostly coherent and has a much steeper t-dependence, forced by the nuclear charge form factor $F_A^{e.m.}(t)$.

Since the DVCS measurement does not allow to extract only purely coherent DVCS events, the measured asymmetries present a sum of the coherent and incoherent contributions, as given by equation 2.32. A simulation of the ratio of asymmetries in the cases of neon ($A = 20$ and $Z = 10$) and krypton ($A = 76$ and $Z = 36$) is presented in figure 2.9. While $\frac{A_{LU}^{nucleus}}{A_{LU}^{proton}}$ is significantly larger than unity for coherent nuclear DVCS (expected to be close to the factor of 2 for $t \to 0$), $\frac{A_{LU}^{nucleus}}{A_{LU}^{proton}} \simeq 1$ for the incoherent part. Consequently, the inclusion of the incoherent contribution should decrease the ratio of

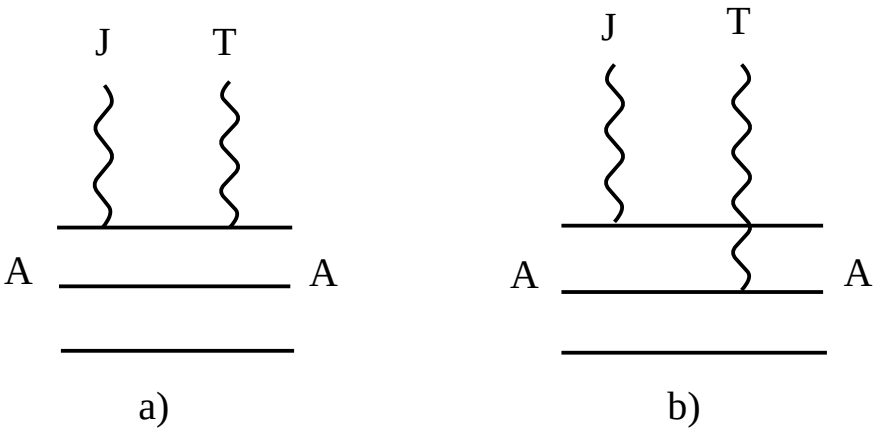

Figure 2.8: Schematic representation of the interference between the BH (J) and DVCS (T) amplitudes in nuclei: There are Z attachments of both J and T to the same proton (a) and $Z(A-1)$ attachments of J to the proton and T to a different nucleon (b) [GS03].

the asymmetries.

A quantitative evaluation of the coherent and incoherent contributions to the ratio of the nuclear BSA over the proton BSA has been worked out in a different model [LT05a, LT05b]. In this model off-shell effects are quite noticeable and an enhancement of the ratio $A_{LU}^{nuclear}/A_{LU}^{proton}$ for higher t is predicted. In figure 2.10 the ratio of nuclear-to-proton asymmetries A_{LU}^{A}/A_{LU}^{p} for ^{4}He is shown, calculated including only coherent scattering terms in both the DVCS and BH contributions to the asymmetry (dashed line), and including only the incoherent terms (dot-dashed line). In these calculations the nuclear model included off-shell effects.

An additional dependence on the atomic number A has been predicted in a study [Pol03] using a model for a large nucleus. A characteristic A-dependence of the D-term was obtained in connection with the spatial components of the energy-momentum tensor. In fact, a conclusion of this study implies, that the contribution of the D-term to the real part of the DVCS amplitude grows with an increase of the atomic number as $A^{4/3}$. It is also mentioned as a general possibility that detailed information about deviations of energy, pressure, and shear forces distributions inside nuclei can be accessed.

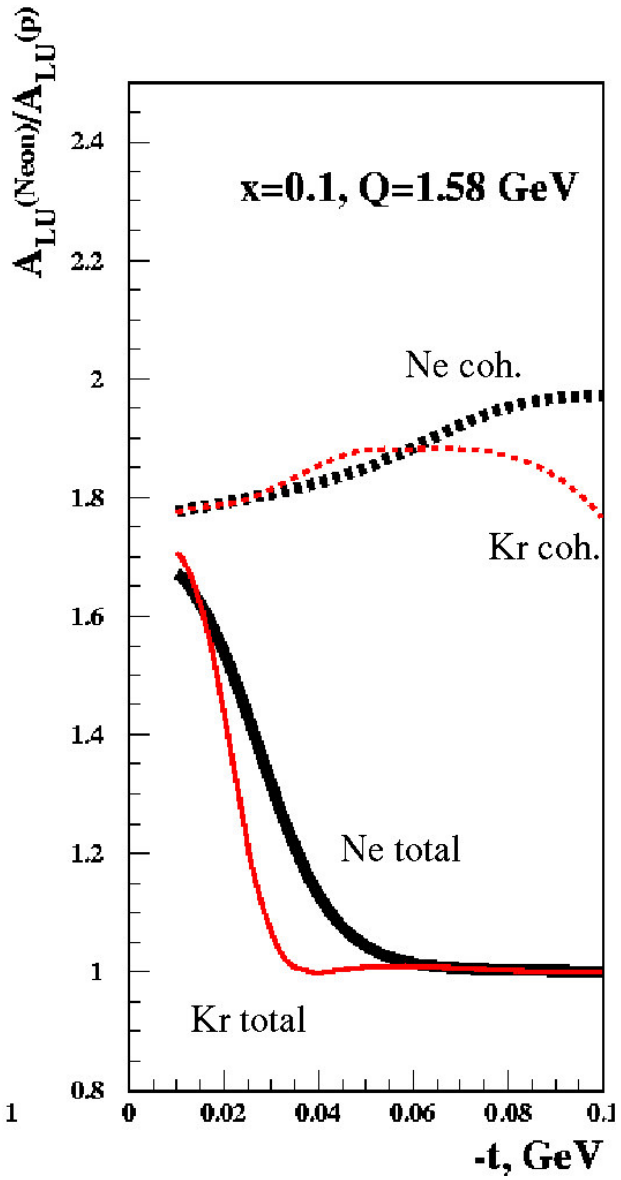

Figure 2.9: The ratio of nuclear to proton asymmetries $A_{LU}^{nuclear}/A_{LU}^{proton}$ for Neon (thick) and Krypton (thin), solid curves for both coherent and incoherent, dashed curves include only the coherent part [GS03].

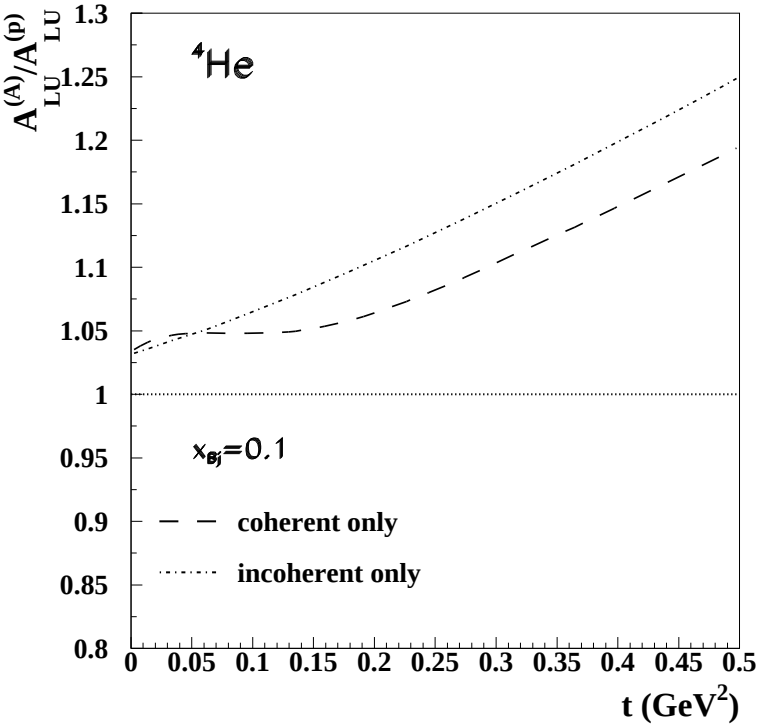

Figure 2.10: The ratio of nuclear to proton asymmetries A_{LU}^A/A_{LU}^p for ^{4}He, calculated including only coherent scattering terms in both the DVCS and BH contributions to the asymmetry (dashed line), and including only the incoherent terms (dot-dashed line). The nuclear model including off-shell effects was used in these calculations [LT05a].

3 The HERMES Experiment

The aim of the HERMES (HERa MEasurement of Spin) experiment is the investigation of the spin structure of the nucleon. The HERMES experiment is located in the East Hall of the HERA (Hadron Elektron Ring Anlage) storage ring complex at DESY, using the polarized lepton beam for scattering off a fixed gas target. The physics program for HERMES is very broad. The experiment was inspired by the flavour decomposition of the nucleon spin. In addition it contributes inclusive data with qualitatively different systematic uncertainties to improve the world data set for the x dependence and the integral of the spin structure function $g_1(x)$. A novel aspect of the experiment is its capability to perform measurements of exclusive processes, even though it was originally conceived as an experiment of inclusive and semi-inclusive physics.

3.1 The HERA Storage Ring Facility

The underground storage ring facility HERA has a circumference of 6.3 km and consists of two beam lines for the 27.57 GeV/c electron (positron) and the 920 GeV/c proton beam respectively. Both beams can be used simultaneously by four different experiments. Two of these experiments, ZEUS and H1, are colliding-beam experiments. HERA-B uses only the proton beam, whereas HERMES accumulates data only with the polarized lepton beam. After the start of HERMES in 1995 the lepton ring was operating with positrons, except for a short period in 1998. As recently as the beginning of 2005, data taking with electrons has again started.

The lepton beam consists of 189 individual bunches, which have a 96 ns (29 m) separation. Each lepton bunch is 27 ps (8 mm) long and contains $2 \cdot 10^{10}$ particles. The average lifetime of the lepton beam is around 10 hours with a starting intensity of 50 mA which decreases to 10 mA. After that, the beam is usually dumped or a one hour special HERMES run with high gas density follows.

The lepton beam is initially unpolarized after injection, but due to the Sokolov-Ternov effect [ST64], a parallel polarization to the magnetic dipole fields is naturally build up. That means the beam is polarized in the transverse direction, *i.e.* the beam spin orientation is perpendicular to the momentum. The Sokolov-Ternov effect can be described as a small asymmetry in the spin-flip probability in the emission of synchroton radiation. Hence the beam polarization increases exponentially in time, with a rise-time of about 25

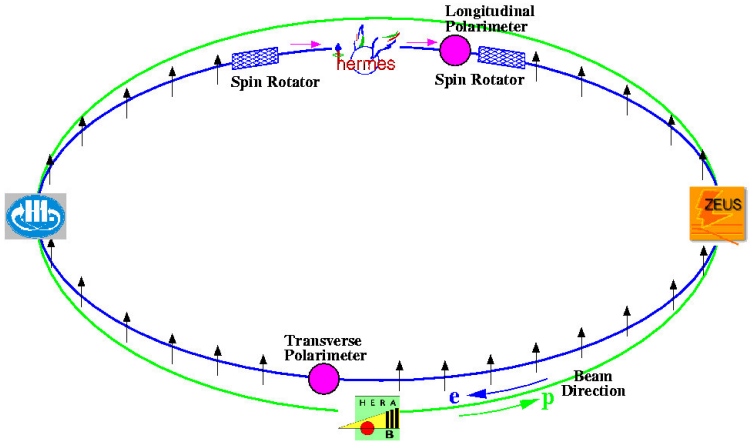

Figure 3.1: Schematic view of the HERA collider

minutes. In fact, depolarization effects limit the achievable polarization. The main contribution arises from non-vertical magnetic field components with respect to the beam orbit. These non-vertical magnetic fields are caused by small magnet misalignments and not perfectly homogenous magnetic fields. Furthermore, the interaction of the lepton and proton beam in the interaction regions of HERA may reduce the beam polarization.

In order to reduce the influence of depolarization effects, the so-called *harmonic-bump* method is used [B$^+$94]. This scheme introduces additional vertical closed-orbit corrections at strategic locations to compensate the effect of the spin-orbit distortions. At HERA there are eight *harmonic bumps* available and helped to achieve up to 60% polarization in the year 2000. Note that the polarization is defined as

$$\frac{N^{\uparrow} - N^{\downarrow}}{N^{\uparrow} + N^{\downarrow}}$$

whereby $N^{\uparrow}$ ($N^{\downarrow}$) refers to the number of leptons with their spin aligned parallel (antiparallel) to the magnetic dipole field.

For the study of the helicity structure of the nucleon, a longitudinally polarized lepton beam is required, i.e., the lepton spins have to be aligned parallel to their propagation direction. Therefore, before and after the interaction region, a pair of 90^o spin rotators have been installed, to turn the spin into the beam direction and then back into the vertical again. In figure 3.1 the spin rotators can be seen, one upstream and the other one downstream of the HERMES experiment. They consist of a sequence of horizontal and vertical beam normal conductor magnets.

The beam polarization is measured by two independent polarimeters, one for the transverse polarization (TPOL) and the other one for measuring the longitudinal beam polarization (LPOL). For the determination of the polarization, both use asymmetries in

the Compton scattering of polarized laser light off the lepton beam. The transverse polarimeter [B$^+$93, B$^+$94], measures the polarization of the lepton beam at a point where it is polarized in transverse direction. The polarization measurement is based on a spatial asymmetry effect in the back-scattering of laser light off the polarized lepton beam. These back-scattered photons are measured in a split lead-scintillator sampling calorimeter, where the change in the position of the photons with initial circular polarization determines the polarization of the lepton beam.

The second polarimeter, the LPOL [B$^+$02], measures the longitudinal polarization of the beam when crossing the experiment. It is also based on Compton back-scattering of laser light, but instead of the spatial distribution the asymmetry in the total cross-section is used. The larger asymmetry in this case allows a more precise measurement of the polarization. In addition, the polarization is measured for each individual lepton bunch in HERA. Furthermore the existence of two polarimeters provides the possibility for a cross-check of the polarization measurement.

3.2 The Internal Gas Target

Since a storage ring can not be operated with a liquid or solid target, the use of a gas target was mandatory for the HERMES experiment. The target system comprises the Atomic Beam Source (ABS), the internal storage cell and the target monitor system with the Target Gas Analyzer (TGA) and the Breit Rabi Polarimeter (BRP). The ABS-system consists of a dissociator to form atoms, a skimmer and a collimator for the formation of the atomic beam, a sextuple magnet system to sample out unwanted electron polarization, and high frequency units to transfer the polarization of electrons to nucleons. In figure 3.2 a schematic view of the HERMES ABS-system is presented. It is also possible to inject unpolarized gases into the storage cell by the unpolarized gas feed system (UGFS). The density of unpolarized gas can be up to two orders of magnitude larger in comparison to the density of polarized gas, which is at the maximum achievable value for present technology. Since the start of HERMES, a variety of pure unpolarized gas targets was used like H, D, He, N, Ne, Kr, Xe.

The target region is shown schematically in figure 3.3. The gas enters an open-ended tube that confines the gas atoms in a region around the positron beam. The storage cell increases the areal target density by about two orders of magnitude compared to a free atomic beam. The cryogenically cooled storage cell is an elliptical tube, 9.8 mm high by 29 mm wide and 400 mm in length made of ultra-pure aluminum with a uniform wall thickness of 75 μm [HERMES98]. At the open ends of the target cell the gas atoms, which leak out, are pumped away. Particles, emerging from the interaction, which are scattered into the spectrometer acceptance, exit the target chamber through a thin (0.3 mm) stainless steel foil.

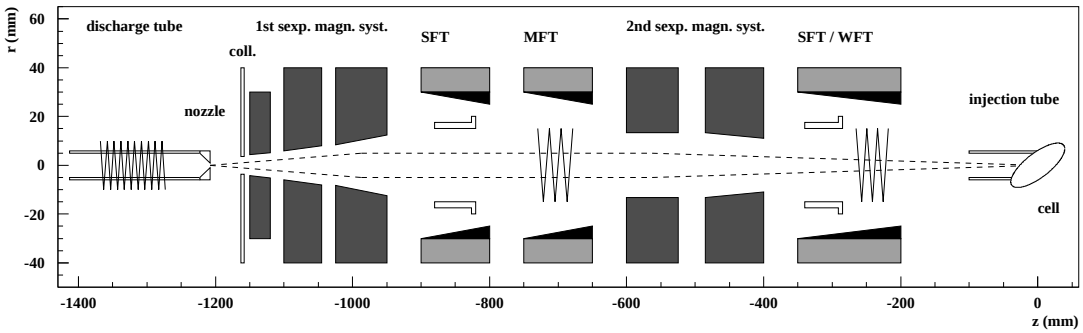

Figure 3.2: Schematic view (seen against the electron beam) of the HERMES ABS with dissociator and collimator for beam formation. Two sets of sextuple magnets are located along the axis of the gas jet. The axis of the ABS is tilted by 30° downwards with respect to the horizontal plane.

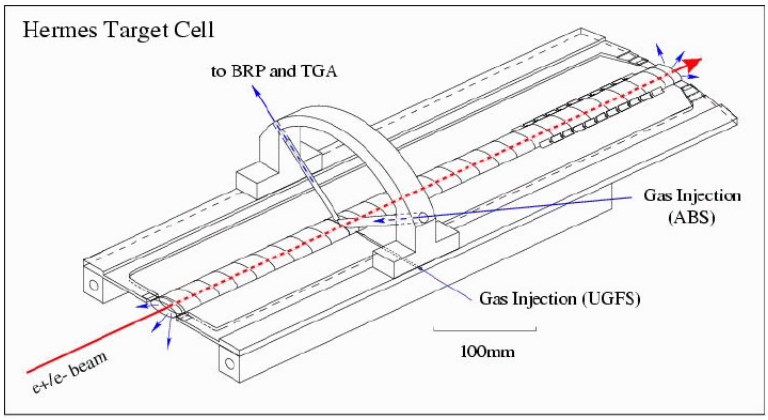

Figure 3.3: Schematic view of the target cell.

In order to decrease the amount of synchroton radiation, two collimator are installed near the target. In addition, the synchroton radiation is reduced by two weak dipoles downstream of the last bending magnet in the arc of the accelerator.

3.3 The HERMES Spectrometer

The HERMES spectrometer [HERMES98] is an open-aperture forward spectrometer, consisting of two symmetric halves above and below a central shielding plate in the beam plane. A schematic view of the spectrometer is shown in figure 3.4. The coordinate

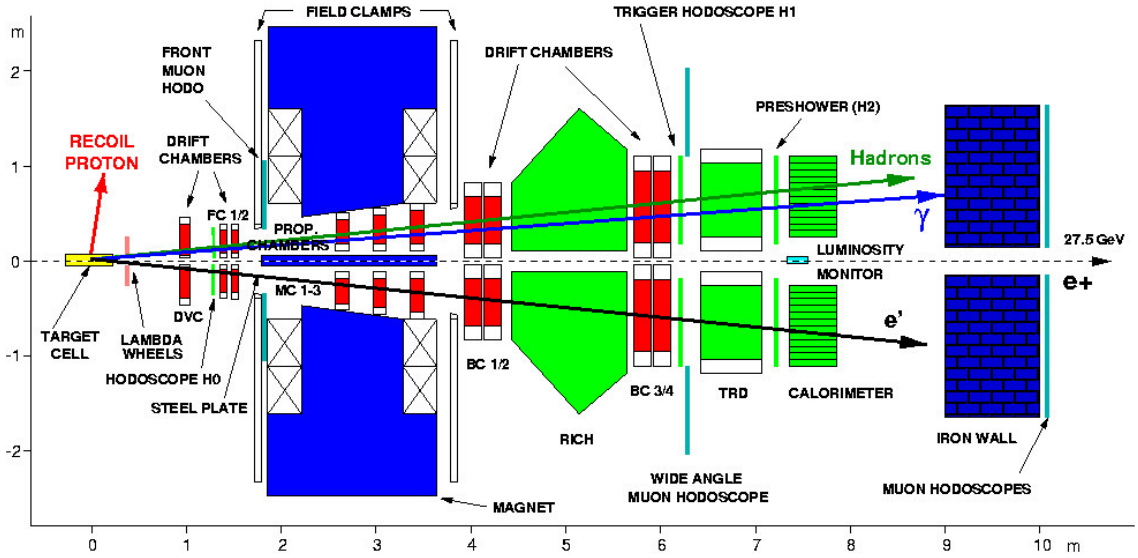

Figure 3.4: Schematic side view of the HERMES experiment. The incoming lepton beam enters from the left side of the picture.

system of HERMES is defined by the z axis pointing along the beam direction, the y axis oriented vertical upwards, and the x axis horizontal, pointing towards the outside of the ring. The polar and azimuthal scattering angles, as well as the initial trajectory for the determination of the momentum of the particle, are measured by the front tracking system, which consists of the Vertex Chamber (VC) and the Drift Chambers (DVC, FCs). Two sets of drift chambers behind the magnet (BCs) are used for the momentum measurement of leptons. In addition, three chambers in the magnet (MCs) help to match front and back tracks as well as to track low momentum particles.

The particle identification (PID) is provided by a combination of signals from the electromagnetic calorimeter, the preshower detector (H2), the Transition Radiation Detector (TRD), a threshold Cerenkov detector (C) [before 1998] or a Ring-Imaging Cerenkov counter (RICH) [after 1998]. Since the electromagnetic calorimeter is the only detector able to measure the position and energy of the photon, it is the most important detector for this analysis.

The acceptance is limited at small angles by an iron plate in the beam plane, which shields the lepton and proton beams from the magnetic field of the spectrometer magnet. Therefore, the range of scattering angles is 40 mrad to 220 mrad. The range for the variable x, which defines the momentum fraction of the proton carried by the struck quark, is 0.02-1.0 in the HERMES kinematics.

3.3.1 The Tracking System

The kinematics of charged particles traversing the spectrometer are reconstructed by the tracking system, which comprises several detectors, before, inside and behind the spectrometer magnet. The following tasks have to be performed by the tracking system:

- Measurement of the scattering angles for kinematic reconstruction.
- Determination of the event vertex in the target region.
- Measurement of the particle momentum from the track deflection in the spectrometer dipole magnet
- Identification of the hits in the PID detectors associated with each track.

The tracking system consists of 51 planes of wire chambers. The vertex reconstruction and the determination of the scattering angles is provided by the front tracking system, which consists of the drift vertex chambers (DVC) and the front drift chambers FC1,2. In order to determine the track momentum of the charged particles, a combination of the front tracking information with the signals of the back drift chambers BCs is performed. These BCs measure the charged tracks behind the spectrometer magnet. The latter has an integrated field strength of 1.3 Tm and contains three proportional chambers. These so-called Magnet Chambers (MCs) helps resolving multi-tracks and provide the analysis of low energy tracks, which do not reach the BCs. The momentum resolution of the HERMES spectrometer ranges from 1.5 to 2.5% [HERMES05]. The uncertainty in the scattering angle is better than 0.6 mrad.

3.3.2 The Particle Identification

In order to achieve a high efficiency lepton-hadron separation, the responses of various dedicated detectors are combined. The particle identification system consists of the RICH counter, the TRD, two sets of hodoscopes (H1,2), and the electromagnetic calorimeter. At HERMES, particles are identified using a probabilistic algorithm that utilizes the response of these four detectors. The resulting logarithmic ratio of the hadron and lepton probability is commonly called PID. The responses of the four PID detectors are combined into probabilities using a Bayesian algorithm, which maximizes the lepton-hadron separation.

The PID code associates each track with the responses of each PID detector module along the track. With these responses, calculations are performed and the result are parameters called PID2 through PID5, which correspond to the probability that a particular track was a lepton rather than a hadron. For a track with a particular momentum p and the

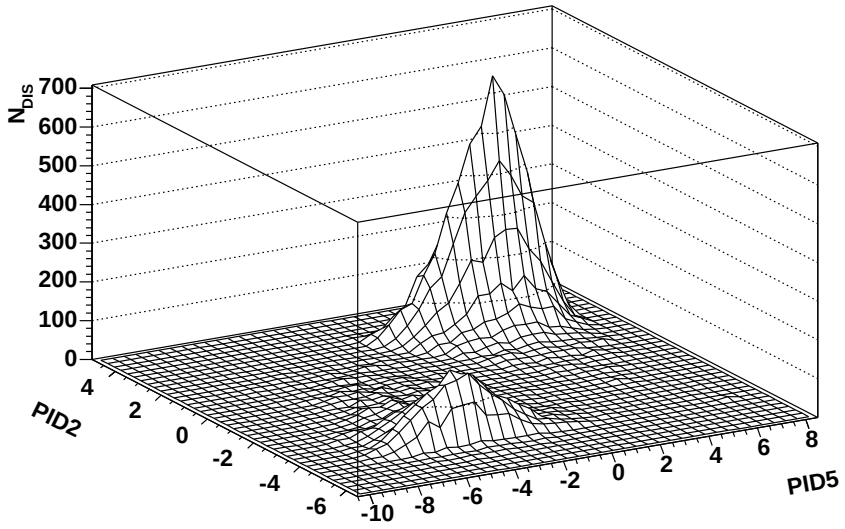

Figure 3.5: Distribution of DIS events versus the PID2 and PID5 values, based on unpolarized neon data.

responses of the PID detectors, denoted by R, the quantity PID is then calculated as

$$PID = log_{10}\frac{P_e(p,R)}{P_h(p,R)}$$

whereby the probability distribution that an electron (hadron) of momentum p caused a response R, is presented by $P_e(p,R)$ ($P_h(p,R)$). A large positive PID value means that the track was very likely an electron, and a large negative value indicates a hadron. For the case PID = 0, the probability for both is the same. At HERMES the following combinations of PID values are commonly defined,

$$PID2 \equiv PID_{cal} + PID_{pre} \quad (3.1)$$

$$PID3 \equiv PID_{cal} + PID_{pre} + PID_{cer} \quad (3.2)$$

$$PID5 \equiv PID_{trd} \quad (3.3)$$

The DIS-event distribution in simultaneous dependence of PID2 and PID5 is presented in figure 3.5. For this analysis the condition $PID2 + PID5 \geq 2$ is used, indicating that only those tracks are selected which were at least 10 times more likely to be a positron than a hadron. The distribution for the sum of PID2 and PID5 is shown in figure 3.6.

In fact, only the preshower-detector (hodoscope H2) and the calorimeter are able to detect photons and have therefore a particular importance for this analysis. The preshower detector in each spectrometer half consists of 42 vertical 1 cm thick scintillator paddles.

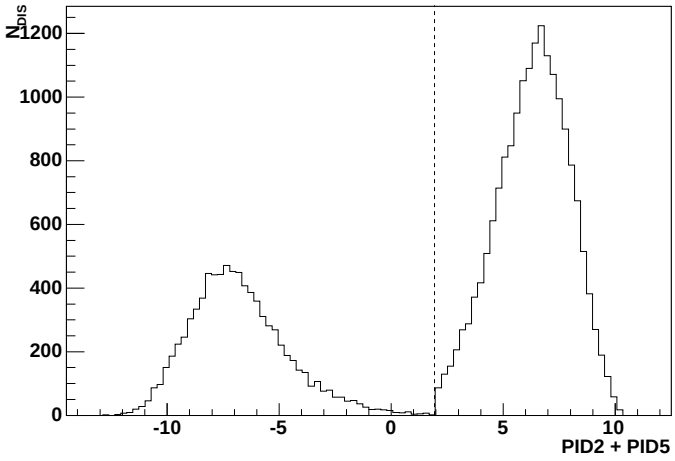

Figure 3.6: Distribution of DIS events versus the sum PID2+PID5, based on unpolarized neon data.

Each scintillator is optically combined with a photomultiplier at the outside of the detector. In front of the scintillators a lead shield with a thickness of 11 mm causes the majority of particles to produce electromagnetic showers. The lepton-hadron separation uses the fact that the probability for producing electromagnetic showers is considerably larger for leptons than for hadrons. Hence leptons deposit more energy in the scintillators and are thus energy distinguishable from hadrons.

In contrast to the preshower detector, the electromagnetic calorimeter is capable to provide a measurement of the energy and the position of the photon. The calorimeter consists of 840 radiation-resistant lead-glass blocks, divided in two parts, above and below the beam pipe, as indicated in figure 3.7. Each block is viewed from the rear by a photomultiplier tube. The blocks have an area of 9×9 cm^2 and a length of 50 cm. In order to prevent the lead-glass blocks to suffer from radiation damage, both calorimeter walls can be moved away vertically from the beam pipe for beam injection. The hit position of the photons has to be determined from the energy distribution inside a cluster, which refers to a 3×3 array of lead glass blocks. Note that the energy sum in a cluster is almost independent of the hit position.

3.3.3 The Trigger System

The Trigger System selects events that are potentially interesting for physics analysis. At HERMES, different trigger schemes are implemented, which select Deeply-Inelastic Scattering (DIS) events and photoproduction processes (without detection of the scat-

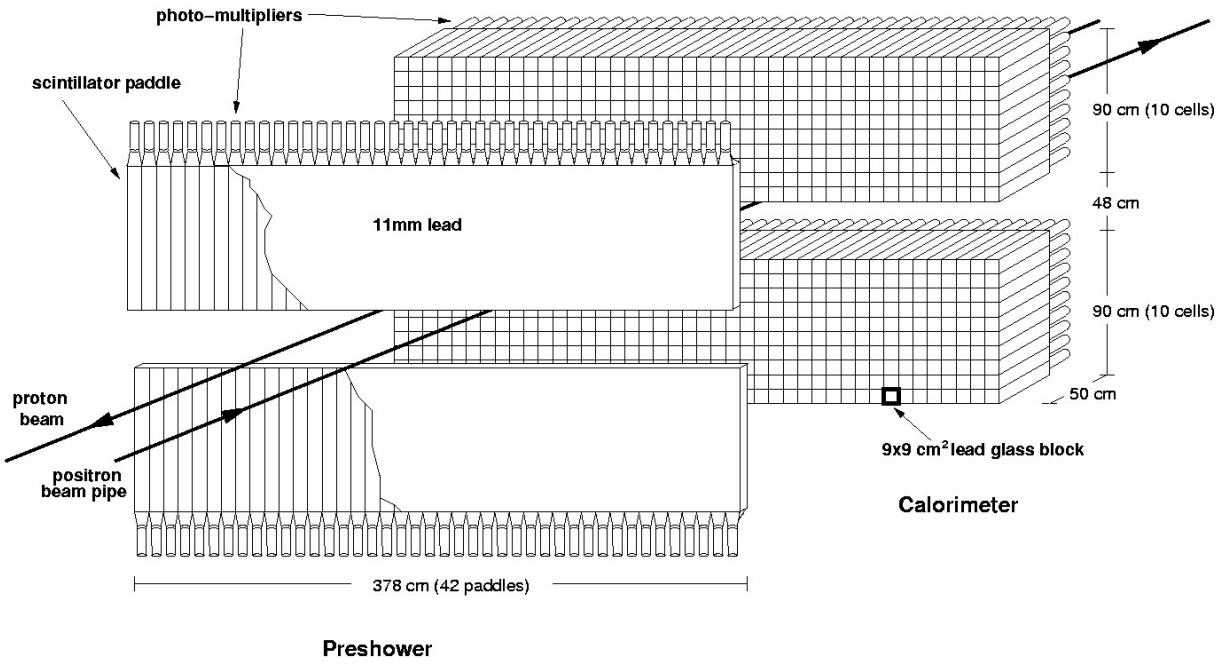

Figure 3.7: Schematic view of the preshower detector and the calorimeter.

tered lepton). There exist additional triggers for detector monitoring and calibration. The main physics trigger is trigger-21 for the DIS events, requiring hits in the three scintillator hodoscopes and a signal from the calorimeter corresponding to a deposition of at least 1.4 GeV in two adjacent calorimeter rows in coincidence with the HERA bunch signal (HERA *clock*). The data used in this analysis was collected with a threshold of 3.5 GeV in the calorimeter, corresponding to the fact that two thirds of the trigger had tracks, where 95% of reconstructed tracks came from the target, and one third had accompanying leptons.

3.4 Data Acquisition

3.4.1 Data Taking

At HERMES exists three modes of data taking. The most common mode is standard polarized-target data-taking where the luminosity is limited by the attainable target densities. To collect data from unpolarized targets there are two ways. Unpolarized-target data can be collected either by using target densities that are limited by the

beam lifetime, or alternatively in high-density running, which is done regularly at the end of each fill when the collider experiments have switched off. Under these conditions the luminosity is limited by the trigger rates or the dead time. For this analysis only unpolarized-target data exists for the neon gas target, from which 97% of the data was accumulated in high density runs.

3.4.2 Data Acquisition and Structure

The backbone of the data acquisition system is constructed in Fastbus. It consists of 10 front-end crates, the event collector crate, and the event receiver crate connected to the online workstation cluster, whereby the CERN Host Interfaces (CHI) act as Fastbus master. Their readout performance is enhanced in most places with Struck Fastbus Readout Engines (FRE).

HERMES data sets are divided into fills, runs and bursts. A fill is the time period in which the HERA lepton ring accelerates and stores the same fill of leptons until the lepton beam is dumped. The usual fill time is 8-14 hours. Data is taken after a trigger occurs during the measurement. Then the acquisition system translates the responses from all detectors into a digital form and stores it in a file on a hard disk. A run is determined by a file size of approximately 450 MB, corresponding to 10-30 min data taking. In addition, all data not associated to a single event but to the hardware, target and beam performance is stored in the slow-control data. The slow-control refers to the reading and recording of hardware information that changes on a slow time scale, which is read out every 10 sec. This chosen time period defines a burst.

The run-file is written in the Experimental Physics Input Output (EPIO) format on a hard disc and copied to the DESY tape robot. After that, several programs convert this raw data into useful physics quantities:

- At first the HERMES DECoder (HDC) decodes the EPIO files by using the knowledge of the design of the subdetectors. The output file is stored in a tabular structure of the Aleph DAta MOdel (ADAMO). Before writing a program, the tables are defined using a specific Data Definition Language (DDL).
- The ADAMO database is sent to the HERMES ReConstruction (HRC) program. This program combines individual detector responses with alignment and calibration information, in order to reconstruct the trajectories in the spectrometer.
- After that, the HRC output and the slow-control data are combined into a single file for every run. The output is written as a micro-Data Summary Tape file (μDST), which is then normally used for the physics analysis.

4 Data Analysis

In order to get access to the Beam Spin Asymmetry (BSA), discussed in section 2.4, several data analysis steps have to be performed. An exclusive event has to fulfill specific conditions to be considered as a DVCS-BH event. In a first step only analyzable data are selected. In a second step events within certain kinematic boundaries according to a DIS event are accepted. After that, only those DIS events are selected that have exactly one charged track (the scattered positron), and one photon within certain constraints. These events are called single-photon events. Since the HERMES spectrometer can not detect the recoiling nucleon, the missing mass is calculated by using the kinematics of the scattered positron and the real photon. In order to ensure exclusivity, only single-photon events are selected which fulfill a certain missing mass constraint. In the last step the selected exclusive event sample has to be separated in a coherent and incoherent part. The several steps of event selections and the according data treatment are discussed in the following sections.

4.1 Event Selection

4.1.1 Data Sample

The data for this analysis were accumulated during the 2000 running period of HERA using a polarized positron beam with an average polarization of 54%. The beam polarization in both helicity states was approximately the same, for parallel polarization 52% and for antiparallel polarization 55%. The positrons were scattered off an unpolarized neon gas target. The measurements are based on an integrated luminosity of about 82 pb^{-1}. The μDST-production 00d0 is used which amounts to 845 runs.

4.1.2 Data Quality

In order to select data with sufficient quality for the physics analysis two different lists have to be checked. The first quality check is done on the run level. Only runs are taken into account that are marked with the following criteria in the electronic logbook:

- The target was normal or high density neon.
- The run was marked as analyzable.

The second quality check is based on the slow-control data, written for every burst. For that the burstlist-file with the condition *badbit*&0x503E13DC is used, containing the following data-quality cuts:

- The run is marked as analyzable in the logrun file.
- There are no HV trips in the tracking chamber.
- There are no dead blocks in the calorimeter or luminosity monitor.
- The preshower detector is working correctly.
- The TRD is fine during the burst.
- The DAQ live time is greater than 0.8.
- The burst is not the first one in a run.
- The beam current is reasonable (5 mA $<$ I $<$ 50 mA).

Three additional cuts are applied:

- The live time for trigger 21 is between 0.8 and 1
- The raw luminosity is between 5 and 3000.
- The fitted beam polarization is between 30% and 80%.

4.1.3 DIS Event Selection

The DIS event selection is based on several detector acceptance cuts and kinematic constraints for positrons. In addition the number of the recorded DIS events is important for normalization purposes. The following cuts for identifying a DIS event are required:

- The combined response from preshower and calorimeter ($PID2$) and the response of the TRD ($PID5$) satisfy the requirement $PID2 + PID5 > 2$. This corresponds to a 10^2 times larger probability, that the track is a lepton and not a hadron.
- Each event contains exactly one positron.
- Each event is triggered by trigger 21.

- The track passes the fiducial volume cuts.
- The track traverses the full length of the spectrometer.
- The distance of closest approach of the track to the beam should be in the longitudinal direction -18 $< z_{vtx} <$ 18 cm and in the transverse direction $|t_{vtx}| < 0.75$ cm.
- The (x, y) position of the lepton in the calorimeter has to obey $|x^l_{calo}| < 175$ cm and $30 < |y^l_{calo}| < 108$ cm. This corresponds to the track not being incident in the outermost 2/3 of the outer row or column of calorimeter blocks, in order to avoid that the energy might leak out of the sides of the calorimeter.
- The kinematical cuts on the detected lepton are:
  - The photon virtuality Q^2 should be large in order to be in the hard scattering regime. Therefore the data is constrained to $Q^2 > 1$ GeV^2.
  - The invariant mass of the virtual-photon-proton system is required to be W^2 >9GeV^2.
  - The energy of the virtual photon should be $\nu < 22$ GeV.

The distribution of DIS events for different variables is shown in figure 4.1. Note that the variables are calculated by using the proton mass for the reacting part of the neon nucleus. The fact that the distributions for both cases, proton and neon mass, are very similar, will not be further discussed here. Hence the variables in this chapter are all calculated on the basis of the proton mass. A comparison between the two methods of using proton or neon mass is discussed in more detail in section 5.3.

4.1.4 Single-photon Selection

Since the single photon event is characterized by only one DIS lepton and one photon in a certain kinematic range, the following cuts are required:

- Only DIS events with exactly one charged track are taken.
- The photon requires exactly one cluster in the calorimeter with no track assigned to it.
- A signal in the preshower detector with $E_{presh} > 0.001$ GeV.
- The photon energy in the calorimeter is $E_\gamma > 5$ GeV.
- The fiducial volume of the calorimeter for photons is given by $|x^p_{calo}| < 125$ cm and $33 < |y^p_{calo}| < 105$ cm.

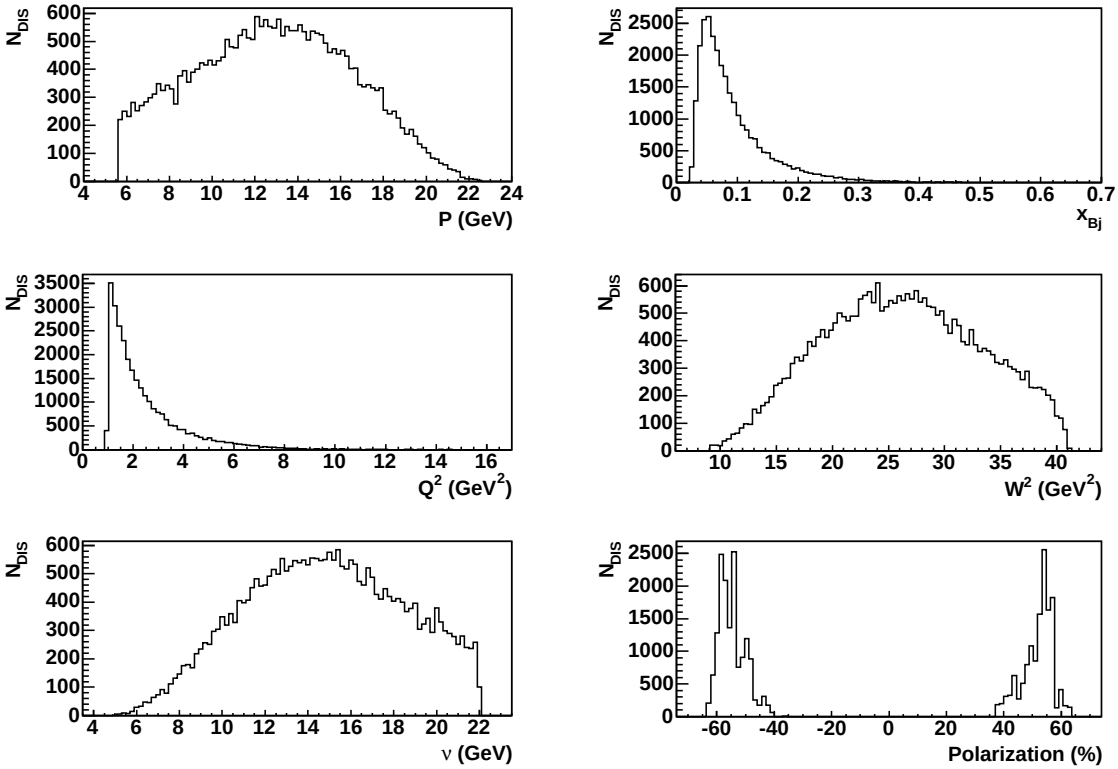

Figure 4.1: Distribution of DIS events scattered off a neon target in dependence on different kinematical variables.

- The angle between virtual and real photon, $\theta_{\gamma^*\gamma}$, has to be between 3 and 45 mrad.

The distributions of single-photon events are presented in figure 4.2 for different kinematic variables.

4.1.5 Exclusive Event Selection

The selection of exclusive events has to be based on a missing mass calculation, since there is no possibility to detect the recoiling nucleon with the present HERMES detector. The missing mass squared M_x^2 is given as

$$M_x^2 = (q + p - q')^2 \tag{4.1}$$

with the four momenta of the virtual photon q, of the target nucleon (nucleus) p and the real photon q'. Since the energy resolution of the HERMES spectrometer is not perfect,

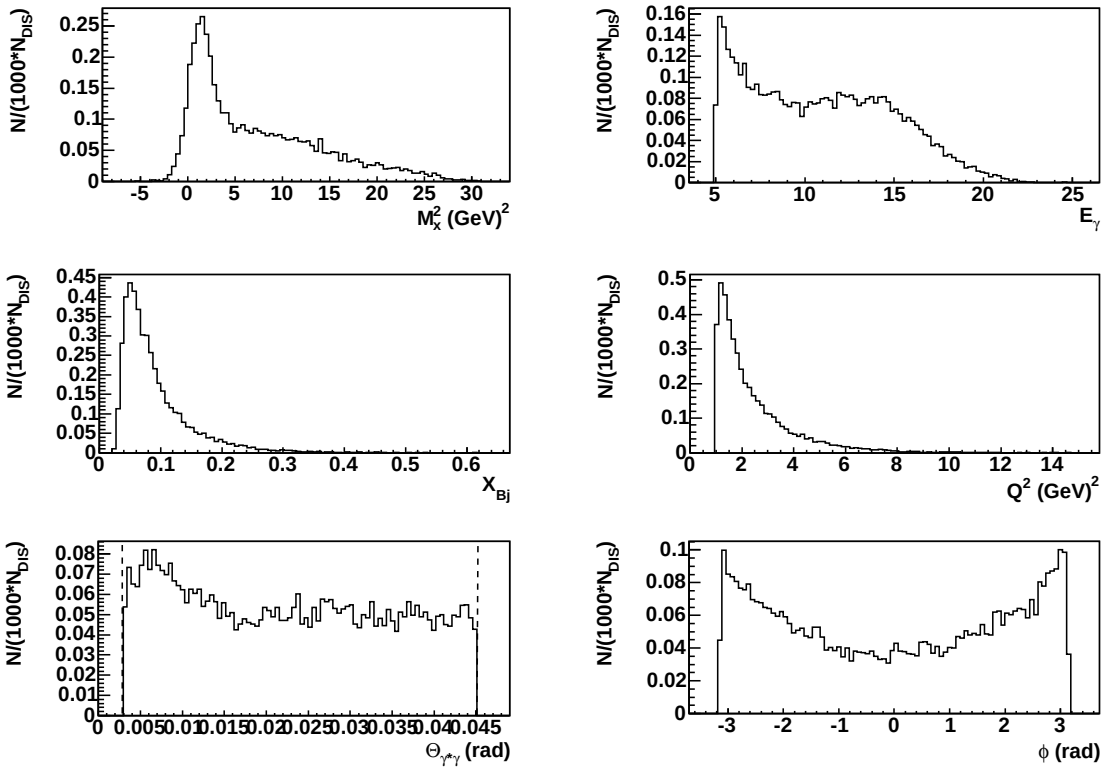

Figure 4.2: Distributions of the single-photon event yields in dependence on different kinematic variables, normalized per 1000 DIS events.

events can be reconstructed with negative values of M_x^2. The M_x^2-distribution for neon is shown in figure 4.3. The exclusive peak for this distribution is smeared out (negative values for M_x are defined as $M_x = -\sqrt{-M_x^2}$).

In order to ensure exclusive events, the missing mass constraint -1.5 GeV $< M_x <$ 1.7 GeV is used, as indicated by the two lines in figure 4.3. This specific missing mass interval is found by optimizing the signal-to-background ratio using semi-inclusive background [Ell].

In fact, the missing mass distribution is not the only kinematic distribution which shows an *unphysical* extension to negative values. Also the $-t$ distribution is smeared, caused by the energy resolution of the calorimeter. Since the extraction of the BSA as a function of $-t$ is important for theoretical predictions, the following *reconstruction* of $-t$ is performed [Ell]. The variable M_x and $-t$ are related to each other via

$$M_x^2 = M_p^2 + 2M_p(\nu - E_\gamma) + t. \tag{4.2}$$

By assuming that the missing mass squared is equal to the proton mass $M_x = M_p$, it

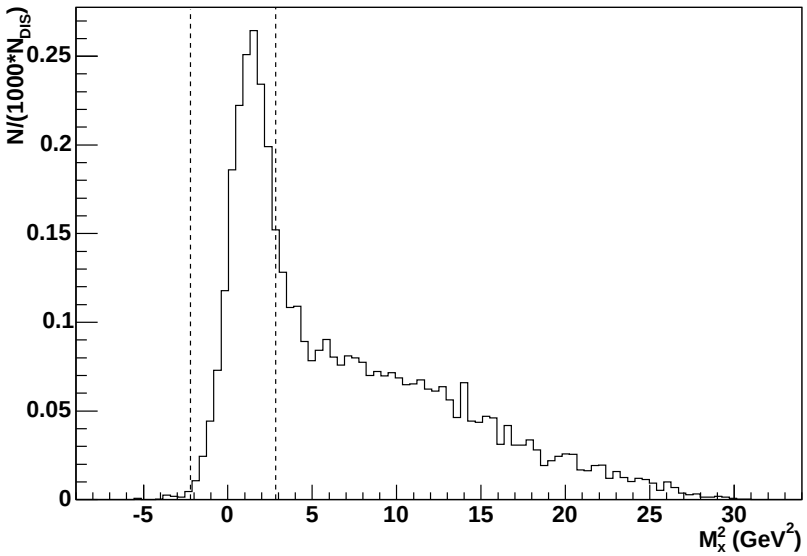

Figure 4.3: Distribution of single photon events versus the missing mass squared M_x^2.

is possible to calculate $-t$ without the knowledge of the photon energy E_γ. Hence the photon energy E_γ is calculable via

$$E_\gamma = \frac{t}{2M_p} + \nu \tag{4.3}$$

The calculation of the four-momentum transfer squared is given as

$$t = (q - q')^2 = -Q^2 - 2E_\gamma(\nu - \sqrt{\nu^2 + Q^2}\, cos\theta_{\gamma^*\gamma}) \tag{4.4}$$

By inserting equation 4.3 in equation 4.4, the momentum transfer squared can be calculated without any dependence on E_γ via

$$t_c = \frac{-Q^2 - 2\nu(\nu - \sqrt{\nu^2 + Q^2} cos\theta_{\gamma^*\gamma})}{1 + \frac{1}{M_p}(\nu - \sqrt{\nu^2 + Q^2} cos\theta_{\gamma^*\gamma})}. \tag{4.5}$$

The result is called the constrained momentum transfer t_c. The effect of this calculation is shown in figure 4.4, comparing the momentum transfer $-t$ to the constrained momentum transfer $-t_c$. Note that this method is completely correct for the important "3-particle final states" ($e\ p\ \gamma$), while it is not exactly correct for the (less important) background events (π^0, η, K^0). Summarizing, the exclusive sample is constrained by the following kinematic boundaries:

$$\begin{array}{lcccl} 0.03 & < & x_{Bj} & < & 0.35 \\ 2.25\ \text{GeV}^2 & < & M_x^2 & < & 2.89\ \text{GeV}^2 \\ & & -t_c & < & 0.7\ \text{GeV}^2 \end{array}$$

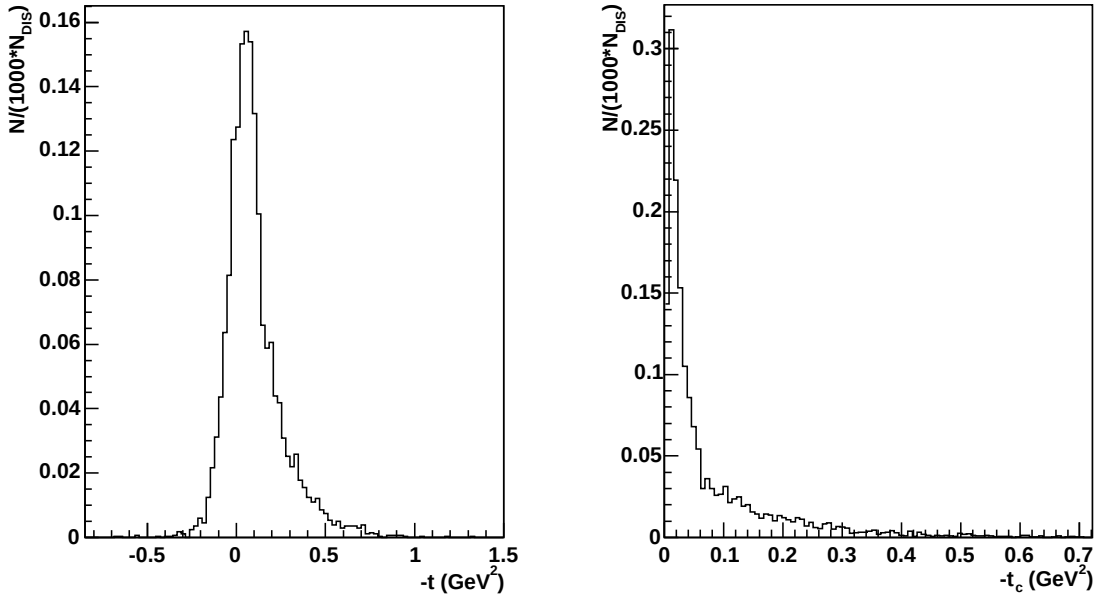

Figure 4.4: Comparison between the momentum transfer $-t$ and the constrained momentum transfer $-t_c$. Both distributions are for the exclusive sample, normalized per 1000 DIS events.

The kinematic distributions of exclusive events are shown in figure 4.5 for different variables.

4.2 Extraction of the Beam-Spin Asymmetry

The azimuthal dependence of the BSA can be extracted by fitting the cross-section asymmetry as a function of the azimuthal angle ϕ. The beam spin asymmetry A_{LU} is defined as

$$A_{LU}(\phi) = \frac{d\overrightarrow{\sigma} - d\overleftarrow{\sigma}}{d\overrightarrow{\sigma} + d\overleftarrow{\sigma}} = \frac{\int_0^{2\phi} d\phi \left(\frac{d\overrightarrow{\sigma}}{d\phi} - \frac{d\overleftarrow{\sigma}}{d\phi}\right)}{\int_0^{2\phi} d\phi \left(\frac{d\overrightarrow{\sigma}}{d\phi} + \frac{d\overleftarrow{\sigma}}{d\phi}\right)}, \tag{4.6}$$

where L denotes the longitudinal polarized beam and U the unpolarized target. In order to extract the beam spin asymmetry A_{LU} from the data, the cross-section ratio is calculated for every ϕ-bin by counting the respective exclusive events. A_{LU} is then

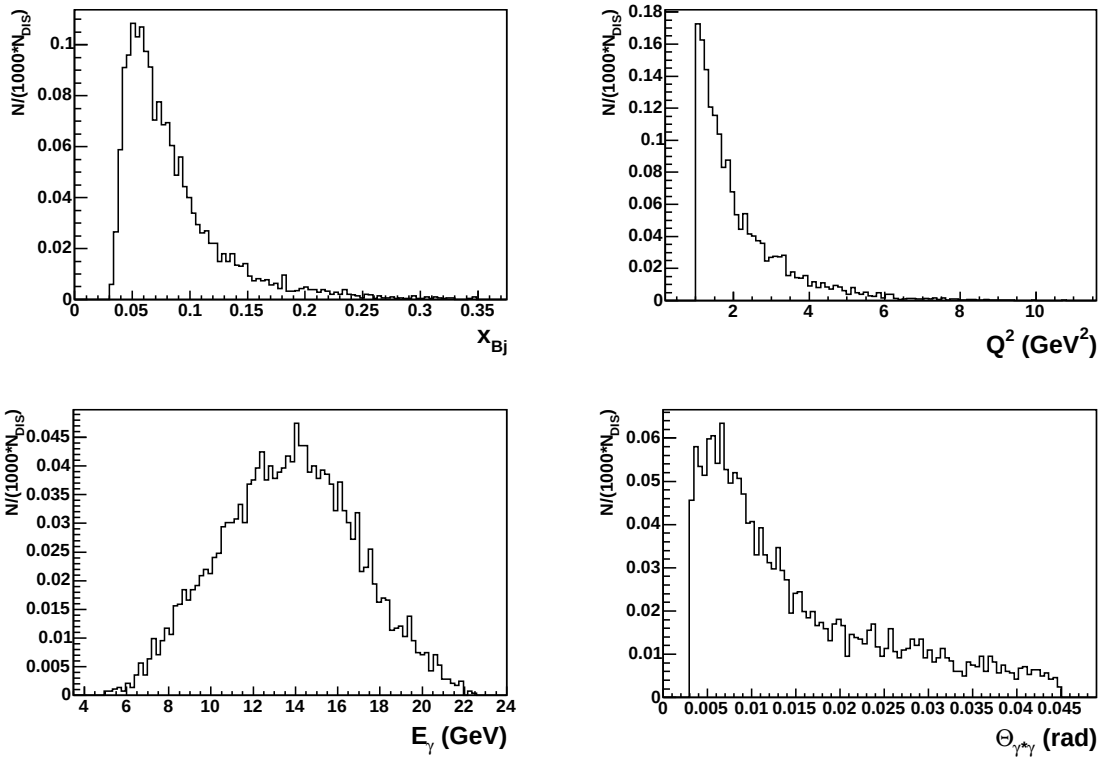

Figure 4.5: Kinematic distributions of exclusive events with normalization per 1000 DIS events

given as

$$A_{LU}(\phi) = \frac{1}{\langle P \rangle} \frac{\frac{\overrightarrow{N}(\phi)}{\overrightarrow{Norm}} - \frac{\overleftarrow{N}(\phi)}{\overleftarrow{Norm}}}{\frac{\overrightarrow{N}(\phi)}{\overrightarrow{Norm}} + \frac{\overleftarrow{N}(\phi)}{\overleftarrow{Norm}}} \tag{4.7}$$

with $\overrightarrow{N}$ ($\overleftarrow{N}$) representing the exclusive yield in the helicity state parallel (antiparallel) to the beam direction. The average beam polarization $\langle P \rangle$ for the neon data in 2000 was 54%. For normalization, denoted by $\overrightarrow{Norm}$ and $\overleftarrow{Norm}$,the numbers of DIS events in each helicity state were used. Another possibility for a normalization is based on the luminosity, calculated as the product of the rate measured in the luminosity monitor, the live time of trigger 21 and of the burst length. Both methods for normalization are compared in section 5.4. for the neon data.

The beam spin asymmetries on neon for each ϕ-bin are plotted in figure 4.6 with the respective statistical error bars. The harmonics $\sin\phi$ and $\sin 2\phi$ of the BSA are obtained by fitting the asymmetries over ϕ. As already discussed in section 2.4. the $\sin\phi$ amplitude, denoted by $A_{LU}^{\sin\phi}$, is correlated to the amplitude of the BH-DVCS-interference

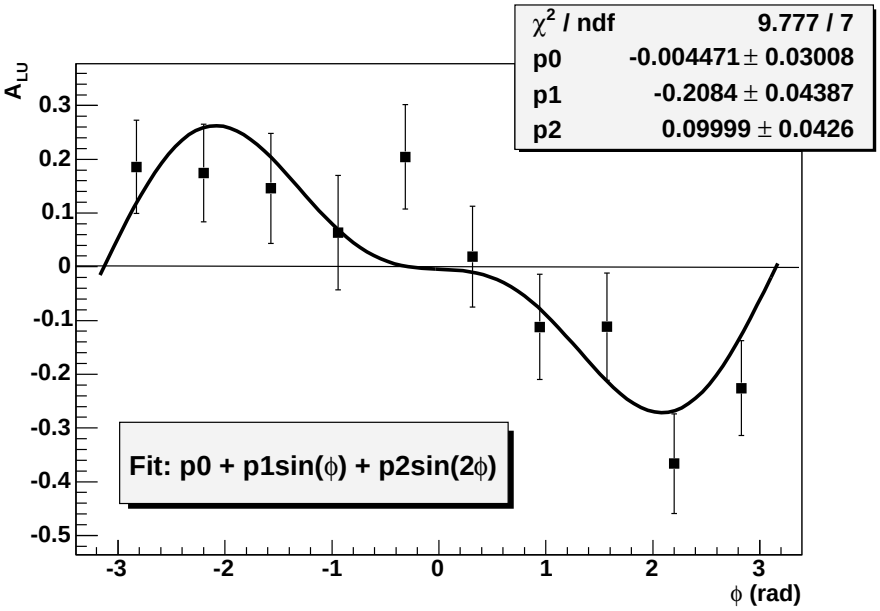

Figure 4.6: The calculated beam-spin asymmetry A_{LU} on neon for each ϕ-bin with the respective statictical error bars. The fit-function is given as $p_0 + p_1 \sin\phi + p_2 \sin 2\phi$.

term. Therefore the asymmetry fit for the BSA is usually done with the fit function

$$f(\phi) = p_0 + p_1 \sin\phi + p_2 \sin 2\phi. \tag{4.8}$$

Other fit functions are discussed in section 5.5. The $\sin 2\phi$ term is allowed to appear, due to higher order in α_s, as explained in section 2.4. A possible constant term p_0 can only arise from a helicity-dependent, but ϕ-independent term in the cross-sections. The constant term p_0 is studied in section 5.10.

The calculation of the statistical error for A_{LU} is based on the Poisson distribution:

$$dA_{LU}^{stat} = \frac{2}{\langle P \rangle} \sqrt{\overrightarrow{N} * \overleftarrow{N} * (\overrightarrow{N} + \overleftarrow{N})} \frac{\overrightarrow{Norm} * \overleftarrow{Norm}}{(\overrightarrow{N} * \overleftarrow{Norm} + \overrightarrow{N} * \overleftarrow{Norm})^2}. \tag{4.9}$$

Note that the Poisson distribution becomes a Gaussian distribution for higher values of N.

In figure 4.7 the amplitude of the $\sin\phi$ harmonic, $A_{LU}^{\sin\phi}$, is plotted vs. missing mass M_x for neon. The upper cut on t_c and the upper cut on $\theta_{\gamma^*\gamma}$ have been removed here in order to reduce the error bars in the non-exclusive region. The asymmetry is largest for the first two bins in M_x where the contribution of the background processes is smallest. The third bin shows a slightly smaller asymmetry since background contributions start to dilute the asymmetry. The fourth bin yields a mixture of the exclusive and the

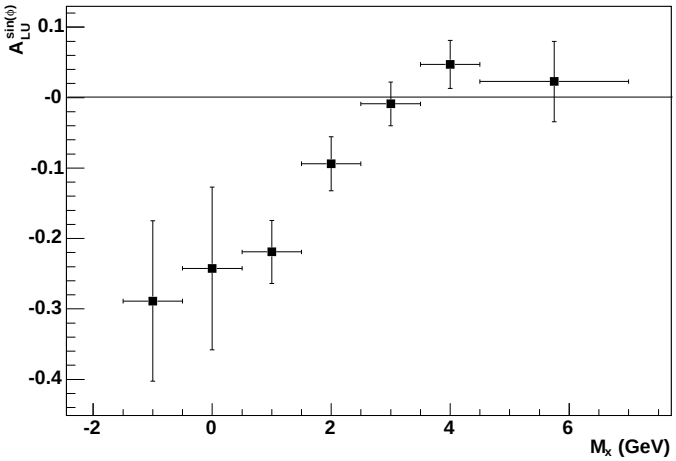

Figure 4.7: The asymmetry amplitude $A_{LU}^{\sin\phi}$ vs. missing mass M_x for neon. The upper cut on t_c and the upper cut on $\theta_{\gamma^*\gamma}$ have been removed in order to reduce the error bars in the non-exclusive region.

non-exclusive sample and consequently shows a decreased asymmetry value. The last three bins should not yield any contribution from the BH-DVCS interference anymore and there is indeed no sign for a significant negative amplitude anymore. The slightly positive asymmetry in the non-exclusive region shows the known beam spin asymmetry for π^0 production, which is carried through the π^0 decay to the one detected photon.

4.3 Hydrogen Data

Since hydrogen data is required for the interpretation in chapter 7, the currently available hydrogen results will be presented and compared to the results obtained in the present study. In figure 4.3 the extracted asymmetry A_{LU} for hydrogen is compared between previous released results [Now05] and non-released results obtained from this analysis. Note that the $\theta_{\gamma^*\gamma}$ constraints are changed to 0.002 rad $< \theta_{\gamma^*\gamma} <$ 0.7 rad for this comparison. The only difference between both data sets is due to different productions of 2000 data: the results of [Now05] are extracted from the production 00c0, whereas the present analysis is based on the newest production 00d0. The asymmetry amplitudes are

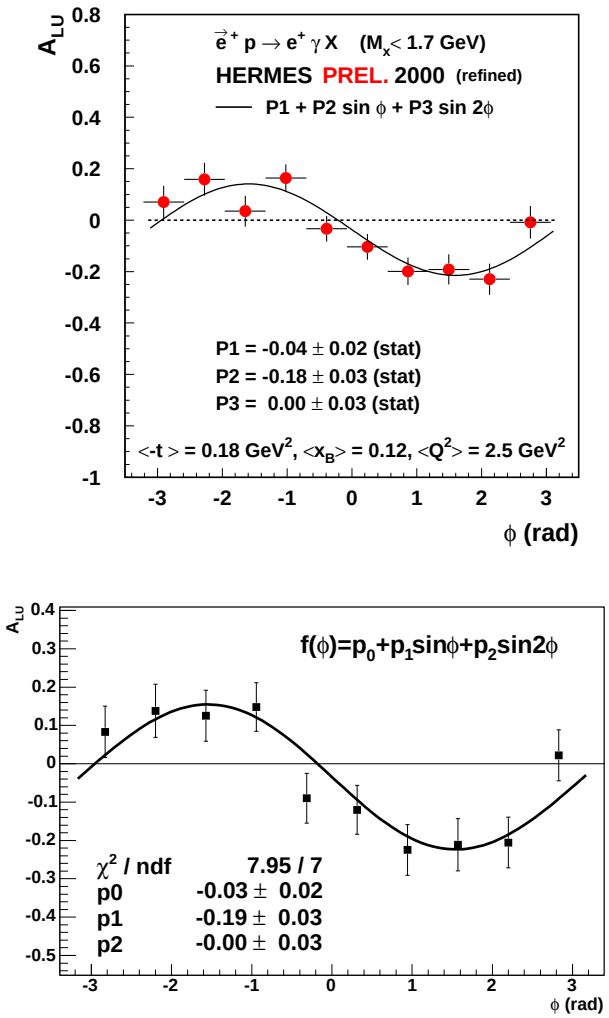

Figure 4.8: Comparison of A_{LU} for hydrogen between previous released results [Now05] and non-released results obtained from this analysis.

	Previous Study Released [Now05]	Present Study Not Released
const p_0	-0.04±0.02	-0.03±0.02
$A_{LU}^{\sin\phi}$	-0.18±0.03	-0.19±0.03
$A_{LU}^{\sin 2\phi}$	0.002±0.03	0.00±0.03,

and are found in good agreement. A comparison of $A_{LU}^{\sin\phi}$ in dependence on t_c is presented in figure 4.9. The only available t_c dependence for $A_{LU}^{\sin\phi}$ is presented in [Ell] and is

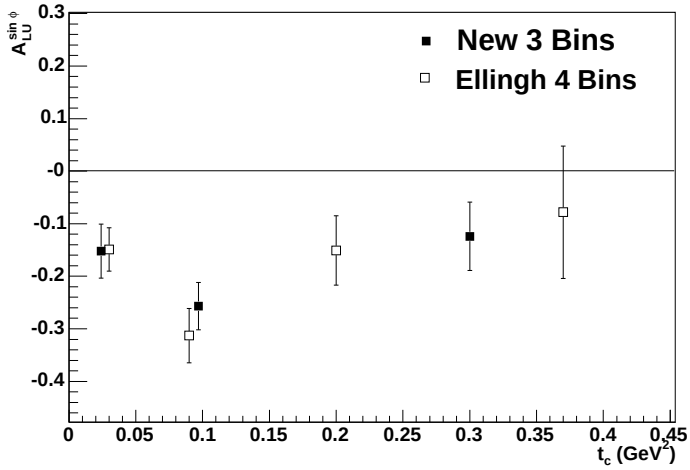

Figure 4.9: Comparison of the asymmetry amplitude $A_{LU}^{\sin\phi}$ in dependence of t_c for hydrogen between previous results [Ell] and non-released results obtained from this analysis.

taken for this comparison. Note that there exists a different t_c binning. In summary, the hydrogen results obtained in the present analysis are compatible to the released ones and therefore they will be taken for further comparison with neon in chapter 7.

4.4 Separation of Coherent and Incoherent Part

The DVCS reaction on neon proceeds through two different processes. On the one hand, there is the coherent process that involves the nucleus as a whole, on the other hand, the incoherent process as the reaction on a single nucleon. Since coherent and incoherent processes contribute to the photon production cross section, both parts have to be separated. As has been explained in section 2.5., the distribution of the momentum transfer $-t$ is a reasonable tool for a separation between coherent and incoherent part.

In figure 4.10 the t_c distribution is shown for the exclusive sample of neon. Note that the yield is on a logarithmic scale. In fact, the t_c distribution shows a different slope at low and high t_c, corresponding to coherent and incoherent part. In order to estimate the separation point p_{sep}, a double exponential function is fitted to both parts simultaneously:

$$f(\phi) = \underbrace{e^{p_0+p_1 x}}_{exp_{coh}} + \underbrace{e^{p_2+p_3 x}}_{exp_{incoh}} \tag{4.10}$$

For the calculation of the transition point x_0, both exponential functions have to be set

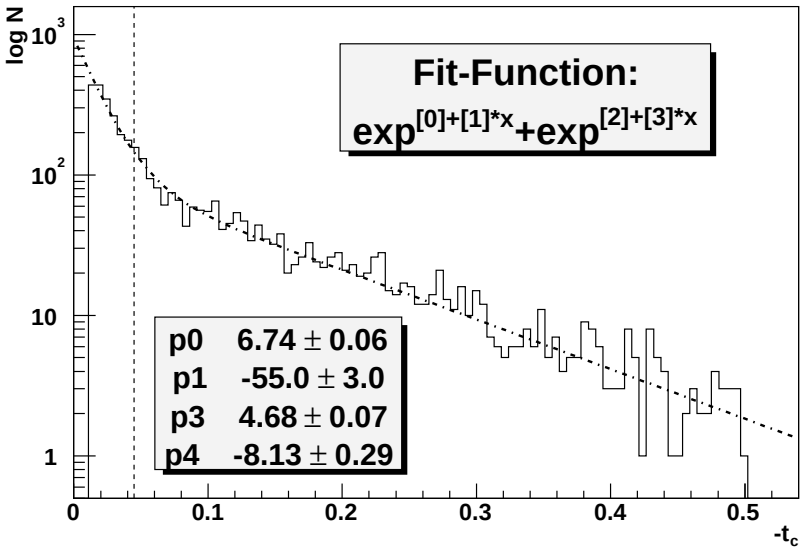

Figure 4.10: Distribution for the exclusive sample of neon. The y-axis is set logarithmically. The distribution is fitted by $e^{p_0+p_1 x} + e^{p_2+p_3 x}$, corresponding to the coherent and incoherent part. The vertical dashed line indicates the point where both exponential functions are equal.

equal

$$exp_{coh} = exp_{incoh} \tag{4.11}$$

and from that x_0 is obtained as

$$x_0 = \frac{p_0 - p_2}{p_3 - p_1} \tag{4.12}$$

By using the fit result, given in 4.10, x_0 was found to be at $t_c = 0.044 \pm 0.006$ GeV^2. A comparison of the $-t_c$ distribution between neon and proton is presented in figure 4.11. The parameter of the fit results are given as

	Neon	Hydrogen
coh. constant $p0$	6.74 ± 0.07	5.4 ± 0.2
coh. slope $p1$	-54.99 ± 2.95	-19.1 ± 3.7
incoh. constant $p2$	4.68 ± 0.07	5.6 ± 0.2
incoh. slope $p3$	-8.13 ± 0.30	-7.9 ± 0.5 ,

indicating a clear difference in the slope behavior between both processes, as expected.

Another possibility for the separation of coherent and incoherent part is offered by Monte-Carlo (MC) studies. Such studies allow in addition to estimate the contribution

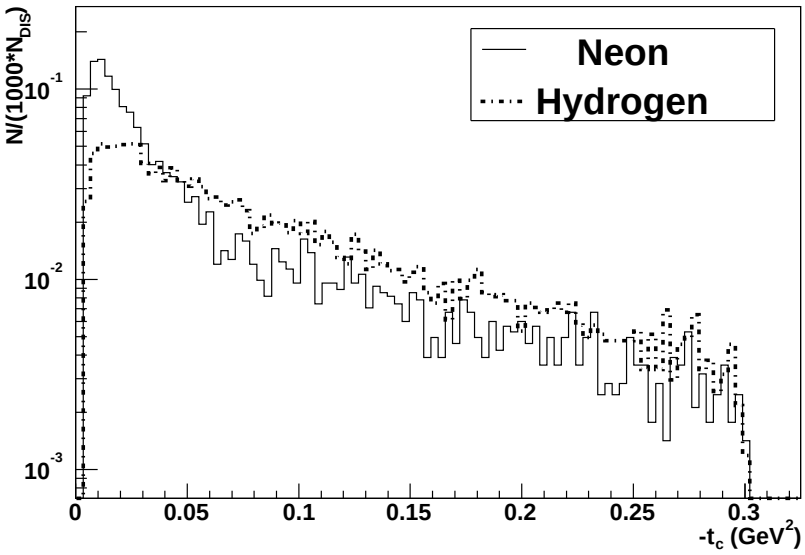

Figure 4.11: Comparison of the t_c distribution between neon and proton, normalized per 1000 N_{DIS}.

of coherent and incoherent to the full exclusive sample and will be discussed in section 5.1.2. In the following the separation point, p_{sep}, was set at $t_c = 0.045$ GeV^2. It is important to note that p_{sep} does not make a clear cut between coherent and incoherent part, because each part contaminates the other. Further studies on the influence of the separation point on the extracted BSA will be discussed in section 5.2. A comparison between coherent and incoherent part for the kinematic distributions is shown in figure 4.12. The separated BSA results for neon are presented in figure 4.13

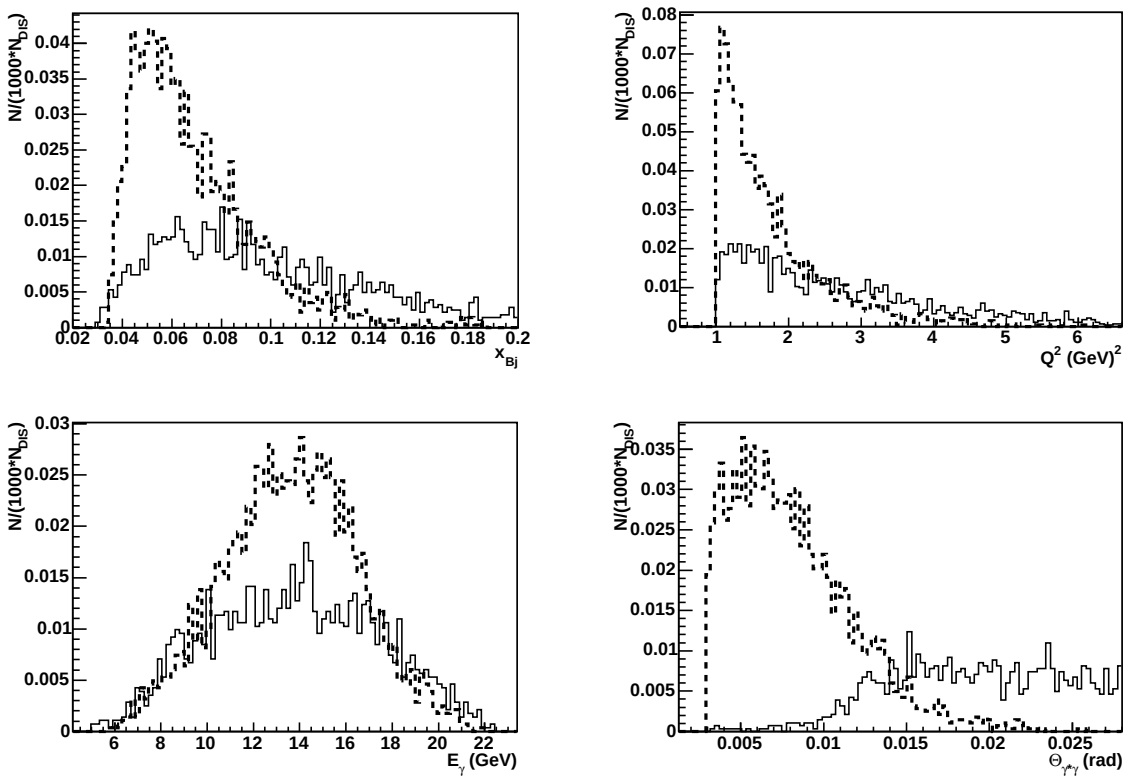

Figure 4.12: Kinematic distributions of exclusive events for coherent data (dashed) and incoherent data (solid), normalized per 1000 DIS events.

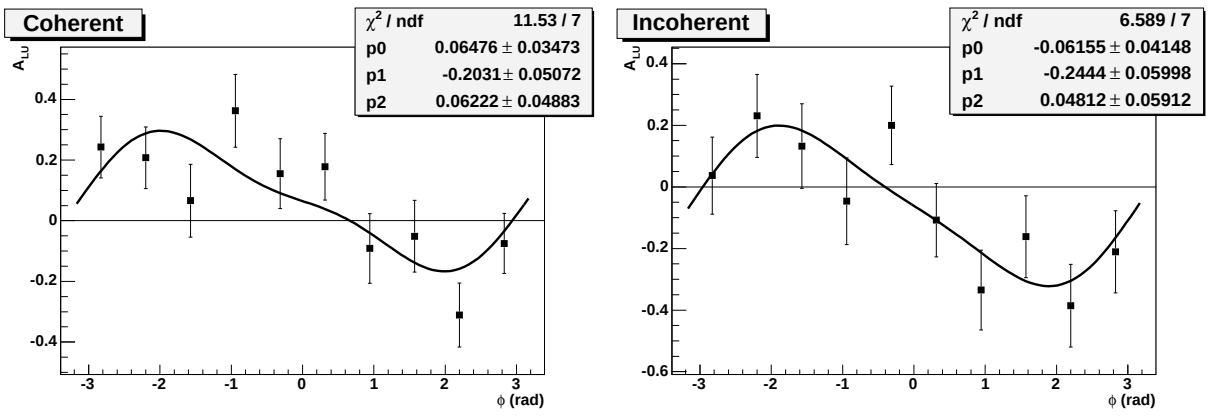

Figure 4.13: BSA for coherent (left) and incoherent part (right) on neon.

5 Systematic Studies

In order to evaluate the systematic uncertainties of the BSA results, a number of different studies were performed and are described in the following sections.

5.1 Monte Carlo Studies

5.1.1 The HERMES Monte Carlo Production

The HERMES Monte Carlo (HMC) program simulates a variety of physics processes using different programs on the event generation level. At first, a Generator Monte Carlo (GMC) program is used to generate the final state particles in each event. This information is then processed by HMC, whereby each particle is tracked through the HERMES spectrometer by the detector description code GEANT, and the response of the detector is digitized. The output of HMC is very similar to the output of the data decoder, HDC, except that it also includes all the information generated by GMC.

The Monte Carlo code is subdivided into units, called *packages*. For example, the JETSET package [Sjo94] models the fragmentation process, based on the LUND string hadronization model [AGIS83]. In order to simulate the BH process, the RADGEN [ABR98] program is used, which takes into account the lowest order radiative processes in QED for polarized and unpolarized DIS. Note that the unpolarized case can be also calculated directly using the Mo and Tsai formalism [MT69].

5.1.2 Coherent and Incoherent Contribution

In comparison to data, where no simple distinction between coherent and incoherent contribution is possible, the MC simulation offers the advantage to provide a clear separation of coherent and incoherent processes. For this study, DIS events on neon are generated via HMC and exclusive events are extracted by using the kinematic constraints discussed in section 4.1. A comparison between the exclusive MC event and data event distribution for t_c is presented in figure 5.1. Both distributions show the same t_c behavior and are found to be in good agreement.

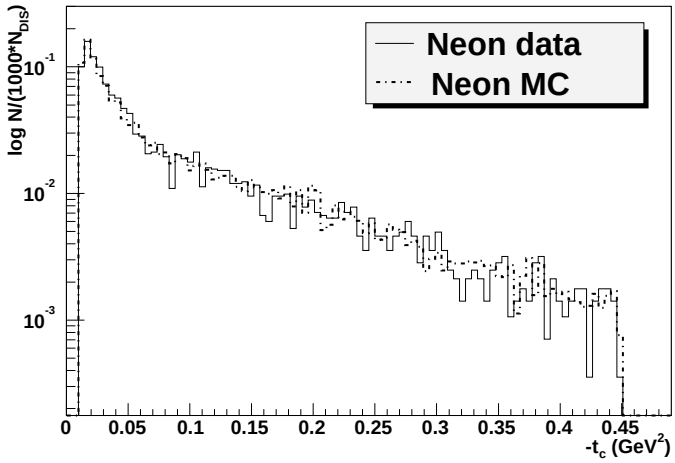

Figure 5.1: Comparison of the $-t_c$ distribution between MC (dashed line) and data (solid line) for DVCS on neon, normalized per 1000 DIS events.

In order to estimate the coherent and incoherent contributions to the full cross-section, the MC events can be clearly separated in coherent and incoherent processes. In the left panel of figure 5.2 the t_c distribution is shown for coherent, incoherent, semi-inclusive and associated BH processes. The right panel of the figure shows the fractional contribution of these processes to the full cross section. As expected, the low t_c region is dominated by coherent events, whereas the higher t_c region is dominated by incoherent events. The transition point, where both processes have about the same contribution to the full cross-section, is found to be at $-t_c = 0.045$ GeV^2. This is in good agreement to the separation point t_{sep} as calculated from data and discussed in 4.3. By setting t_{sep} at 0.045, the incoherent (coherent) admixture in the coherent (incoherent) part is calculated to be 16% (8%). Note that in the coherent (incoherent) part exists a 4% (27%) contribution from associated BH and semi-inclusive events.

5.2 The Influence of the Separation Point on the BSA

In the following study a variation of the coherent-incoherent separation point t_{sep} is performed. In figure 5.3 the BSAs $A_{LU}^{\sin\phi}$ and $A_{LU}^{\sin 2\phi}$ are shown in dependence of t_{sep}. The differences of $A_{LU}^{\sin\phi}$ in dependence on t_{sep} are found to be less then 0.02 in the region of $\pm$ 0.015 from the separation point at $-t_c = 0.045$ GeV^2 for the coherent as well as the incoherent part. In the case of $A_{LU}^{\sin 2\phi}$ the differences are less then 0.03 for the coherent and less then 0.05 for the incoherent part.

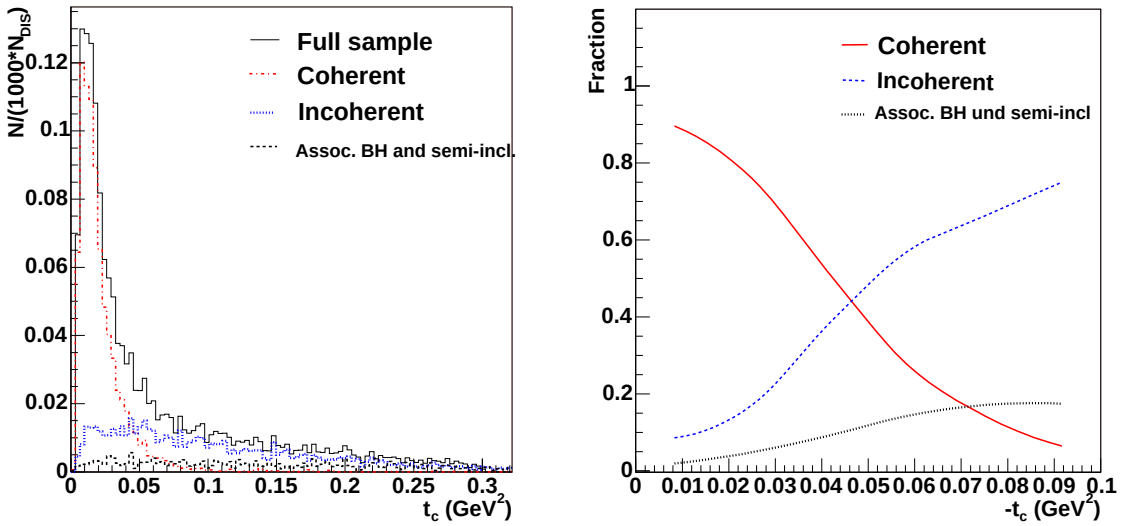

Figure 5.2: MC study of the $-t_c$ distribution, separated in coherent, incoherent, semi-inclusive and associated BH processes (left panel). The right panel shows the fractional contribution to the full cross-section.

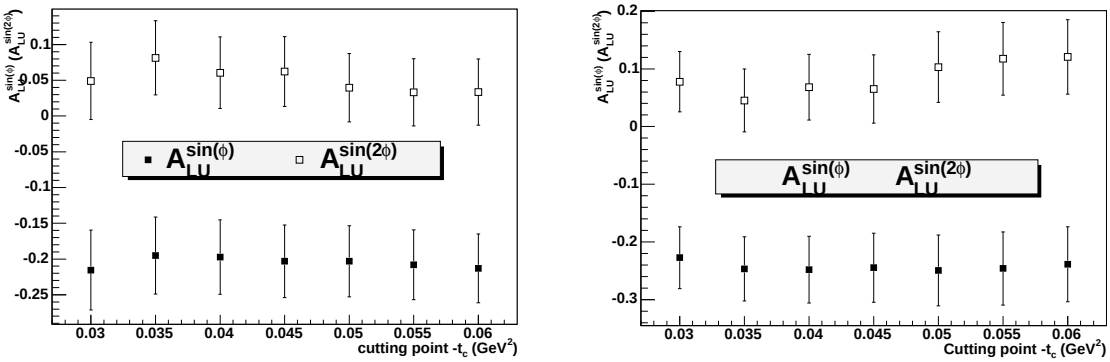

Figure 5.3: The BSA results $A_{LU}^{\sin\phi}$ and $A_{LU}^{\sin 2\phi}$ in dependence of different separation points t_{sep} for coherent (left) and incoherent part (right).

In order to avoid a sharp cut in t_c, the asymmetries can also be calculated by *weighting* the corresponding events. The *weighting* depends on the fraction of the coherent or incoherent contribution to the full cross-section, shown in the right figure 5.2. The result of the asymmetries, extracted by *weighting*, is given for the coherent data as

$$\begin{aligned} A_{LU}^{\sin\phi} &= -0.206 \pm 0.057 \ (t_{sep} = -0.045 : -0.203 \pm 0.051) \\ A_{LU}^{\sin 2\phi} &= 0.057 \pm 0.055 \ (t_{sep} = -0.045 : 0.062 \pm 0.049), \end{aligned}$$

shown in comparison to the results calculated by a sharp cut t_{sep}. Note that the sample is still constrained at $-t_c < 0.07$, because the contribution of semi-inclusive and associated BH overwhelm the coherent contribution beyond this point. In comparison to the separation point method, which uses $t_{sep} = 0.045$, the differences are very small. Hence the separation point method is correct and will be used in the further analysis.

5.3 Comparison of the Calculation Method with Proton and Neon Mass

The calculation of the kinematic variables can be done either by using the proton mass (0.938 GeV) or the neon mass (18.79 GeV for Ne-20). This calculation must in principle be done in accordance with the actual process, which could be either coherent or incoherent. As the coherent process describes a reaction on the nucleus as a whole and the incoherent process is characterized by a reaction on a single nucleon, the corresponding masses should be the neon or the proton/neutron mass. It is important to note that this systematic study refers only to the mass definition and not to a comparison between proton and neon data.

The calculation based on the neon mass changes some of the kinematic values, hence several kinematical cuts have to be adapted:

- Invariant mass of the system of virtual photon and proton: $W^2 > 520$ GeV^2.
- Bjorken variable: $0.016 < x_{Bj} < 0.0186$
- The missing mass cut M_x is changed to $289 < M_x < 397$, derived from a comparison of the M_x distribution for both calculation methods. The comparison between the neon mass and proton mass calculation for the M_x distribution is shown in figure 5.4. Note that the distribution calculated with the neon mass is scaled to that with the proton mass as

$$M_x^{Proton} = \frac{M_x^{Neon}}{21} - 16, \tag{5.1}$$

  from where the changed boundaries in M_x were calculated.

A possible effect on the t_c distribution by the chosen mass can not be seen from figure 5.4. Concerning to the BSA results, the differences are negligible, presented in the following table for the coherent part:

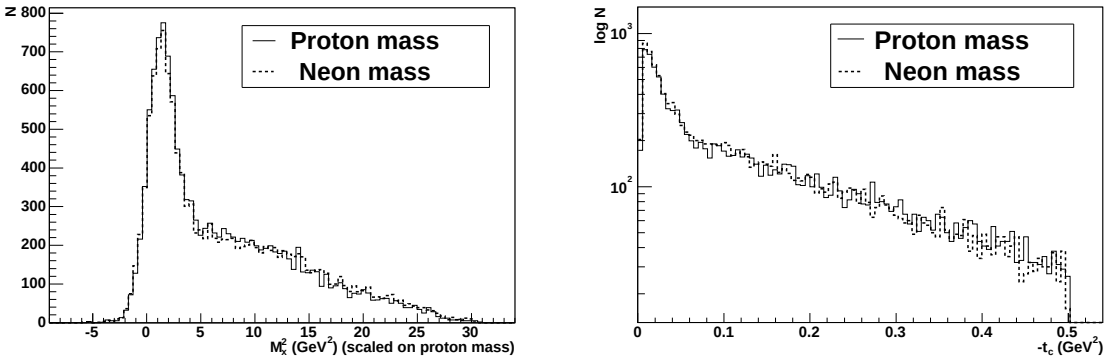

Figure 5.4: Comparison of M_x distribution (left) and t_c distribution (right) when calculated based on neon mass or proton mass, respectively. Note that the M_x distribution calculated with the neon mass is scaled to that with the proton mass.

	Proton mass	Neon mass
const p_0	0.065±0.035	0.055±0.034
$A_{LU}^{\sin\phi}$	-0.203±0.051	-0.20±0.05
$A_{LU}^{\sin 2\phi}$	0.062±0.049	0.042±0.048

In order to avoid possible mismatches, the calculation with the proton mass is applied both for the coherent and the incoherent part in this analysis.

5.4 Normalization method

The asymmetry, given as

$$A_{LU}(\phi) = \frac{1}{< P >} \frac{\frac{\overrightarrow{N}(\phi)}{\overrightarrow{Norm}} - \frac{\overleftarrow{N}(\phi)}{\overleftarrow{Norm}}}{\frac{\overrightarrow{N}(\phi)}{\overrightarrow{Norm}} + \frac{\overleftarrow{N}(\phi)}{\overleftarrow{Norm}}},$$

has to be normalized for different helicity states to the factors $\overrightarrow{Norm}$ and $\overleftarrow{Norm}$. The normalization can be done either by the corresponding number of DIS events or by the measured luminosity. Since the normalization could effect a constant-term p_0 in the asymmetry, it is useful to check the normalization on consistency. In the following, both methods are compared.

The normalization per number of DIS events is the standard method and was applied in the previous sections (e.g. figure 4.13). The kinematic boundaries and acceptance cuts for the DIS event selection were given in 3.1.2. In order to apply the luminosity method,

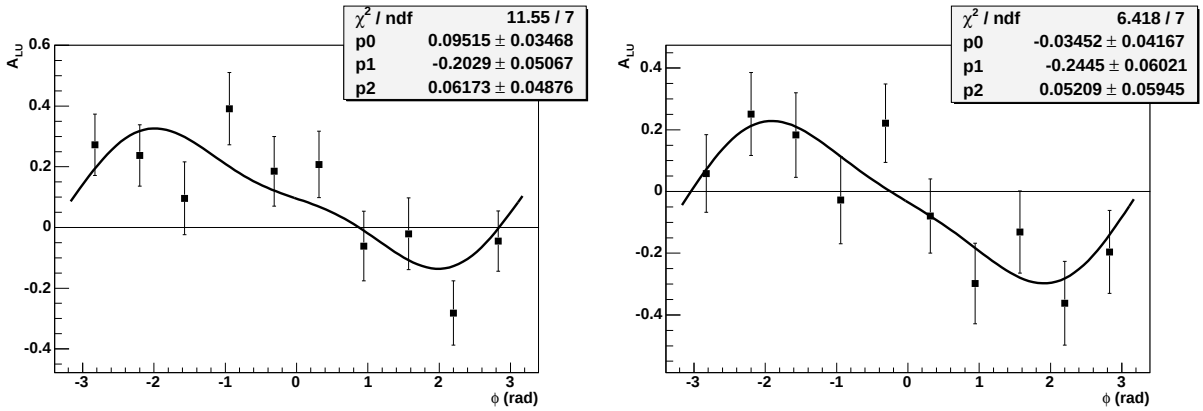

Figure 5.5: The BSA for neon, performed by using the luminosity method, for the coherent (left) and incoherent (right) part.

the product of the rate in the luminosity monitor, the live time of trigger 21 and of the burst length has to be calculated. The BSA extracted by using the luminosity method instead is shown in figure 5.5 for the coherent and incoherent part.

A comparison between both normalization methods is given in the following table:

		Norm per DIS	Norm per Lumi
Coherent	const p_0	0.065±0.035	0.095±0.035
	$A_{LU}^{\sin\phi}$	-0.203±0.051	-0.203±0.051
	$A_{LU}^{\sin 2\phi}$	0.062±0.049	0.062±0.049
Incoherent	const p_0	-0.062±0.042	0.035±0.042
	$A_{LU}^{\sin\phi}$	-0.244±0.060	-0.244±0.060
	$A_{LU}^{\sin 2\phi}$	0.048±0.059	0.052±0.059

Summarizing, it is shown that the method of normalization does not effect the BSAs $A_{LU}^{\sin\phi}$ and $A_{LU}^{\sin 2\phi}$, as expected. The constant term p_0 is shifted up by about one sigma in the luminosity method.

5.5 Study of different Fit Methods

5.5.1 The Influence of Binning

In order to estimate the effect of binning for the azimuthal angle ϕ for the BSA, a calculation with different number of ϕ-bins is performed. In figure 5.6 $A_{LU}^{\sin\phi}$ and $A_{LU}^{\sin 2\phi}$ are plotted in dependence on the number of ϕ-bins. For the coherent part the average

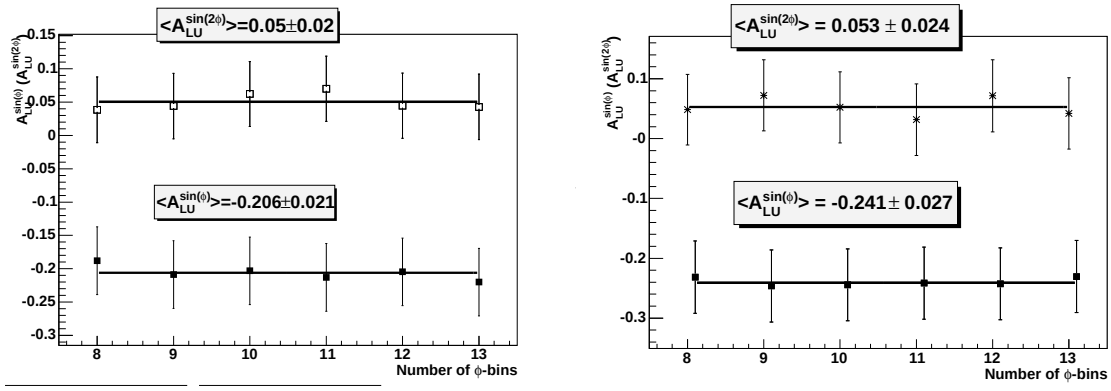

Figure 5.6: $A_{LU}^{\sin\phi}$ and $A_{LU}^{\sin 2\phi}$ in dependence on the number of ϕ-bins for the coherent (left) and incoherent (right) part.

$A_{LU}^{\sin\phi}$ ($A_{LU}^{\sin 2\phi}$) is -0.206 (0.05) with an uncertainty of ± 0.021 (± 0.02). The number of ϕ-bins varied from 8 to 13. For the incoherent part the average $A_{LU}^{\sin\phi}$ ($A_{LU}^{\sin 2\phi}$) is -0.241 (0.053) with an uncertainty of ± 0.027 (± 0.024). In comparison to the usual fit method with 10 ϕ-bins the difference is less then 0.01 for $A_{LU}^{\sin\phi}$ and less than 0.02 for $A_{LU}^{\sin 2\phi}$, i.e. can be neglected at the present level of statistics.

5.5.2 The Fit Function

The standard fit-function is given as

$$f(\phi) = p_0 + p_1 \sin\phi + p_2 \sin 2\phi \tag{5.2}$$

In order to study the influence of additional harmonics, the following fit functions are applied:

$$f(\phi) = p_1 \sin\phi \tag{5.3}$$
$$f(\phi) = p_0 + p_1 \sin\phi + p_2 \sin 2\phi + p_3 \sin 3\phi + p_4 \sin 4\phi \tag{5.4}$$
$$f(\phi) = p_0 + p_1 \cos\phi + p_2 \cos 2\phi \tag{5.5}$$

The corresponding BSA results are shown in figure 5.7 for the coherent part. Note that the amplitudes can not change by using additional parameters in the fit-function, e.g. shown in the top part in figure 5.7 for $A_{LU}^{\sin\phi}$:

$$p_1 \sin\phi \quad A_{LU}^{\sin\phi} = -0.208 \pm 0.05$$
$$p_0 + p_1 \sin\phi + p_2 \sin 2\phi \quad A_{LU}^{\sin\phi} = -0.203 \pm 0.051$$

The results of this study can be summarized in the following:

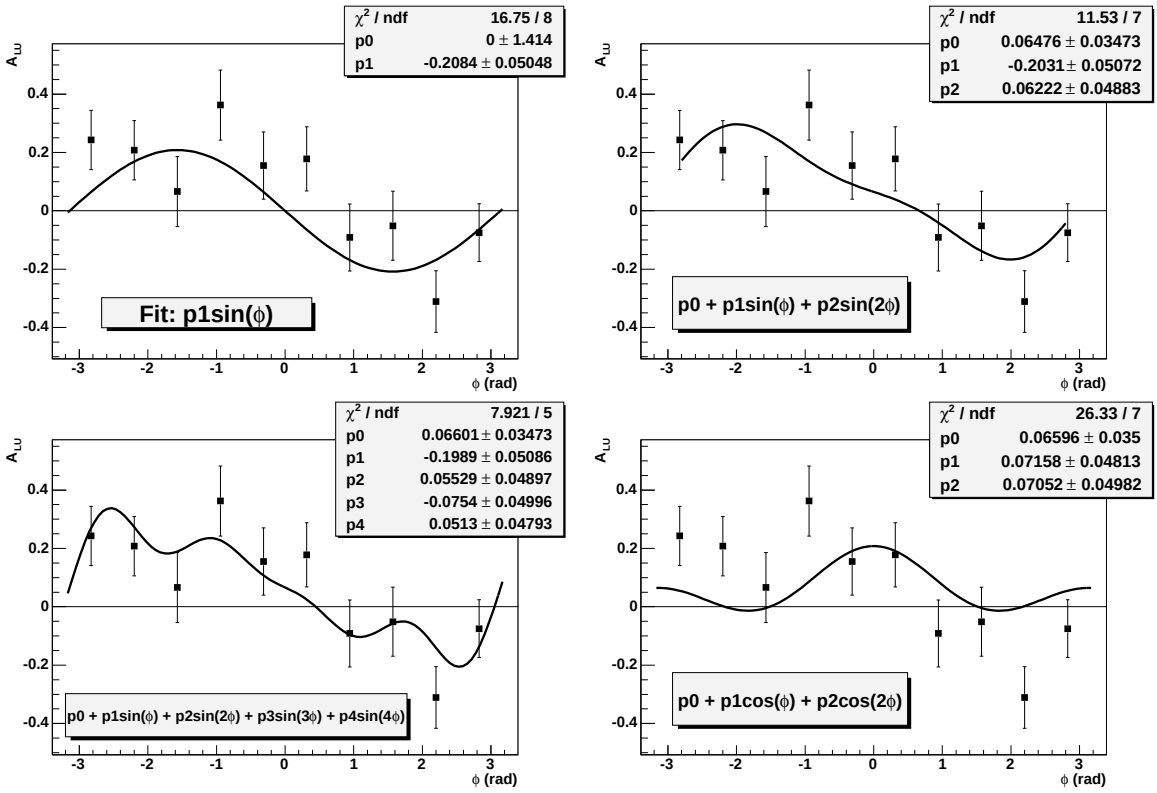

Figure 5.7: The BSA results with different fit functions for the coherent part.

- $A_{LU}^{\sin 3\phi}$ and $A_{LU}^{\sin 4\phi}$ are given as

$$\begin{aligned} A_{LU}^{\sin 3\phi} &= -0.075 \pm 0.05 \\ A_{LU}^{\sin 4\phi} &= -0.051 \pm 0.048 \end{aligned}$$

  A theoretical interpretation of these higher harmonics is only known for proton and not for nuclei. In addition they have too small statistics and therefore they will not be further discussed here.

- The $\cos\phi$-dependence is negligible within the statistical errors. Note that a non-zero $\cos\phi$ amplitude is forbidden from theory.

The same conclusions hold for the incoherent sample.

5.5.3 The Anti-symmetrization Fit Method

The anti-symmetrization fit method is characterized by mapping the region $[-\pi, 0]$ to the region $[0, \pi]$, which projects out the *odd* part in ϕ in the BSA. Hence the *even* harmonics disappear, especially acceptance effects. This means, anti-symmetrized BSAs, by ansatz, are not sensitive (anymore) to a possible constant term p_0, as this is also an *even* contribution.

For the beam-spin asymmetry on an unpolarized target, two different formulae exist for the anti-symmetrization:

1st way: A_{LU} can be calculated for each ϕ-bin as

$$A_{LU} = \frac{1}{< |P| >} \frac{\frac{\overrightarrow{N}(\phi) - \overrightarrow{N}(-\phi)}{\overrightarrow{Norm}} - \frac{\overleftarrow{N}(\phi) - \overleftarrow{N}(-\phi)}{\overleftarrow{Norm}}}{\frac{\overrightarrow{N}(\phi)}{\overrightarrow{Norm}} + \frac{\overrightarrow{N}(-\phi)}{\overrightarrow{Norm}} + \frac{\overleftarrow{N}(\phi)}{\overleftarrow{Norm}} + \frac{\overleftarrow{N}(-\phi)}{\overleftarrow{Norm}}} \tag{5.6}$$

In terms of the cross-section

$$\frac{d\sigma}{d\phi} = \underbrace{\frac{d\sigma_U}{d\phi}}_{even\ in\ \phi} + \underbrace{\frac{d\sigma_L}{d\phi} P_L}_{odd\ in\ \phi} \tag{5.7}$$

the above defined asymmetry turns out to be theoretically correct:

$$A_{LU} = \frac{1}{P_L} \frac{P_L \frac{d\sigma_L}{d\phi} - (-P_L)\frac{d\sigma_L}{d\phi}}{\frac{d\sigma_U}{d\phi} + \frac{d\sigma_U}{d\phi}} = \frac{\frac{d\sigma_L}{d\phi}}{\frac{d\sigma_U}{d\phi}} \tag{5.8}$$

2nd way: Alternatively, A_{LU} can be calculated *separately for each helicity state* and ϕ-bin:

$$\overrightarrow{A_{LU}} = \frac{1}{< \overrightarrow{|P|} >} \frac{\overrightarrow{N}(\phi) - \overrightarrow{N}(-\phi)}{\overrightarrow{N}(\phi) + \overrightarrow{N}(-\phi)} \tag{5.9}$$

$$\overleftarrow{A_{LU}} = \frac{1}{< \overleftarrow{|P|} >} \frac{\overleftarrow{N}(\phi) - \overleftarrow{N}(-\phi)}{\overleftarrow{N}(\phi) + \overleftarrow{N}(-\phi)} \tag{5.10}$$

In terms of cross sections

$$\overrightarrow{A_{LU}} = \frac{\overrightarrow{P}\frac{d\sigma_L}{d\phi}}{\overrightarrow{P}\frac{d\sigma_U}{d\phi}} = \frac{\frac{d\sigma_L}{d\phi}}{\frac{d\sigma_U}{d\phi}} = -\overleftarrow{A_{LU}} \tag{5.11}$$

also the 2nd way to calculate the anti-symmetrized BSA is correct.

In comparison with the standard (non-symmetrized) fit method both ways share the fact that local acceptance effects cancel out. In addition, the second way provides the

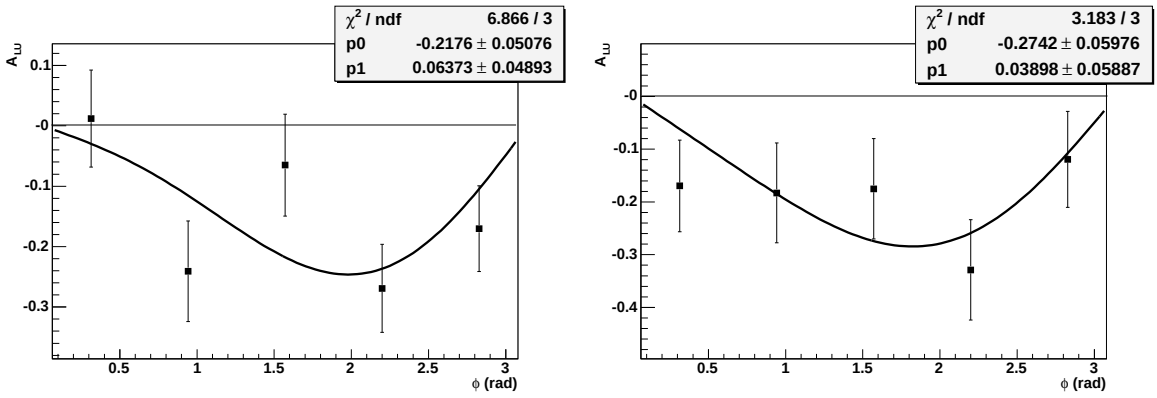

Figure 5.8: The BSA obtained via the anti-symmetrization method for the coherent (left) and incoherent (right) part.

advantage that any helicity-dependent acceptance effects (as e.g. beam envelopes and/or vertex positions depending on helicity) drop out, as long as they are even in ϕ.

The final BSA, in the second way of antisymmetrization, can be obtained as the weighted average of both measurements:

$$A_{LU} = \frac{\sum_{i,k} \overrightarrow{w^i}\overrightarrow{A^i_{LU}} - \overleftarrow{w^k}\overleftarrow{A^k_{LU}}}{\sum_{i,k} \overrightarrow{w^i} + \overleftarrow{w^k}}, \tag{5.12}$$

where $i(k)$ runs over helicity periods $\rightarrow$ ($\leftarrow$). The weighting can be done either by normalization $w = Norm$ or by the statistical error $w = \frac{1}{(\delta A_{LU})^2}$, which in fact should be equivalent. Note that although the statistical uncertainty per bin decreases by about $\sqrt{2}$, the resulting uncertainties of the fit stays the same, as the number of bins was halved. The result of the anti-symmetrization method via the 2nd way is plotted in figure 5.8. The asymmetries A_{LU} are fitted with the function

$$p_0 \sin\phi + p_1 \sin 2\phi.$$

Note that the weighting is done by the statistical error $w = \frac{1}{(\delta A_{LU})^2}$ for each helicity state. The result of this anti-symmetrization method in comparison with the standard (non-symmetrized) fit method is given in the following table:

	Coherent	Incoherent
non-symmetrized	$A_{LU}^{\sin\phi} = -0.20 \pm 0.05$	$A_{LU}^{\sin\phi} = -0.24 \pm 0.06$
anti-symmetrized	$A_{LU}^{\sin\phi} = -0.22 \pm 0.05$	$A_{LU}^{\sin\phi} = -0.27 \pm 0.06$

Summarizing, the BSA results obtained via the anti-symmetrization fit method are in good agreement with the results of the standard fit method.

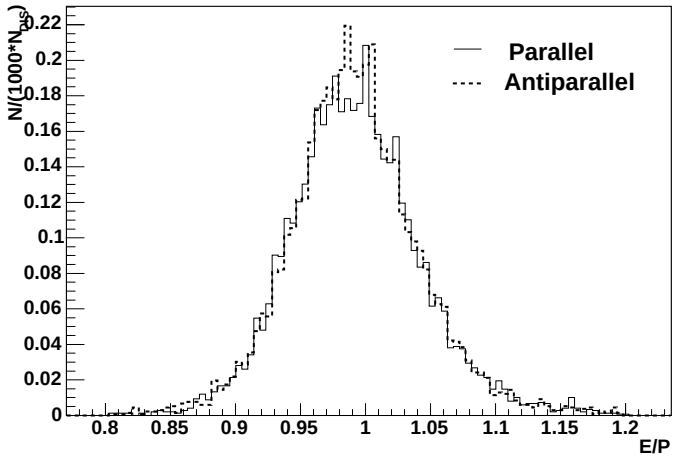

Figure 5.9: Distribution of the ratio between the lepton energy deposited in the calorimeter E and the momentum of the lepton P, derived from the x-slope difference between the front and the back track, for the parallel and antiparallel helicity state.

5.6 The Influence of the Calorimeter on the Results

5.6.1 Study of the Photon Energy Reconstruction

Since the calorimeter is the only detector able to measure the energy and position of the photon, it is very important for this analysis. In order to check the reconstruction of the photon energy from the calorimeter measurement, the ratio between the lepton energy deposited in the calorimeter E and the momentum of the lepton P is used. The latter is derived from the x-slope difference between the front and the back track. The distribution for the value E/P for the lepton sample is shown in figure 5.9 for the parallel and antiparallel helicity state. The mean value is extracted by a gaussian fit function and the result is given as

$$\left(\frac{E}{P}\right)_{Mean} = 0.991 \pm 0.001,$$

being the same for parallel as well as antiparallel helicity. Hence there is no difference in the energy reconstruction from the calorimeter when comparing both helicity states.

5.6.2 Study of the Photon Position Reconstruction

Another important quantity for this analysis is the resolution of the position reconstruction of the calorimeter. In order to cross check the position measurement of the

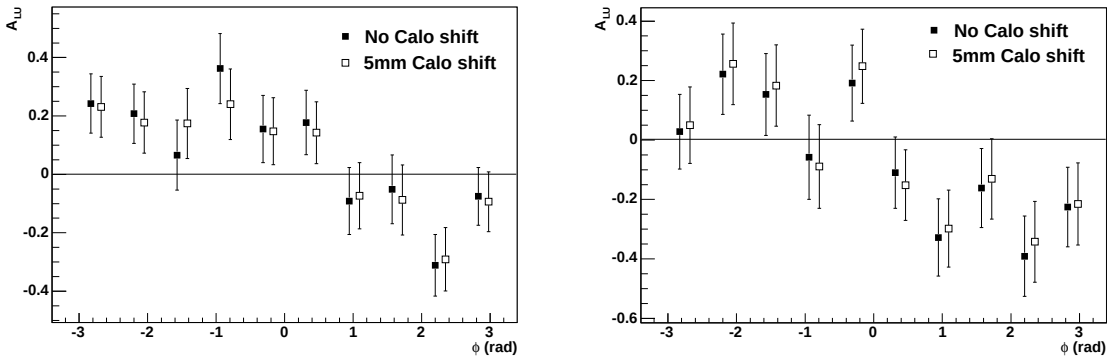

Figure 5.10: Comparison between the results achieved with and without -5 mm correction of the photon position in the top part of the calorimeter for the coherent (left) and incoherent sample (right).

calorimeter, the reconstructed cluster position for charged tracks can be used. Note that the position reconstruction in the calorimeter behaves similarly for leptons and photons, because the photons used in this analysis convert into lepton pairs in the preshower detector, which is located in front of the calorimeter. Investigating the difference $y_{track} - y_{calo}$ separately for the top and the bottom part of the calorimeter reveals that the mean of this distribution in the top part is about zero while it is about -5 mm in the bottom part for the year 2000 [Ell].

The influence on the asymmetry A_{LU} of this position shift is calculated by using a -5 mm correction of the photon position in the top part of the calorimeter. A comparison between the results achieved with and without the correction is shown in figure 5.10 for the coherent and incoherent sample. The results for the BSAs are given in the following table.

		No Correction	5mm Correction
Coherent	const p_0	0.065±0.035	0.055±0.035
	$A_{LU}^{\sin\phi}$	-0.203±0.051	-0.199±0.051
	$A_{LU}^{\sin 2\phi}$	0.062±0.049	0.072±0.049
Incoherent	const p_0	-0.062±0.042	0.045±0.042
	$A_{LU}^{\sin\phi}$	-0.244±0.06	-0.242±0.06
	$A_{LU}^{\sin 2\phi}$	0.048±0.059	0.046±0.06

The influence on $A_{LU}^{\sin\phi}$ ($A_{LU}^{\sin 2\phi}$) is less than 0.005 (0.011).

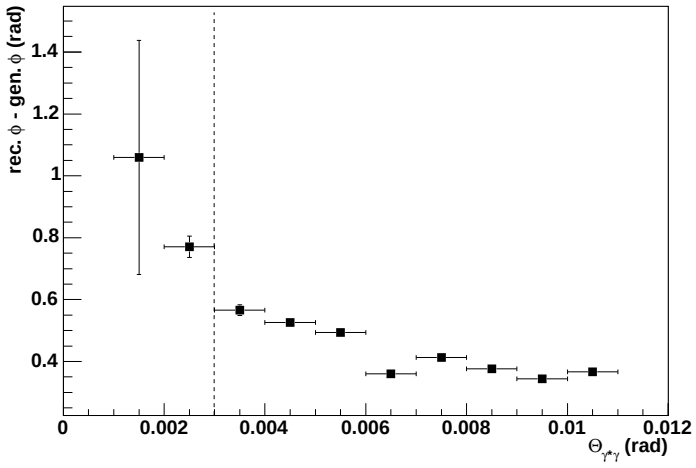

Figure 5.11: Average difference between generated ϕ and reconstructed ϕ in dependence on $\theta_{\gamma^*\gamma}$.

5.7 Smearing Effects

Smearing effects are mainly of interest as they change the relative direction of the real photon with respect to that of the virtual photon. Therefore they change the value of the azimuthal angle ϕ as well as the polar angle $\theta_{\gamma^*\gamma}$ and the momentum transfer t_c. The smearing of the photon can be studied by using MC and comparing the generated photon direction with the reconstructed photon direction. In figure 5.11 the average difference between the generated ϕ and the reconstructed ϕ is shown in dependence of $\theta_{\gamma^*\gamma}$. The lower cut for $\theta_{\gamma^*\gamma}$ was set to 3 mrad, in order to reduce smearing effects in ϕ. The remaining smearing for an asymmetry has been obtained in a MC simulation in 4 bins in t. The generated asymmetry amplitude is 0.5. It is shown in figure 5.12 that smearing effects reduce the generated asymmetry by about 0.02 (0.04) in the coherent (incoherent) part. Hence an relative error of 4% (8%) of the asymmetry amplitude in the coherent (incoherent) sample is estimated.

5.8 Determination of the Background Contribution

The background for DVCS originates from the production of photons produced in a semi-inclusive or exclusive background (= exclusive reaction other than DVCS). It was derived from MC studies that the main part stems from π^0 meson production ($\simeq$80%) and the rest is dominated by photons from the decay of the η meson. The general

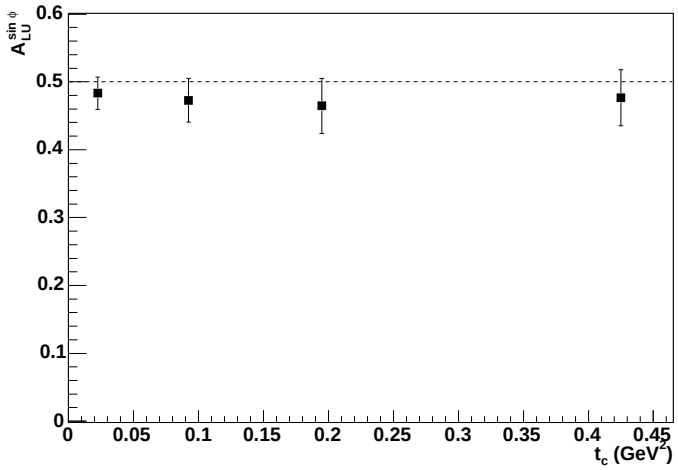

Figure 5.12: Reconstructed $A_{LU}^{\sin\phi}$ from a MC simulation with a generated asymmetry amplitude of 0.5, for different t_c bins.

problem in the data analysis is not only the exclusive π^0-or η production, which are almost indistinguishable from BH-DVCS under certain kinematic constraints, but also semi-inclusive processes can leak into the exclusive sample. Since there are statistical fluctuations in the measured energy deposition in the calorimeter, the energy of the single photon cluster can be overestimated such that the missing mass gets closer to the exclusive range.

The fraction of the background in dependence of t is studied in [Kra]. The upper limit for the coherent sample is 7% and it increases to 14% for the incoherent sample. In order to determine the uncertainty of the beam-spin asymmetry results caused by the background contribution, the asymmetry of the background has to be estimated. Since the largest contribution stems from the π^0 meson, it is important to determine the beam-spin asymmetry in semi-inclusive π^0 production, which is found to be less than 3% [HERMES04a]. In summary the uncertainty caused by background contributions is approximately given as:

$$A_{bkg} = 0.03\ \eta(t)$$

where η denotes the fraction of the dataset that originates from background: $\eta = \frac{N_{bkg}}{N_{tot}}$

5.9 Combined Systematic Uncertainties

In addition to the statistical uncertainty, as given in equation 4.9, the estimation of the systematic uncertainties is also important. Therefore the results described in the

previous sections are used. The total systematic uncertainty arises from the following uncertainties:

- Photons from the semi-inclusive background and exclusive reactions other than DVCS: It was derived from MC studies that the main part stems from π^0 meson ($\simeq$80%) and the rest is dominated by photons from the decay of the η meson. For the coherent (incoherent) part the upper limit of the uncertainty is 0.003 (0.005), as discussed in section 5.8.
- Detector smearing: The relative error is estimated to be 4% (8%) of the asymmetry amplitude in the coherent (incoherent) sample, as explained in section 5.7. These values include binning effects as discussed in section 5.5.1.
- Uncertainty of the polarization measurement: The measurement of the beam-polarization is done by two polarimeters (see section 3.1.) in parallel. Usually, the polarization value is taken from the longitudinal polarimeter (LPOL) since it has a smaller systematic uncertainty (1.6%). Only if there are some problems in the LPOL during operation, the values of the transverse polarimeter (TPOL) with a systematic uncertainty of 3.4% are taken. The resulting systematic uncertainty is 1.9% of the beam polarization. Hence the uncertainty of the asymmetry is 0.004 for the coherent part and 0.005 for the incoherent part.
- The systematic uncertainty of a vertical calorimeter shift (alignment) was found to be 0.005 (0.003) for the coherent (incoherent) part, as described in section 5.6.2.

The combined systematic uncertainty is obtained by adding in quadrature the uncertainties listed above. The systematic uncertainty for the coherent part is

$$dA_{LU}^{\sin\phi}(syst) = 0.011 \tag{5.13}$$

and for the incoherent part

$$dA_{LU}^{\sin\phi}(syst) = 0.021. \tag{5.14}$$

5.10 Study of the Constant Term

In the fits to extract the BSAs, as shown in figure 4.13, a non-negligible constant term p_0 is found for the coherent part ($p_0 = 0.065 \pm 0.035$), as well as for the incoherent part ($p_0 = -0.062 \pm 0.041$). Note that the sign of p_0 is different for each part and that consequently the sum of both parts in figure 4.6 shows no constant term p_0. For the coherent part, p_0 is two times the statistical error (2σ), which corresponds to a probability of 95% not to be caused by statistical effects. Since there is no known theoretical reason for a constant term, which could explain a ϕ-independent different

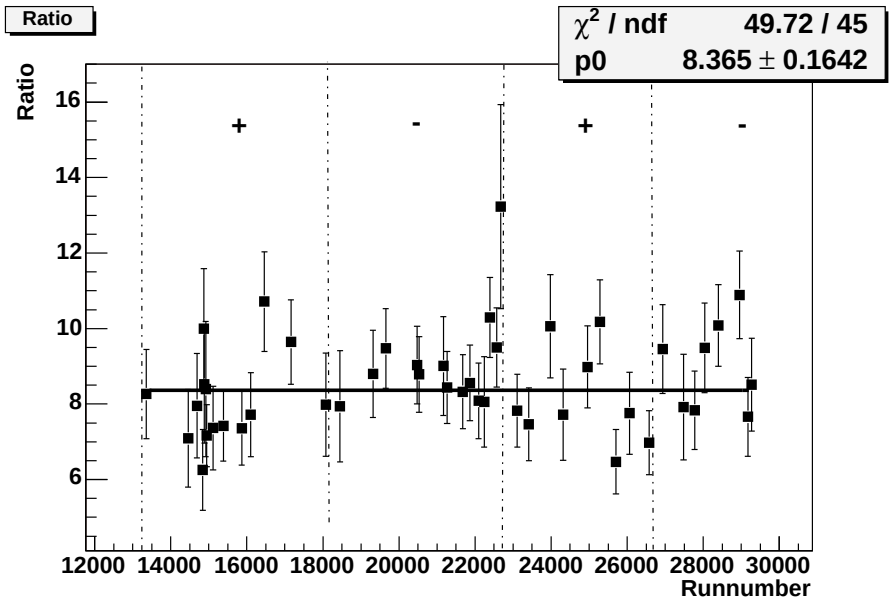

Figure 5.13: Ratio of coherent DVCS to DIS events per fill. The vertical lines indicate different helicity running periods.

cross-section between parallel and antiparallel helicity states, the only remaining reason can be due to systematic differences. Because of the ϕ-independence, p_0 is defined by the difference between the ratio of $\frac{DVCS}{DIS}$ for both helicity states, given as

$$p_0 = \frac{1}{< P >} \frac{\frac{\overrightarrow{N_{DVCS}}}{\overrightarrow{N_{DIS}}} - \frac{\overleftarrow{N_{DVCS}}}{\overleftarrow{N_{DIS}}}}{\frac{\overrightarrow{N_{DVCS}}}{\overrightarrow{N_{DIS}}} + \frac{\overleftarrow{N_{DVCS}}}{\overleftarrow{N_{DIS}}}} \tag{5.15}$$

In order to find the systematic reason for p_0, several systematic studies are performed in the following.

5.10.1 The Time Dependence of p_0

Since there is no physical reasons for a different ratio of $\frac{DVCS}{DIS}$ events, a strong evidence for a time-dependent change of some detector properties exists. For example, a different ratio could be caused by a change in the detector efficiency between two run periods, which correspond to different beam helicity states. In order to estimate the time dependence, the ratio $\frac{DVCS}{DIS}$ is calculated per fill for the coherent sample, as shown in figure 5.13. In particular, the region from run 14000 to run 16000 shows a significantly low ratio.

5.10.2 Study of Systematic Influences

In order to identify a systematic origin for the non-zero value of p_0, a number of studies has been done:

- The standard normalization is done per DIS events. In addition, the normalization per luminosity is performed as described in section 5.4. The result by using the luminosity is shown in figure 5.5 with $p0 = 0.095 \pm 0.035$. Since p_0 does not disappear, p_0 can not be caused by wrong normalization.

- A different photon energy reconstruction of the calorimeter between both helicity states was also considered. Since the energy reconstruction E/P is the same for both helicity states, as described in section 5.6.1, it could not cause a constant term. In addition there is also no difference in E/P, depending on the position in the calorimeter.

- The photon position reconstruction was reviewed and described in 5.6.2. The result, calculated with a correction of -5 mm in the top part of the calorimeter, gives a constant term p_0 reduced by 0.01, as described in section 5.6.2.

- Another possibility could arise from a variation of the efficiency in the hodoscope H0. In order to calculate the H0 inefficiency, the number of DIS events was counted by using trigger-18 in comparison to trigger-21. Since the only difference between trigger-18 and trigger-21 is the required signal in H0, the efficiency is given by the ratio of the number of trigger-18 events with and without trigger-21. The H0 efficiency is calculated for a grid of $2\times2\text{cm}^2$ across the H0 scintillator plane using the lepton tracks that passed trigger-18. The correction is done by weighting the respective events with the inverse efficiency for each run period. The results show a negligible influence (less than 2%) for p_0 as well as for $A_{LU}^{\sin\phi}$ and $A_{LU}^{\sin 2\phi}$.

- Usually the threshold of the calorimeter is set at 3.5 GeV for high density runs and 1.4 GeV for standard-density runs. In fact, the threshold was also set for several high-density runs at 1.4, which could have an influence on the acceptance. In order to estimate this influence, the BSA is calculated without these runs and compared to the standard result. The differences for $A_{LU}^{\sin\phi}$ and $A_{LU}^{\sin 2\phi}$ are negligible. For p_0 the difference is about 0.006 and can be included in its systematic uncertainty.

- Since high density runs with neon are usually following standard ABS density hydrogen data taking, a possible systematic deviation should be also be seen in the hydrogen data. Therefore, the hydrogen data of the according time periods is analyzed by using the same cuts as in the neon analysis. In the hydrogen results no constant term appears.

- In addition to the studies discussed above, the following kinematic variables are reviewed for differences in the distributions between both helicity states: Q^2, W^2,

ν, x_{Bj}, y_{Bj}, t_c, θ, ϕ_{lepton}, P, $\theta_{\gamma^*\gamma}$, E_γ, M_x^2, z_{vtx}, t_{vtx} and the beam energy. Summarizing, a significant variation can be only seen in t_c and $\theta_{\gamma^*\gamma}$ as well as in the M_x distribution, illustrated in figure 5.14

A combined systematic uncertainty for p_0 is obtained by adding in quadrature the uncertainties of the photon position and the H0 inefficiency. From that the systematic uncertainty for p_0 is given as

$$dA_{LU}^{p_0}(syst) = 0.012. \tag{5.16}$$

This is clearly not covering the observed 2σ deviations of p_0. As a non-zero value for p_0 can only be due to experimental systematic problems, it must at present be assigned to unknown sources of systematic uncertainties.

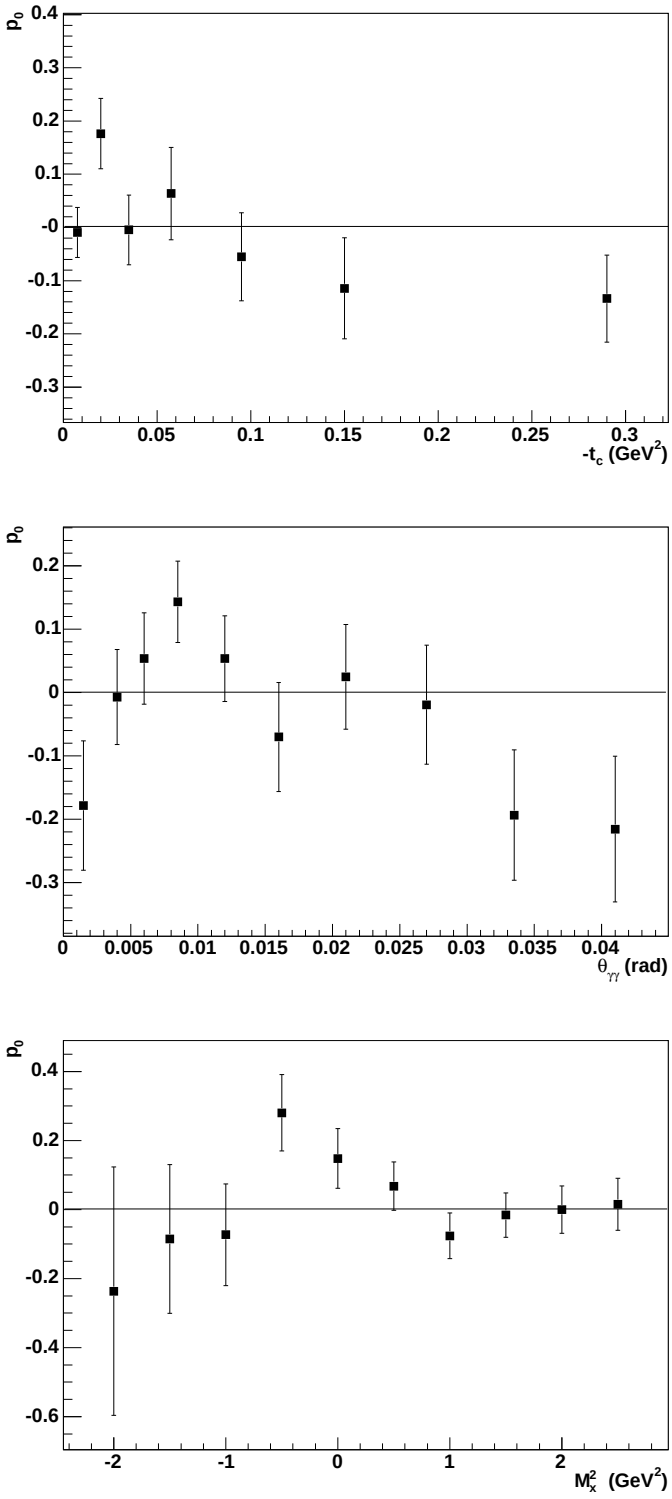

Figure 5.14: The constant term p_0 in dependence of the kinematic variables t_c, $\theta_{\gamma^*\gamma}$ and M_x^2 for full sample.

6 Summary of the Results

In this chapter the beam-spin asymmetries extracted in Deeply Virtual Compton Scattering using a neon target and their kinematic dependences are presented . The interpretation and a comparison with hydrogen data will be discussed in the next chapter.

All data for this study was accumulated during the 2000 running period of HERA using a polarized positron beam with an average polarization of 54%. The measurements amount to an integrated luminosity of about 82 pb^{-1}. For the mostly coherent (incoherent) part the exclusive single photon sample contains 1394 (909) events in the parallel helicity state and 1470 (1102) in the antiparallel helicity state.

The asymmetries have been extracted in dependence on the variables x_{Bj}, $-t_c$, Q^2 within their kinematic constraints, given as:

$$\begin{array}{ccccc} 0.03 & < & x_{Bj} & < & 0.35 \\ & & -t_c & < & 0.7\ \mathrm{GeV}^2 \\ & & Q^2 & > & 1\ \mathrm{GeV}^2 \end{array}$$

A separation between coherent and incoherent exclusive sample is done at $-t_c = 0.045$, whereby the coherent (incoherent) sample is constrained as $-t_c < 0.045$ ($-t_c >= 0.045$). The average values of the kinematic variables for the coherent and incoherent exclusive sample are:

	Coherent	Incoherent
$\langle x_{Bj} \rangle$	0.068	0.107
$\langle -t_c \rangle$	0.019 GeV^2	0.163 GeV^2
$\langle Q^2 \rangle$	1.75 GeV^2	2.76 GeV^2

6.1 Coherent Sample

The result for A_{LU} is plotted in figure 6.1 in dependence on ϕ using the fit function

$$f(\phi) = p_0 + p_1 \sin\phi + p_2 \sin 2\phi. \tag{6.1}$$

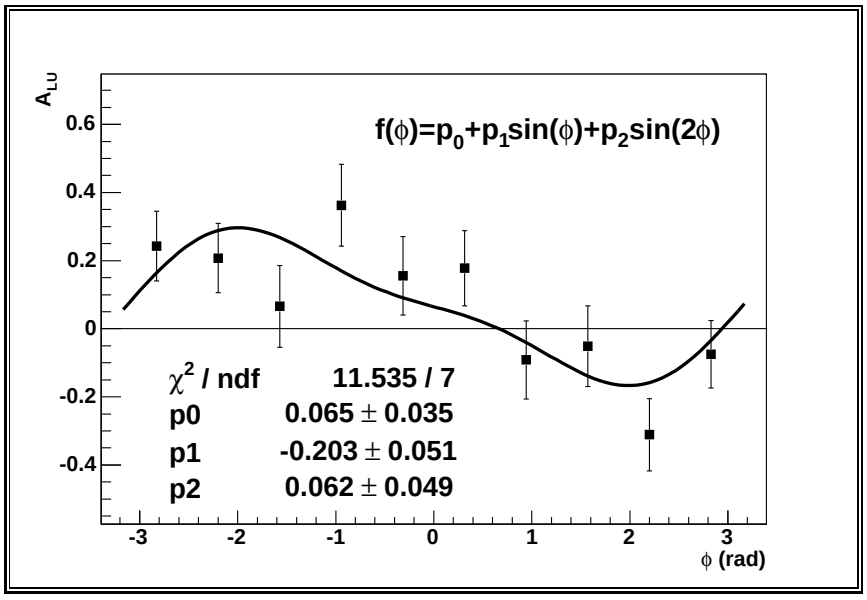

Figure 6.1: Beam spin asymmetry on unpolarized neon (2000) in 10 bins of ϕ for the coherent sample. The three-parameter fit function $f(\phi)$ and its coefficients are also shown.

Note that the parameters p_0, p_1 and p_2 correspond to the constant term, to the amplitude $A_{LU}^{\sin\phi}$ and to the amplitude $A_{LU}^{\sin 2\phi}$. A clear left/right asymmetry is visible. This is related to the negative amplitude of $A_{LU}^{\sin\phi}$ with a statistical significance of 4σ. The amplitude $A_{LU}^{\sin 2\phi}$ is positive with a very small statistical significance of 1.3σ and therefore no kinematic dependences are shown for it. In addition there is a positive constant term p_0 with a statistical significance of 1.9σ. The asymmetry $A_{LU}^{\sin\phi}$ is clearly non-zero:

$$\boxed{A_{LU}^{\sin\phi} = -0.203 \pm 0.051(stat) \pm 0.011(syst)}$$

with a significance of 3.9σ when quadratically combining statistical and systematic uncertainties.

The extracted amplitudes $A_{LU}^{\sin\phi}$ for the coherent sample are shown in figure 6.2 in dependence on x_{Bj}, $-t_c$, Q^2, whereby the respective other two variables were integrated over in each case. The numerical results and the average kinematics of the respective other two variables are presented in the appendix (table 9.1). The dependences on x_{Bj} and Q^2, shown in the top and bottom panel, appear to be not very strong within the statistical uncertainty. Looking at the dependence on $-t_c$ in the middle panel, the very low t_c region ($-t_c \lesssim 0.03$) seems to have a significant non-zero asymmetry.

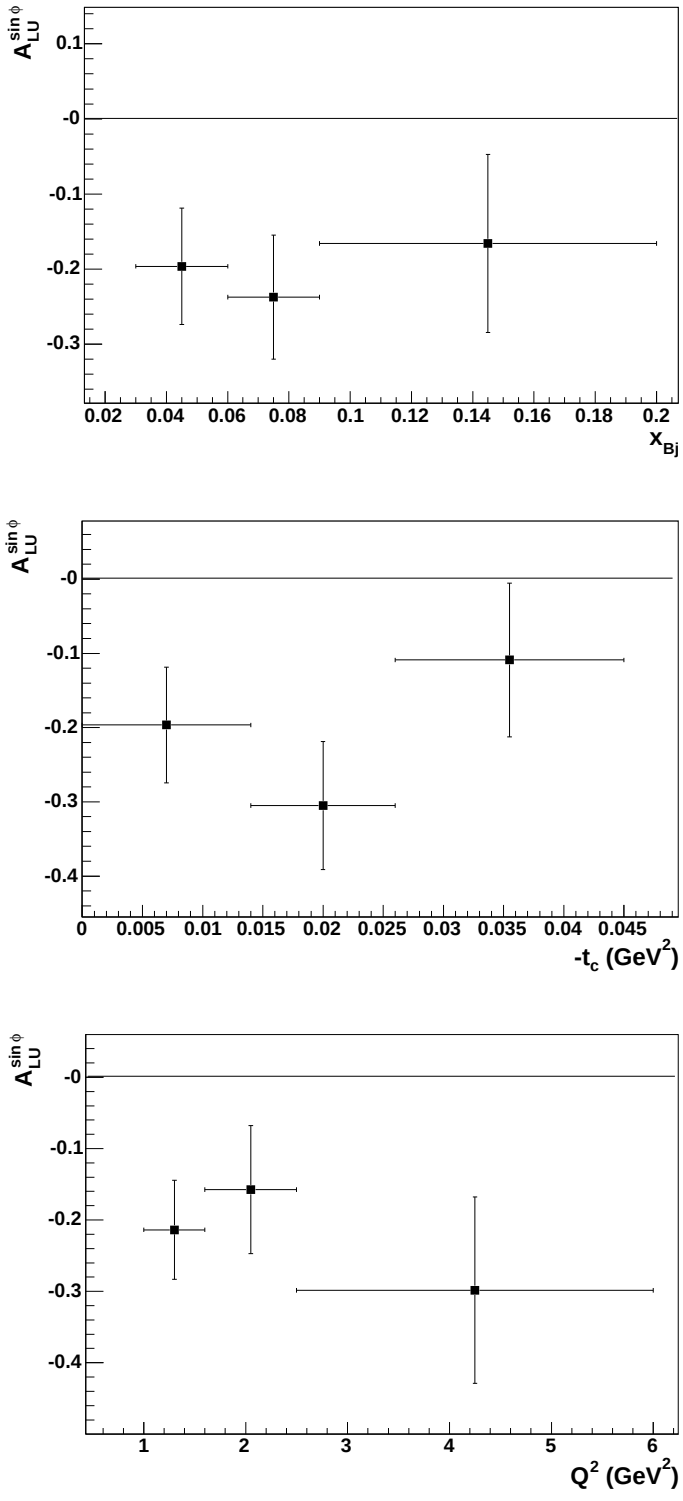

Figure 6.2: $A_{LU}^{\sin\phi}$ for the coherent sample in dependence on the kinematical variables x_{Bj}, $-t_c$, Q^2.

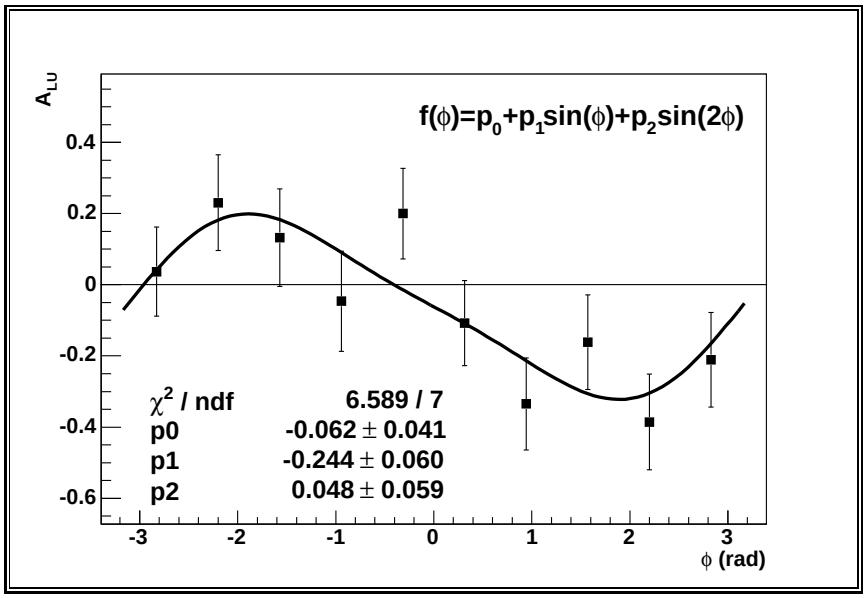

Figure 6.3: Beam spin asymmetry on unpolarized neon (2000) in ten bins of ϕ for the incoherent sample. The three-parameter fit function $f(\phi)$ and its coefficients are also shown.

6.2 Incoherent Sample

For the incoherent sample the extracted asymmetry A_{LU} is shown in figure 6.3, fitted with the same function as in the case of the coherent sample (equation 6.1). A significant negative amplitude of $A_{LU}^{\sin\phi}$ is visible:

$$\boxed{A_{LU}^{\sin\phi} = -0.244 \pm 0.06(stat) \pm 0.021(syst)}$$

with a significance of 3.8σ when adding quadratically statistical and systematic uncertainties. $A_{LU}^{2\sin\phi}$ is found to be compatible with zero and therefore no kinematic dependences are shown. The constant term p_0 is small and negative with a significance of 1.5σ.

The extracted amplitudes $A_{LU}^{\sin\phi}$ for the incoherent sample are shown in figure 6.4 in dependence on x_{Bj}, $-t_c$, Q^2. The numerical results are presented in the appendix (table 9.2) in conjunction with the corresponding average kinematic values. Because of the small statistics no significant dependence on x_{Bj}, $-t_c$ and Q^2 can be seen.

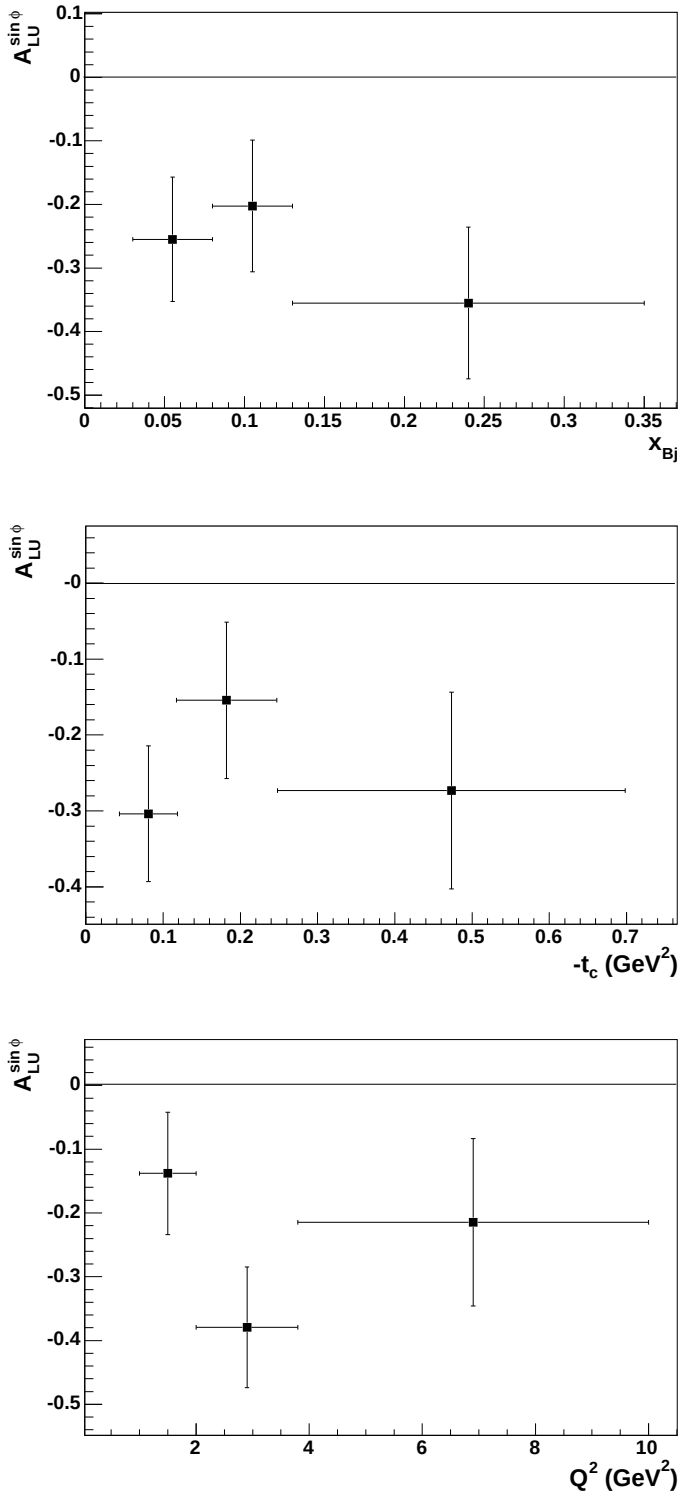

Figure 6.4: $A_{LU}^{\sin\phi}$ for the incoherent sample in dependence on x_{Bj}, $-t_c$, Q^2.

7 Interpretation in the Light of Theoretical Models

In the following, the results obtained on neon in the last chapter are compared with hydrogen results and nuclear effects predicted from theoretical models are discussed. Since hydrogen consists only of one proton in comparison to a neon nucleus (Ne-20) with 10 protons and additional 10 neutrons, some nuclear effects can be expected, as explained in section 2.5.

7.1 Comparison with Hydrogen Data

The hydrogen data was accumulated in the running period 2000 and analyzed using the same kinematic cuts as for neon, described in section 4.1. Note that the hydrogen results are compatible with released results [Now05, Ell] as shown in section 4.3. According to the fact that the neon data is separated in a coherent and incoherent sample, also the hydrogen data is separated into the same t_c regions: $-t_c < 0.045$ GeV^2 for the coherent sample and $-t_c > 0.045$ GeV^2 for the incoherent sample. In the following table a comparison between the results for neon and hydrogen is presented.

		Neon	Hydrogen
Coherent	const p_0	0.065±0.035	-0.011±0.036
	$A_{LU}^{\sin\phi}$	**-0.203±0.051**	**-0.152±0.051**
	$A_{LU}^{\sin 2\phi}$	0.062±0.049	-0.021±0.050
Incoherent	const p_0	-0.062±0.042	-0.048±0.026
	$A_{LU}^{\sin\phi}$	**-0.244±0.060**	**-0.213±0.037**
	$A_{LU}^{\sin 2\phi}$	0.048±0.059	0.010±0.037

For both coherent and incoherent part the amplitudes $A_{LU}^{\sin\phi}$ on neon and hydrogen agree within one sigma of the statistical uncertainty.

In figure 7.1 the comparison of $A_{LU}^{\sin\phi}$ and $A_{LU}^{\sin 2\phi}$ in dependence of t_c is shown. The binning in t_c has been chosen, since it is the best variable to discriminate between different processes. In the bottom part the corresponding ratios of neon over proton

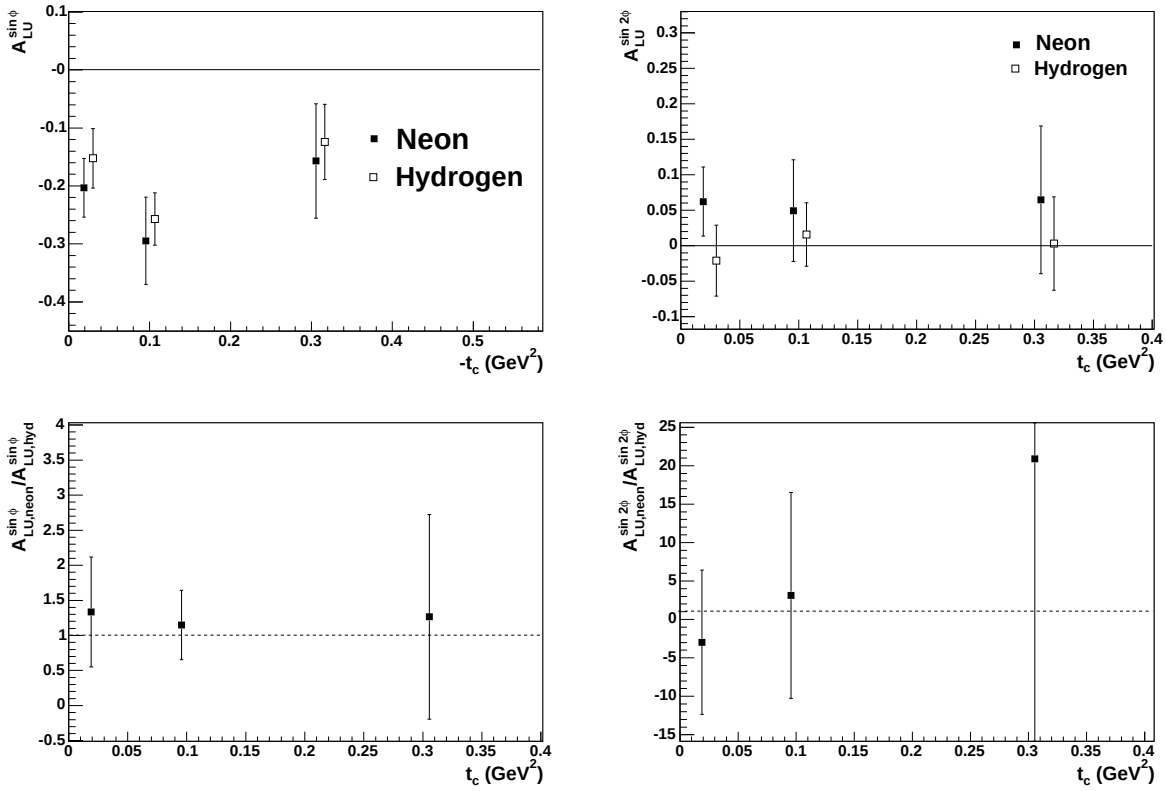

Figure 7.1: Comparison of the asymmetry amplitude $A_{LU}^{\sin\phi}$ (left panel) and $A_{LU}^{\sin 2\phi}$ (right panel) vs. t_c for neon (filled squares) and hydrogen (empty squares). In the bottom part the ratios of neon over proton asymmetry are shown as $A_{LU,neon}^{\sin\phi}/A_{LU,hyd}^{\sin\phi}$ and $A_{LU,neon}^{\sin 2\phi}/A_{LU,hyd}^{\sin 2\phi}$. Note that error bars with a larger value than the y-axis are cut off and hence not shown in their full length.

asymmetry are shown. Note that error bars with a larger value than the y-axis are cut off and therefore not shown in their full length. Looking at the left panel, the asymmetry $A_{LU}^{\sin\phi}$ is systematically slightly larger for neon than for hydrogen in all t_c bins although fully compatible within error bars. Also the asymmetries $A_{LU}^{\sin 2\phi}$ seems to be larger for neon than for hydrogen in a similar way. Because the latter are compatible with zero, the ratio $\frac{A_{LU,neon}^{\sin 2\phi}}{A_{LU,hyd}^{\sin 2\phi}}$ will not be further discussed here. In the appendix (table 9.3) the numerical results of $A_{LU,neon}^{\sin\phi}$ and $A_{LU,hyd}^{\sin\phi}$ with the average values of the kinematic variables are given for each t_c bin. A comparison of $A_{LU}^{\sin\phi}$ between neon and hydrogen in dependence on the variables x_{Bj} and Q^2 is presented in figure 7.2. No significant effect is found within statistical uncertainties. A study of the ratio $\frac{A_{LU}^{neon}}{A_{LU}^{hyd}}$ in dependence on the azimuthal angle ϕ, presented in figure 7.3, shows no visible harmonics for all three

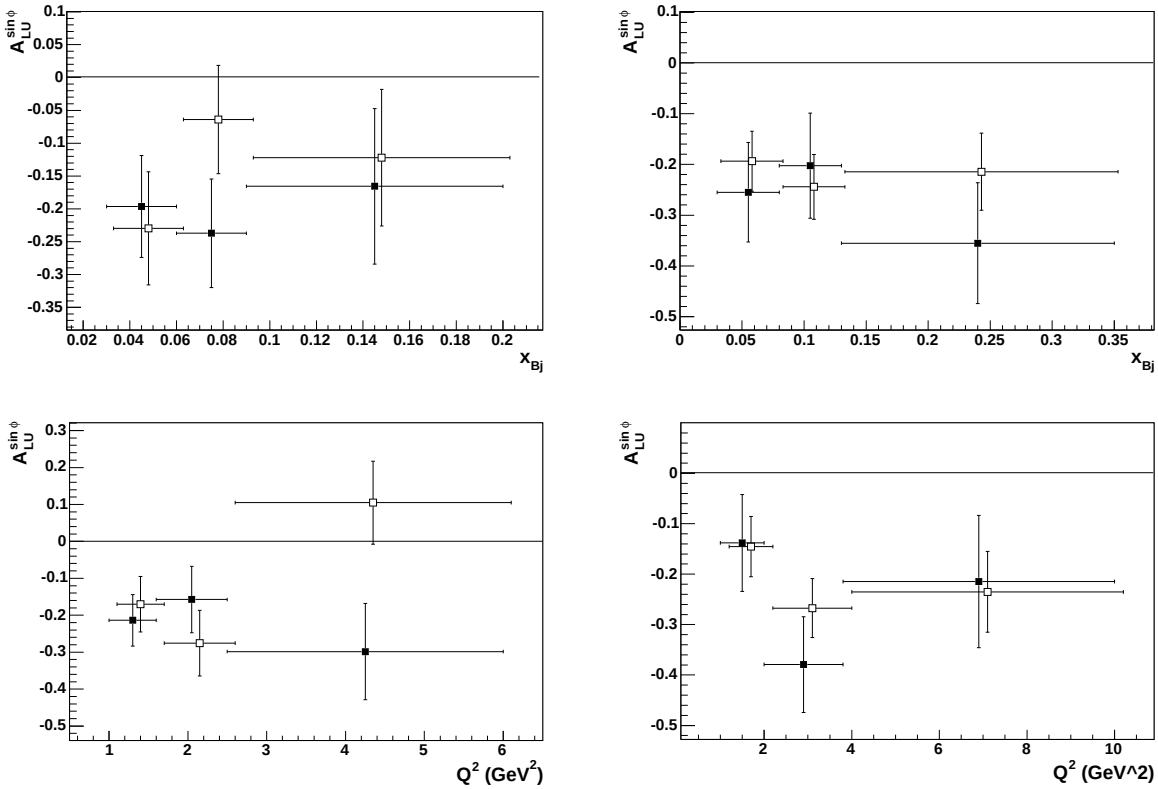

Figure 7.2: Comparison of $A_{LU}^{\sin\phi}$ for the kinematic variables x_{Bj} and Q^2 for neon (filled squares) and hydrogen (open squares). The asymmetries are shown for the coherent sample ($-t_c < 0.045$ GeV^2) in the left panels and for the incoherent sample ($-t_c > 0.045$ GeV^2) in the right panels.

t_c bins. Hence no ϕ dependent nuclear effects are found.

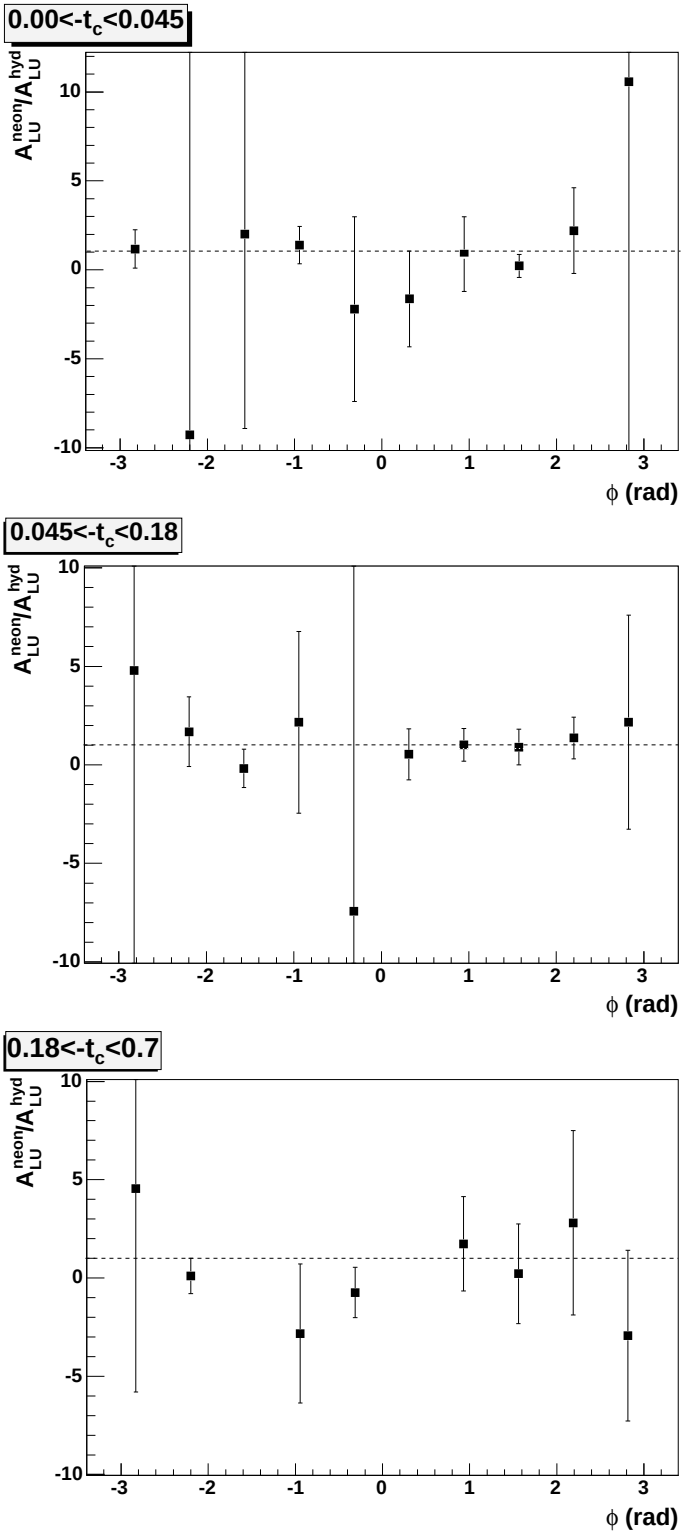

Figure 7.3: The ratio $\frac{A_{LU}^{neon}}{A_{LU}^{hyd}}$ in dependence on ϕ for all three t_c bins.

7.2 Model Calculations and Interpretation

Exploratory studies using GPDs were performed on the generalized EMC effect, i.e. the modifications of the nuclear GPDs with respect to the free-nucleon (more precisely, deuteron) GPDs, normalized to their respective form factors [GS03, LT05a]. In particular it was shown in [LT05a] that the role of partonic transverse degrees of freedom, accounted by a consideration of nucleon off-shellness, is enhanced in the generalized EMC effect. In the model of [LT05a] an enhancement of the ratio $\frac{A_{LU}^{nucleus}}{A_{LU}^{proton}}$ for higher t is predicted. An influence on $A_{LU}^{\sin\phi}$ is also predicted by Guzey and Strikman [GS03], and described in section 2.5. It is shown, apart from the combinatorial enhancement of the asymmetries because of the neutron contribution, that there are two additional effects: while Fermi motion of the nucleons enhances the asymmetries, the presence of the incoherent scattering for larger t reduces the asymmetry. Following the study of Guzey and Strikman, the ratio of neon to proton asymmetry ($\frac{A_{LU}^{nucleus}}{A_{LU}^{Proton}}$) is significantly larger than unity for coherent nuclear DVCS (expected to be close to the factor of two for $t \to 0$). In the case of higher t the inclusion of the incoherent contribution should decrease the ratio of the asymmetries, and $\frac{A_{LU}^{nucleus}}{A_{LU}^{proton}} \simeq 1$ is expected for the incoherent part.

From the results of $A_{LU}^{\sin\phi}$ given above a difference of 0.051 (0.031) between neon and proton is obtained for the coherent (incoherent) part. The extracted ratio is 1.34±0.77 (1.15±0.48) for the coherent (incoherent) part. In figure 7.4 a comparison of the extracted ratio with the theoretical models of Guzey/Strikman [GS03] and Liuti/Taneja [LT05a], as explained in section 2.5, is shown in dependence on t_c. Note that in the theoretical models both coherent and incoherent contribution are used for the calculations. In fact, the statistical error is yet too large to distinguish between the theoretical models.

Summarizing, the asymmetry is in all t_c bins slightly higher for neon than for proton. This seems to be in good agreement to all known theoretical results [GS03, LT05a]. Because of limited statistics no significant conclusions on the behavior of asymmetry ratios vs. t_c can be extracted.

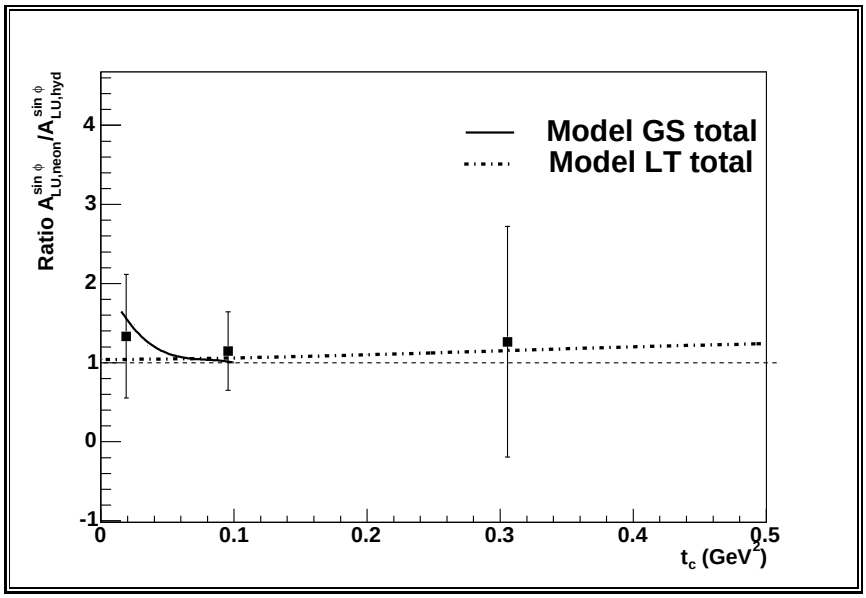

Figure 7.4: Comparison of the ratio $\frac{A^{\sin\phi}_{LU,neon}}{A^{\sin\phi}_{LU,hyd}}$ vs. t_c to theoretical models of Guzey/Strikman (GS) and Liuti/Taneja (LT).

8 Summary and Outlook

The aim of this thesis was to study and to extract the beam-spin asymmetry in hard electroproduction of real photons off neon. The data presented has been accumulated by the HERMES experiment at DESY, scattering the HERA 27.6 GeV polarized positron beam on an unpolarized neon gas target. Attributed to the interference between the Bethe-Heitler process and the deeply-virtual Compton scattering (DVCS) process, the asymmetry gives access to the latter at the amplitude level. Its description is expressed in the theoretical framework of generalized parton distributions (GPDs), which offers a possibility to determine the total angular momentum carried by the quarks in the nucleon. The measurement of DVCS on the proton has shown the possibility to provide a sensitive test of current models of GPDs. Similarly, studying DVCS on a nucleus opens access to the properties of quark and gluon matter inside nuclei by measuring the modification of particle correlations encoded in GPDs due to the nuclear environment.

The DVCS reaction on neon proceeds through two different processes, the coherent process that involves the nucleus as a whole and the incoherent process as the reaction on a single nucleon. Since coherent and incoherent processes contribute to the photon production cross section, both parts have to be separated. In the present analysis the leading amplitude $A_{LU}^{\sin\phi}$ of the beam-spin asymmetry is obtained for the coherent and the incoherent sample. The extraction of these asymmetries has been described in detail and the results are presented as functions of one of the variables x_{Bj}, t_c and Q^2 . In addition, several systematical studies are performed in order to determine consistency and uncertainties of the obtained results.

An explicit extraction of non-leading order effects is not possible, since the amplitudes of the higher harmonics are not significant within the present experimental uncertainty. Finally, although the amplitudes of the leading harmonic $A_{LU}^{\sin\phi}$ have significant values, their interpretation is still difficult. With the present Hermes detector it is not possible to make a separation between the following processes:

- coherent BH-DVCS on neon,
- incoherent BH-DVCS on neutron,
- incoherent BH-DVCS on proton,
- incoherent BH-DVCS on the neutron with excitation of a nuclear resonance.

- incoherent BH-DVCS on the neutron with excitation of a nuclear resonance.

Hence there is presently no way to clearly disentangle the different contributions. In order to solve this problem and to improve the exclusivity of the DVCS process, the installation of a recoil detector is currently under preparation [HERMES04b, Kra].

In summary, the amplitudes of the leading harmonics for the coherent and the incoherent sample are extracted and a clear evidence for a beam-spin asymmetry in each part has been found. In addition, a comparison between proton and neon asymmetries has shown a slightly higher asymmetry for neon than for proton, which is in agreement with theoretical predictions for nuclear DVCS. In the near future, the analysis of BSAs will be extended to other nuclei. Hence, possible nuclear effects could become more visible, including dependences of the atomic number. In fact, with more statistics a distinction between different theoretical models for nuclear models seems possible. In addition, also the theoretical development in the field of nuclear DVCS probably needs more time. A better theoretical interpretation may eventually allow, through comparison to data of higher precision and also more complete kinematics information, to extract new information about the dynamical interplay of complex hadronic systems.

9 Appendix

Tables of Results for the Coherent Sample

x_{Bj} bin	$\langle x_{Bj} \rangle$	$\langle -t_c \rangle$ (GeV^2)	$\langle Q^2 \rangle$ (GeV^2)	$A_{LU}^{\sin\phi} \pm stat. \pm syst.$
0.03 - 0.06	0.049	0.016	1.29	-0.196 ± 0.078 ± 0.011
0.06 - 0.09	0.073	0.019	1.83	-0.236 ± 0.083 ± 0.012
0.09 - 0.20	0.110	0.027	2.79	-0.166 ± 0.119 ± 0.010

$-t_c$ bin	$\langle x_{Bj} \rangle$	$\langle -t_c \rangle$ (GeV^2)	$\langle Q^2 \rangle$ (GeV^2)	$A_{LU}^{\sin\phi} \pm stat. \pm syst.$
0 - 0.014	0.058	0.009	1.47	-0.196 ± 0.078 ± 0.011
0.014 - 0.026	0.071	0.019	1.84	-0.305 ± 0.086 ± 0.014
0.026 - 0.045	0.081	0.034	2.07	-0.109 ± 0.104 ± 0.008

Q^2 bin	$\langle x_{Bj} \rangle$	$\langle -t_c \rangle$ (GeV^2)	$\langle Q^2 \rangle$ (GeV^2)	$A_{LU}^{\sin\phi} \pm stat. \pm syst.$
1.0 - 1.6	0.055	0.017	1.26	-0.214 ±0.069 ± 0.011
1.6 - 2.5	0.075	0.020	1.95	-0.158 ±0.090 ± 0.010
2.5 - 6.0	0.106	0.026	3.20	-0.298 ±0.131 ± 0.014

Table 9.1: The asymmetry $A_{LU}^{\sin\phi}$ of the coherent sample per kinematic bin at the respective average kinematic value.

Tables of Results for the Incoherent Sample

x_{Bj} bin	$\langle x_{Bj} \rangle$	$\langle -t_c \rangle$ (GeV^2)	$\langle Q^2 \rangle$ (GeV^2)	$A_{LU}^{\sin\phi} \pm stat. \pm syst.$
0.03 - 0.08	0.059	0.157	1.62	-0.255 ± 0.098 ± 0.022
0.08 - 0.13	0.102	0.148	2.60	-0.203 ± 0.104 ± 0.018
0.13 - 0.35	0.182	0.191	4.58	-0.355 ± 0.119 ± 0.030

$-t_c$ bin	$\langle x_{Bj} \rangle$	$\langle -t_c \rangle$ (GeV^2)	$\langle Q^2 \rangle$ (GeV^2)	$A_{LU}^{\sin\phi} \pm stat. \pm syst.$
0.045 - 0.12	0.099	0.075	2.40	-0.305 ± 0.089 ± 0.026
0.12 - 0.25	0.111	0.174	2.85	-0.155 ± 0.103 ± 0.015
0.25 - 0.7	0.121	0.374	3.50	-0.273 ± 0.130 ± 0.023

Q^2 bin	$\langle x_{Bj} \rangle$	$\langle -t_c \rangle$ (GeV^2)	$\langle Q^2 \rangle$ (GeV^2)	$A_{LU}^{\sin\phi} \pm stat. \pm syst.$
1.0 - 2.0	0.067	0.135	1.48	-0.138 ± 0.096 ± 0.014
2.0 - 3.8	0.108	0.162	2.80	-0.379 ± 0.095 ± 0.031
3.8 - 10	0.185	0.222	5.23	-0.215 ± 0.131 ± 0.019

Table 9.2: The asymmetry $A_{LU}^{\sin\phi}$ of the incoherent sample per kinematic bin at the respective average kinematic value.

Table of Results for the Comparison of Neon and Hydrogen

				Neon	Hydrogen
$-t_c$ bin	$\langle x_{Bj} \rangle$	$\langle -t_c \rangle$ (GeV^2)	$\langle Q^2 \rangle$ (GeV^2)	$A_{LU}^{\sin\phi} \pm stat. \pm syst.$	$A_{LU}^{\sin\phi} \pm stat. \pm syst.$
0 - 0.045	0.07	0.02	1.7	-0.203±0.051±0.011	-0.152±0.051±0.010
0.045 - 0.18	0.10	0.10	2.5	-0.295±0.075±0.025	-0.257±0.045±0.022
0.18 - 0.7	0.12	0.31	3.3	-0.157±0.099±0.015	-0.124±0.065±0.012

Table 9.3: Comparison of $A_{LU}^{\sin\phi}$ between neon and hydrogen per t_c bin.

Bibliography

[A+76] M. J. Alguard et al., *Deep inelastic scattering of polarized electrons by polarized protons*, Phys. Rev. Lett. **37**, 1261 (1976).

[ABR98] I. Akushevich, H. Bottcher and D. Ryckbosch, *RADGEN 1.0: Monte Carlo generator for radiative events in DIS on polarized and unpolarized targets*, (1998), hep-ph/9906408.

[AGIS83] B. Andersson, G. Gustafson, G. Ingelman and T. Sjostrand, *PARTON FRAGMENTATION AND STRING DYNAMICS*, Phys. Rept. **97**, 31 (1983).

[B+83] G. Baum et al., *A new measurement of deep inelastic e p asymmetries*, Phys. Rev. Lett. **51**, 1135 (1983).

[B+93] D. P. Barber et al., *The HERA polarimeter and the first observation of electron spin polarization at HERA*, Nucl. Instrum. Meth. **A329**, 79–111 (1993).

[B+94] D. P. Barber et al., *High spin polarization at the HERA Electron Storage Ring*, Nucl. Instrum. Meth. **A338**, 166–184 (1994).

[B+02] M. Beckmann et al., *The longitudinal polarimeter at HERA*, Nucl. Instrum. Meth. **A479**, 334–348 (2002), physics/0009047.

[BMK02] A. V. Belitsky, D. Muller and A. Kirchner, *Theory of deeply virtual Compton scattering on the nucleon*, Nucl. Phys. **B629**, 323–392 (2002), hep-ph/0112108.

[Die03] M. Diehl, *Generalized parton distributions*, Phys. Rept. **388**, 41–277 (2003), hep-ph/0307382.

[Ell] F. Ellinghaus, *Beam charge and beam spin azimuthal asymmetries in deeply- virtual Compton scattering*, DESY-THESIS-2004-005.

[FS04] A. Freund and M. Strikman, *DVCS on nuclei: Observability and consequences*, Eur. Phys. J. **C33**, 53–61 (2004), hep-ph/0309065.

[GPRV04] M. Guidal, M. V. Polyakov, A. V. Radyushkin and M. Vanderhaeghen, *Nucleon form factors from generalized parton distributions*, (2004), hep-ph/0410251.

[GS03] V. Guzey and M. Strikman, *DVCS on spinless nuclear targets in impulse approximation*, Phys. Rev. **C68**, 015204 (2003), hep-ph/0301216.

[H101] C. Adloff et al. (H1 Collaboration), *Measurement of deeply virtual Compton scattering at HERA*, Phys. Lett. **B517**, 47–58 (2001), hep-ex/0107005.

[HERMES98] K. Ackerstaff et al. (HERMES Collaboration), *HERMES spectrometer*, Nucl. Instrum. Meth. **A417**, 230–265 (1998), hep-ex/9806008.

[HERMES03] F. Ellinghaus, R. Shanidze and J. Volmer (HERMES Collaboration), *Deeply-virtual Compton scattering on deuterium and neon at HERMES*, AIP Conf. Proc. **675**, 303–307 (2003), hep-ex/0212019.

[HERMES04a] E. Avetisyan, A. Rostomyan and A. Ivanilov (HERMES Collaboration), *Beam-spin azimuthal asymmetries in pion electroproduction at HERMES*, (2004), hep-ex/0408002.

[HERMES04b] B. Seitz (HERMES Collaboration), *The HERMES recoil detector: A combined silicon strip and scintillating fibre detector for tracking and particle identification*, Nucl. Instrum. Meth. **A535**, 538–541 (2004).

[HERMES05] A. Airapetian et al. (HERMES Collaboration), *Quark helicity distributions in the nucleon for up, down, and strange quarks from semi-inclusive deep-inelastic scattering*, Phys. Rev. **D71**, 012003 (2005), hep-ex/0407032.

[HJ98] P. Hoodbhoy and X.-D. Ji, *Helicity-flip off-forward parton distributions of the nucleon*, Phys. Rev. **D58**, 054006 (1998), hep-ph/9801369.

[Hof57] R. Hofstadter, *Nuclear and nucleon scattering of high-energy electrons*, Ann. Rev. Nucl. **7**, 231–316 (1957).

[HZ] P. R. B. Saull (H1 and ZEUS Collaborations), *Deeply virtual Compton scattering*, Prepared for International Europhysics Conference on High-Energy Physics (HEP 2001), Budapest, Hungary, 12-18 Jul 2001.

[JF99] J.C.Collins and A. Freund, Phys. Rev. D **59**, 074009 (1999).

[Ji97a] X.-D. Ji, *Deeply-virtual Compton scattering*, Phys. Rev. **D55**, 7114–7125 (1997), hep-ph/9609381.

[Ji97b] X.-D. Ji, *Gauge invariant decomposition of nucleon spin*, Phys. Rev. Lett. **78**, 610–613 (1997), hep-ph/9603249.

[Ji98] X.-D. Ji, *Off-forward parton distributions*, J. Phys. **G24**, 1181–1205 (1998), hep-ph/9807358.

[Ji03] X.-d. Ji, *Generalized parton distributions and the spin structure of the nucleon*, Nucl. Phys. Proc. Suppl. **119**, 41–49 (2003), hep-lat/0211016.

[Kra] B. Krauss, *Deeply virtual Compton scattering and the HERMES recoil-detector*, DESY-THESIS-2005-008.

[LT05a] S. Liuti and S. K. Taneja, *Microscopic description of deeply virtual Compton scattering off spin-0 nuclei*, (2005), hep-ph/0505123.

[LT05b] S. Liuti and S. K. Taneja, *Nuclear medium modifications of hadrons from generalized parton distributions*, (2005), hep-ph/0504027.

[M$^+$94] D. Muller et al., *Wave functions, evolution equations and evolution kernels from light-ray operators of QCD*, Fortschr. Phys. **42**, 101 (1994), hep-ph/9812448.

[MPW98] L. Mankiewicz, G. Piller and T. Weigl, *Hard exclusive meson production and nonforward parton distributions*, Eur. Phys. J. **C5**, 119–128 (1998), hep-ph/9711227.

[MT69] L. W. Mo and Y.-S. Tsai, *RADIATIVE CORRECTIONS TO ELASTIC AND INELASTIC e p AND mu p SCATTERING*, Rev. Mod. Phys. **41**, 205–235 (1969).

[Muon88] J. Ashman et al. (European Muon Collaboration), *MEASUREMENT OF THE RATIOS OF DEEP INELASTIC MUON - NUCLEUS CROSS-SECTIONS ON VARIOUS NUCLEI COMPARED TO DEUTERIUM*, Phys. Lett. **B202**, 603 (1988).

[Muon89] J. Ashman et al. (European Muon Collaboration), *An investigation of the spin structure of the proton in deep inelastic scattering of polarized muons on polarized protons*, Nucl. Phys. **B328**, 1 (1989).

[Now02] W.-D. Nowak, *Physics objectives for future studies of the spin structure of the nucleon*, (2002), hep-ph/0210409.

[Now05] W.-D. Nowak, *Deeply virtual Compton scattering: Results and future*, (2005), hep-ex/0503010.

[Pol03] M. V. Polyakov, *Generalized parton distributions and strong forces inside nucleons and nuclei*, Phys. Lett. **B555**, 57–62 (2003), hep-ph/0210165.

[PW99] M. V. Polyakov and C. Weiss, *Skewed and double distributions in pion and nucleon*, Phys. Rev. **D60**, 114017 (1999), hep-ph/9902451.

[Rad96] A. V. Radyushkin, *Asymmetric gluon distributions and hard diffractive electroproduction*, Phys. Lett. **B385**, 333–342 (1996), hep-ph/9605431.

[Rad97] A. V. Radyushkin, *Nonforward parton distributions*, Phys. Rev. **D56**, 5524–5557 (1997), hep-ph/9704207.

[Sjo94] T. Sjostrand, *High-energy physics event generation with PYTHIA 5.7 and JETSET 7.4*, Comput. Phys. Commun. **82**, 74–90 (1994).

[ST64] A. A. Sokolov and I. M. Ternov, *On Polarization and spin effects in the theory of synchrotron radiation*, Phys. Dokl. **8**, 1203–1205 (1964).

Acknowledgements

This thesis could not have been written without the help of many people and I would like to thank all of them for their support.
First and foremost, I would like to thank my advisor Dr. Wolf-Dieter Nowak who encouraged me to begin this work at HERMES and always found the time and patience to discuss all questions and to listen to my presentations. I am also grateful for his careful reading of this manuscript and his detailed comments and suggestions on it. My special thanks go to Prof. Dr. Butz who agreed on supervising this dissertation as my official advisor at the University of Leipzig.
I want to express my gratitude to all Hermes members, especially to Elke Aschenauer and Delia Hasch, for their support throughout the work on the diploma thesis.
In particular I would like to thank Frank Ellinghaus, who introduced me in the DVCS analysis, Hayg Guler and Frank Zhenyu Ye for their helps on my data analysis and for all the inspiring discussions on physics as well as on unrelated topics. Outside the DVCS group I benefited from discussions with Achim Hillenbrand and Markus Diefenthaler, who helped me with their patient advices and with software problems of all kind. I would like to thank Jim Stewart and Eduard Avetisyan for their knowledge and explanation of the Hermes detectors.
My thanks also go to all Hermes members who are not mentioned above and I very much appreciated the friendly athmosphere in the entire group, who made work and life in Hamburg so enjoyable.
Finally, I would like to thank my friends and my family for their support and understanding.

Declaration

This document is the result of my own work. Material from the published or unpublished work of otheres, which is referred to in the document, is credited to the author in the text.

Selbständigkeitserklärung

Hiermit erkläre ich, die vorliegende Diplomarbeit selbständig und nur unter Verwendung der angegebenen Hilfsmittel und Quellen angefertigt zu haben.

Leipzig, den 16.08.2005